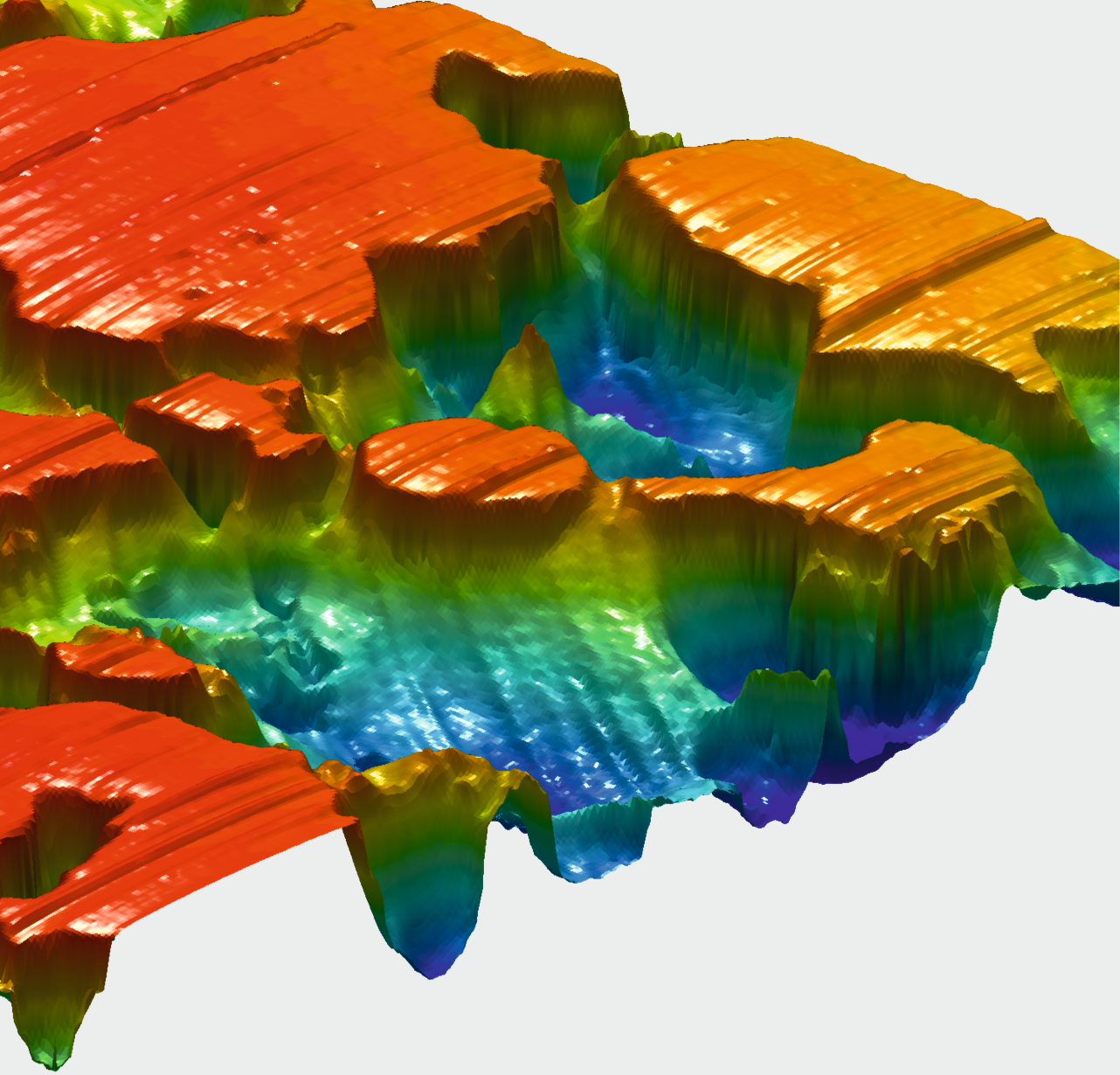

Multi-scale friction modeling for sheet metal forming

Johan Hol

MULTI-SCALE FRICTION MODELING FOR SHEET METAL FORMING

Johan Hol

De promotiecommissie is als volgt samengesteld:

Voorzitter en secretaris:	
Prof.dr. G.P.M.R. Dewulf	Universiteit Twente
Promotor:	
Prof.dr.ir. A.H. van den Boogaard	Universiteit Twente
Assistent promotor:	
Dr.ir. V.T. Meinders	Universiteit Twente
Leden:	
Prof.dr.ir. A. de Boer	Universiteit Twente
Prof.dr.-ing.dipl.-wirtsch.-ing. P. Groche	Technische Universität Darmstadt
Prof.dr.ir. D.J. Schipper	Universiteit Twente
Dr.ir. E.M. Toose	Tata Steel
Prof.dr.ir. M. Vermeulen	Universiteit Gent

This research was carried out under project number MC1.07289 in the framework of the Research Program of the Materials innovation institute (M2i) in the Netherlands (www.m2i.nl).

Multi-scale friction modeling for sheet metal forming
Hol, Johan
PhD thesis, University of Twente, Enschede, The Netherlands
December 2013

ISBN 978-90-77172-98-8
Keywords: boundary lubrication modeling, mixed lubrication modeling, friction characterization, sheet metal forming

Printed by Ipskamp Drukkers B.V., Enschede, The Netherlands

Cover: 3D surface impression measured by confocal microscopy. Material: DC06 EN10130:2006 with an EDT surface finish ($S_q = 1.8\,\mu m$). Resolution: $1.1 \times 1.1\,\mu m$.

MULTI-SCALE FRICTION MODELING FOR SHEET METAL FORMING

PROEFSCHRIFT

ter verkrijging van
de graad van doctor aan de Universiteit Twente,
op gezag van de rector magnificus,
prof.dr. H. Brinksma,
volgens besluit van het College voor Promoties
in het openbaar te verdedigen
op donderdag 19 december 2013 om 10.45 uur

door

Johan Hol

geboren op 15 augustus 1985

te Bernisse

Dit proefschrift is goedgekeurd door de promotor

Prof.dr.ir. A.H. van den Boogaard

en de assistent promotor

Dr.ir. V.T. Meinders

Summary

Finite element (FE) formability analyses are everyday practice in the metal-forming industry to reduce costs and lead time of new metal products. Although the predictive capabilities of FE software codes have improved significantly over the years, unfortunately, the experimental trial-and-error process can still not be entirely replaced by virtual design. The simplistic handling of friction in FE software is one of the main reasons for this. In this thesis, friction mechanisms in metal forming are addressed and a physical based friction model is proposed to improve the description of friction in metal forming processes.

In the automotive industry, parts are usually formed by using the rust preventive lubricant present on the sheet. As the amount of lubricant is not enough to fill the roughness of the sheet, the load will be mainly carried by contacting surface asperities. Friction under these conditions is referred to as boundary lubrication friction. A multi-scale friction model is developed in this research that accounts for the change in surface topography and the evolution of friction in this regime. The friction model has been implemented in an FE software code, enabling the accurate modelling of friction in full-scale forming simulations.

If enough lubricant is present to fill the non-contacting surface valleys, the lubricant can carry some load as well. In this case, a lower fraction of the total load is carried by contacting surface asperities. Friction in this regime is referred to as mixed lubrication friction, which is characterized by lower friction coefficients compared to boundary lubrication friction. A hydrodynamic friction model is developed in this research to determine the load-carrying capacity of the lubricant. The hydrodynamic friction model is coupled to the boundary lubrication friction model to describe friction in the mixed lubrication regime. The lubricant film thickness, calculated from the amount of lubricant present in non-contacting surface valleys, is used to realize this coupling. Mixed lubrication interface elements are introduced to solve the governing differential equations. The interface elements have been implemented in an FE software code to describe mixed lubrication friction in metal forming simulations.

An experimental procedure is proposed to quantify input parameters of the advanced friction model. A method to obtain deterministic and stochastic 3D rough surface descriptions is discussed and a procedure is proposed to determine the interfacial shear strength of boundary layers. Loading and sliding experiments have been conducted to investigate the development of real contact area and friction coefficients during sliding. Results have been used to calibrate model parameters and to show the predictive capabilities of the friction model.

Two deep-drawing applications are discussed to demonstrate the performance of the advanced friction model. A comparison is made between numerically and experimentally obtained punch force–displacement diagrams. FE results showed a distribution in friction coefficients that depend on location and time, and rely on external process settings like the blankholder force, punch velocity and lubrication amount. An excellent prediction of punch forces can be made for simple-shaped metal products, showing a decrease in friction coefficients for increasing the blankholder force, increasing the lubrication amount or increasing the lubricant viscosity. For complex-shaped products, a good prediction of punch forces can be made. A small difference between experimental and numerical punch forces is found, which could be caused by the advanced friction model, but also by the material model used during the forming simulation. That is, for complex metal products more energy is required to deform the material, reducing the relative influence of friction. An increase in computation time of approximately 50 %, compared to using a Coulomb friction model, was obtained for both applications. If starvation of lubricant occurs, meaning that only boundary lubrication is present, the boundary lubrication friction model can be used. This excludes the use of mixed lubrication elements, yielding an increase in simulation time of only 3 % compared to using a Coulomb friction model.

Numerical results obtained by using the mixed lubrication friction model are compared with results obtained by using the Coulomb friction model. The value of the (constant) Coulomb friction coefficient is generally unknown in advance and is often adapted based on a trial-and-error approach to mimic experimentally obtained punch forces. It is shown that the fitted value only holds for a specific forming process, and depends on the process settings used (like the blankholder force or the amount of lubricant). Therefore, the Coulomb friction coefficient has to be adapted for each specific situation. Contrary to the Coulomb friction model, the advanced friction model does not require any adaptions to the original input data when process settings are changed. This clearly demonstrates the increased predictive capabilities of the FE simulation by using the advanced friction model. An accurate prediction of friction can be made, rather than fitting the FE data to experiments using a constant friction coefficient.

Samenvatting

Eindige elementen (EE) simulaties spelen in de industriële omvorming van metalen een belangrijke rol bij het streven naar kortere doorlooptijden van nieuwe producten. Hoewel commerciële EE-softwarepakketten in de afgelopen jaren aanzienlijk nauwkeuriger zijn geworden, is het helaas nog niet mogelijk om experimentele trial-and-error procedures volledig te vervangen door EE-simulaties. Dit komt met name door de manier waarop wrijving gemodelleerd wordt in EE-softwarepakketten. Om wrijving nauwkeuriger te modelleren in EE-simulaties van metaal omvormingsprocessen, wordt er in dit proefschrift een fysisch gebaseerd wrijvingsmodel voorgesteld. Hierin wordt rekening gehouden met de meest invloedrijke wrijvingsmechanismen.

In de auto-industrie worden plaatonderdelen normaliter gevormd door direct gebruik te maken van het (roestwerende) smeermiddel dat door de staalfabrikant op de plaat is aangebracht. Als de hoeveelheid smeermiddel onvoldoende is om de ruwheid van de plaat volledig op te vullen, dan zal onder belasting de volledige druk gedragen worden door metaal-metaal contact. Wrijving onder deze omstandigheden wordt wrijving in het grenssmeringsgebied genoemd. In dit onderzoek is een wrijvingsmodel ontwikkeld dat in staat is de plastische vervorming van ruwheidstoppen en de verandering van de wrijvingscoëfficiënt onder verschillende belastingen te beschrijven. Het wrijvingsmodel is in een EE-softwarepakket geïmplementeerd, waardoor wrijving in omvormsimulaties nauwkeurig gemodelleerd kan worden.

Als voldoende smeermiddel aanwezig is om de ruwheid van het plaatmateriaal op te vullen, dan kan een gedeelte van de aangebrachte belasting gedragen worden door het smeermiddel zelf. Wrijving onder deze omstandigheden wordt wrijving in het gemengd gesmeerde gebied genoemd, wat gekarakteriseerd wordt door lagere wrijvingscoëfficiënten dan in het grenssmeringsgebied. In dit proefschrift is een hydrodynamisch wrijvingsmodel ontwikkeld om de dragende werking van het smeermiddel te bepalen. Dit model is vervolgens gekoppeld aan het model voor grenssmeringswrijving door naar de laagdikte van het

smeermiddel te kijken. Hierdoor wordt het mogelijk om de wrijving in het gemengd gesmeerde gebied te beschrijven. De laagdikte wordt berekend aan de hand van de hoeveelheid smeermiddel dat omsloten zit in de ruwheidsdalen van het plaatmateriaal. In een EE-softwarepakket zijn contactelementen met extra drukvrijheidsgraden geïmplementeerd om de drukopbouw in het smeermiddel te modelleren. Door deze elementen met het grenssmeringsmodel te koppelen wordt het mogelijk om gemengd gesmeerde wrijving in omvormsimulaties te beschrijven.

Om de benodigde invoerparameters van het wrijvingsmodel te bepalen wordt in dit proefschrift een experimentele methode voorgesteld. Er wordt een methode besproken voor het bepalen van deterministische en stochastische oppervlakteparameters, en er wordt een experimentele procedure beschreven voor het bepalen van de afschuifsterkte van de grenslaag. Er zijn wrijvingsexperimenten uitgevoerd waarin de normaaldruk gevarieerd wordt, om de ontwikkeling van het werkelijke contactoppervlak en de wrijvingscoëfficiënt te bestuderen. De resultaten van deze experimenten zijn vervolgens gebruikt om modelparameters te kalibreren en het voorspellend vermogen van het wrijvingsmodel aan te tonen.

Om de mogelijkheden van het geavanceerde wrijvingsmodel te demonstreren worden er in dit proefschrift twee verschillende dieptrektoepassingen besproken. Resultaten van EE-simulaties laten een plaats- en tijdsafhankelijk verloop in wrijvingscoëfficiënten zien. Het verloop in wrijvingscoëfficiënten verandert wanneer externe procesinstellingen anders gekozen worden, zoals de plaathouderkracht, de stempelsnelheid of de smeermiddelhoeveelheid. Voor simpel gevormde plaatproducten kan de experimenteel bepaalde stempelkracht accuraat beschreven worden in de EE-omgeving. EE-simulaties laten zien dat de wrijvingscoëfficiënt afneemt bij een toenemende plaathouderkracht, bij een toenemende smeermiddelhoeveelheid en bij een toenemende smeermiddelviscositeit. Ook voor complex gevormde plaatproducten kan de stempelkracht goed beschreven worden. Hier is echter een klein verschil gevonden tussen de numeriek en experimenteel bepaalde stempelkracht. Dit kan komen door het wrijvingsmodel, maar ook door het materiaalmodel dat gebruikt is in de EE-simulaties. Voor complex gevormde producten is er immers meer energie nodig om het materiaal te vervormen. Dit vermindert de relatieve invloed van wrijving op het productieproces. Vergeleken met een EE-simulatie uitgevoerd met een standaard Coulombs wrijvingsmodel, waarin een constante waarde voor de wrijvingscoëfficiënt aangenomen wordt, neemt de rekentijd met ongeveer 50 % toe. Wanneer onvoldoende smeermiddel aanwezig is om een hydrodynamische drukopbouw in het smeermiddel te genereren, kan het

ontwikkelde wrijvingsmodel voor grenssmering gebruikt worden. Voor deze specifieke situatie kan wrijving bepaald worden zonder gebruik te maken van de ontwikkelde smeermiddelelementen. Hierdoor neemt de rekentijd vergeleken met een EE-simulatie uitgevoerd met een standaard Coulombs wrijvingsmodel met slechts 3 % toe.

Numerieke resultaten verkregen met het gemengd gesmeerde wrijvingsmodel zijn vergeleken met resultaten verkregen met het Coulombse wrijvingsmodel. De waarde voor de (constante) Coulombse wrijvingscoëfficiënt is normaliter onbekend en wordt daarom vaak zo gekozen dat experimenteel bepaalde stempelkrachten accuraat beschreven kunnen worden. Dit onderzoek laat zien dat de voorspelde waarde voor de wrijvingscoëfficiënt alleen toepasbaar is voor een specifiek omvormproces, en deze waarde zal daarom aangepast moeten worden als de procesinstellingen (zoals de plaathouderdruk of de smeermiddelhoeveelheid) veranderen. In tegenstelling tot het Coulombse wrijvingsmodel hoeven de invoerparameters van het geavanceerde wrijvingsmodel niet aangepast te worden wanneer procesinstellingen veranderen. Dit laat duidelijk zien dat het voorspellend vermogen van EE-omvormsimulaties geoptimaliseerd kan worden door gebruik te maken van het geavanceerde wrijvingsmodel.

Nomenclature

The symbols used in this thesis are classified in a Greek and Roman category. Some symbols appear more than once, their specific meaning follows from their context or from subscripts

Greek symbols

α	fractional real contact area	[-]
β, γ	nodal counters	[-]
γ, β, ψ	internal energy factors	[N mm]
γ	fan angle	[-]
γ	Peklenik surface pattern parameter	[-]
ε_0	initial strain	[-]
ε	total plastic strain in deforming bars	[-]
ε_p	plastic strain in bulk material	[-]
$\dot{\varepsilon}_\mathrm{p}$	strain-rate in bulk material	[s^{-1}]
η	persistence parameter	[-]
η	dynamic viscosity	[Pa s]
θ	attack angle	[-]
θ_eff	effective attack angle	[-]
λ	reference height of bars	[mm]
μ	friction coefficient	[-]
ν	increase in fractional real contact area	[-]
ξ	generalized midpoint parameter	[-]
ρ	asperity density	[mm^{-1}]
σ	standard deviation	[MPa]
σ_y	yield strength	[MPa]
τ	shear stress between moving bars	[MPa]
τ	shear strength of the interfacial boundary layer	[MPa]
$\boldsymbol{\tau}$	lubricant shear stresses	[MPa]

$\boldsymbol{\tau}_1, \boldsymbol{\tau}_2$	lubricant shear stresses at the lower (1) and upper (2) surface	[MPa]
τ_{lub}	Euclidean norm of hydrodynamic shear stresses	[MPa]
τ_{sol}	shear stress between sliding asperities	[MPa]
ϕ	surface height distribution	[mm^{-1}]
ϕ	orientation elliptical paraboloid	[-]
χ	shape factor	[-]
ω	indentation factor	[mm]
ω	indentation depth of elliptical paraboloid	[mm]
ΔA	contact area bar	[mm^2]
Δs	shear distance	[mm]
Δu	raise non-contacting bars	[mm]
Δz	crushing height bars	[mm]
$\boldsymbol{\Phi}_{\text{p}}, \boldsymbol{\Phi}_{\text{s}}$	flow factors used in the averaged Reynolds equation	[-]

Roman symbols

a_{x}	characteristic length of ellipse	[mm]
a, b	major and minor axis of ellipse	[mm]
d	indentation parameter	[mm]
e	error value	[-]
f_{C}	shear factor	[-]
f	shear forces	[N]
h	fluid film thickness	[mm]
$\dot{\mathbf{h}}$	material time derivative	[mm/s]
k	shear factor used in Tabor's junction growth model	[-]
k	shear strength workpiece material	[MPa]
l	mean half spacing between asperities	[mm]
l, w	length and width of hydrodynamic test cases	[mm]
n_{s}	number of surrounding bars	[-]
$\mathbf{n}$	outward pointing unit vector	[-]
p	pressure	[MPa]
$\overline{p}$	mean pressure	[MPa]
t	time	[s]
$\mathbf{u}$	displacement field	[mm]
$\mathbf{u}$	relative velocity	[mm/s]
v_{a}	downward velocity crushing asperities	[mm/s]
v_{b}	upward velocity non-contacting surface	[mm/s]

$\mathbf{v}_1, \mathbf{v}_2$	velocity in x- and y-direction at the lower (1) and upper (2) surface	[mm/s]
v	velocity	[mm/s]
$\mathbf{v}$	velocity field	[mm/s]
$\mathbf{v}$	sum velocity	[mm/s]
v_{punch}	punch velocity	[mm/s]
w	width of a bar	[mm]
z	height parameter	[mm]
A	(contact) area	[mm^2]
A	lubrication domain	[mm^2]
B	hardness factor	[-]
$\mathbf{B}$	spatial derivative of interpolation matrix	[mm^{-1}]
C	boundary of lubrication zone	[mm]
F	non-dimensional force	[-]
F_{bhf}	blankholder force	[N]
F_{N}	normal force	[N]
F_{w}	shear force	[N]
H	hardness	[MPa]
$\dot{\mathbf{H}}$	nodal material time derivative	[mm/s]
H	non-dimensional fluid film thickness	[-]
H_{eff}	effective hardness	[MPa]
$\mathbf{I}$	second order unity tensor	[-]
$\mathbf{K}_{\text{c}}$	contact stiffness matrix	[N/mm]
$\mathbf{K}_{\text{p}}$	fluidity matrix	[mm^3/(Mpa s)]
$\mathbf{K}_{\text{v,u,}\dot{\text{h}}}$	fluidity matrices	[mm^2]
L	lubricant number	[-]
L_{s}	characteristic shear length	[mm]
M	total number of bars	[-]
N, N^*, N^{**}	number of contacting/ non-contacting bars	[-]
$\mathbf{N}$	interpolation matrix	[-]
$\mathbf{P}$	hydrodynamic pressure field	[MPa]
P_{LUB}	non-dimensional hydrodynamic pressure distribution	[-]
$\mathbf{R}_{\text{F}}$	residual force vector	[N]
$\mathbf{R}_{\text{p}}$	residual fluidity vector	[mm^3/s]
S	shear factor	[-]
S_{a}	average surface roughness	[mm]
S_{q}	composite RMS surface roughness	[mm]
U	uniform raise of non-contacting bars	[mm]

$\mathbf{U}$, $\mathbf{V}$	nodal velocity fields	[mm/s]
V	volume	[mm^3]
W	internal and external energy terms	[N mm]
W	velocity parameter	[-]
X	non-dimensional position parameter	[-]

Subscripts

ab	absorbed
ave	average
cp	contact patch
ε	strain dependent parameters
ell	ellipse
ext	external
i	number of iteration
int	internal
L	load dependent parameters
lub	lubricant
n	number of increment
nom	nominal
ri	raise
S	sliding dependent parameters
sh	shear
sol	solid
t	tool
tot	total
w	workpiece
x, y, z	axis
$x1$, $y1$, $z1$	direction subscripts referring to the lower surface
$x2$, $y2$, $z2$	direction subscripts referring to the upper surface

Various

$\mathbf{B}^{\mathrm{T}}$	transpose of tensor $\mathbf{B}$
$\cdot$	single tensor contraction
:	double tensor contraction
δ	prefix for a virtual quantity
Δ	prefix for an incremental quantity
∇	spatial gradient operator

Abbreviations

ALE	arbitrary Lagrangian Eulerian
d.o.f.	degree of freedom
EDT	electro discharged textured
EE	eindige elementen
FE	finite element
RFT	rotational friction tester
RMS	root mean square

Contents

Chapter 1

Introduction

The challenge in metal forming technology is zero failure production, reducing the cost and lead time of new metal products. To establish this goal, a thorough knowledge of materials and production techniques is required. Over recent years, significant improvements have been made in understanding the complex forming behavior of metals and failure mechanisms using simulation techniques. An accurate description of friction between dies and workpiece is, however, lagging behind, but is gaining more and more attention from industry and academia due to its accepted relevance in metal forming. The aim of this work is to contribute to a better description of frictional behavior in metal forming simulations. The motivation, objective and outline of this thesis is presented in this chapter.

1.1 Sheet metal forming

Metal forming refers to a group of manufacturing methods by which a piece of metal is converted into a desired product shape without material removal. Today, metal forming is one of the most important technologies in the manufacturing industry. Highly automated mass production plants produce a wide variety of metal products, finding its application in construction, the automotive industry, packaging, energy, domestic appliances and industry.

Metal forming processes can be broadly classified into two classes: bulk metal forming and sheet metal forming. In both forming processes, the metal is deformed plastically to ensure the deformation is permanent. The shape of the final product is determined by the contour of one or more dies, depending on the metal forming process used. In bulk metal forming processes, the volume of the workpiece material is in general large compared to the surface area. Well-known bulk forming processes are rolling, wire drawing, extrusion and forging. In sheet metal forming, the thickness of the workpiece is small compared to the other dimensions. Examples are bending, deep-drawing, stretch-forming and hydro-forming. Each metal forming process has its own characteristics in terms of tooling and material flow. In this thesis, the deep-drawing process is considered, which is one of the most popular and widely investigated sheet metal forming processes [14].

Typical application fields of deep-drawing are automotive, aerospace and packaging, which all employ metal forming processes on a large scale. During the deep-drawing process, a flat sheet metal blank is clamped in between a die and a blankholder, see Figure 1.1. The punch is pushed into the die cavity which transfers the specific shape of the punch and the die to the blank. The deformation process is controlled by restraining the sheet metal through friction between the die and the blankholder. The quality of a formed product is judged by the occurrence of necking and fracture, wrinkles, scratching, and the geometrical accuracy of the product after releasing it from the tools. Tooling design, process parameters, blank material, blank shape, lubricant and surface finish of the tool and the workpiece material are all influencing factors that determine the final quality of the product. Due to the complex interaction between these factors, both mechanical and tribological knowledge is necessary to optimize the performance of forming processes [2, 61].

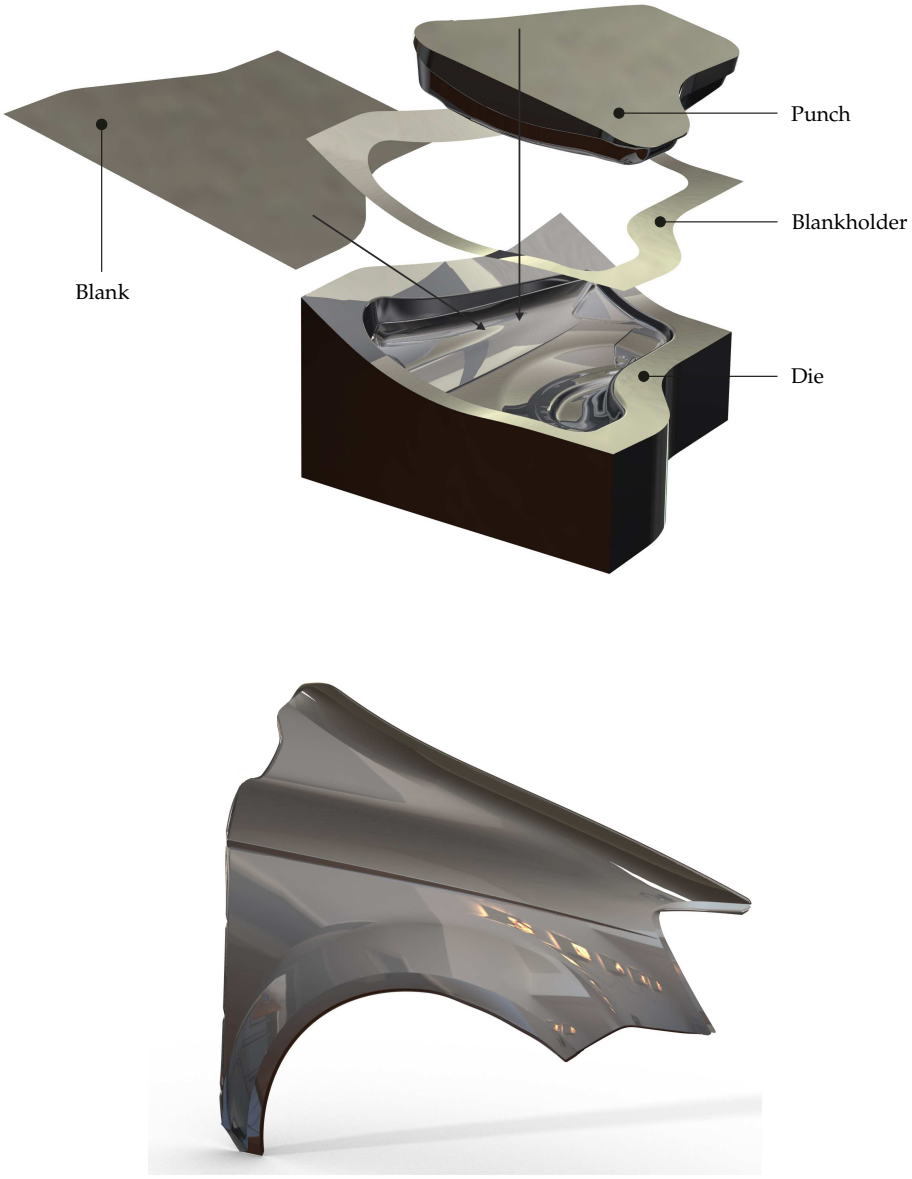

Figure 1.1 *Example deep-drawing set-up front-fender (NUMISHEET'02 benchmark).* ***Top:*** *Exploded view.* ***Bottom:*** *Deep drawn front-fender.*

1.2 Motivation

Until the 1990s, expensive and time-consuming experimental trial-and-error methods were required to produce defect free products. The development of finite element (FE) based simulation software was an important breakthrough in the design of manufacturing processes. The development of FE techniques started in the 1940s, and was first applied to industrial metal forming problems in the 1980s. Over recent years, the application field of FE simulations has grown significantly, and has become a standard tool in the design stage of new metal products. Nowadays, optimization algorithms are coupled to FE simulations to automatically optimize the design of new production processes [45, 82]. Decreasing the costs per product, reducing the time-to-market and increasing the product quality are the main driving forces behind these innovations [22].

Although the accuracy of FE software has improved significantly over the years, unfortunately, the experimental trial-and-error process can still not be entirely replaced by virtual design. The simplistic handling of friction in FE software can be attributed as being one of the main reasons for this. The role of friction in most sheet metal forming processes is significant to other process parameters, especially when dealing with thin metal sheets. In most commercially available software packages, however, a simple Coulomb friction model is used. The Coulomb friction model uses a constant friction coefficient that relates friction forces between the blank and the tooling to the applied normal contact force. From theoretical and experimental studies [15, 21, 88], it is, however, known that the friction coefficient is not constant under forming conditions. In fact, the friction coefficient depends on local process parameters like the nominal contact pressure and the sliding velocity. Moreover, friction depends on the interface properties of the contacting surfaces, e.g. surface roughness, material properties and type of lubricant used, see Figure 1.2 [2, 61]. Friction is described by a complex interaction between these variables, complicating the accurate description of friction.

Experimental and theoretical studies have been performed to account for local varying friction coefficients in metal forming simulations. Experimentally obtained friction coefficients are either directly used in FE simulations [17, 23, 66], or used to generate empirical models that cover a larger range of process parameters, e.g. by generating Stribeck curves [63, 68]. However, such methods only apply to certain test conditions, and do not cover the full range of process conditions that can occur in forming operations. Micro-mechanical (theoretical) studies on the other hand have given a more physical explanation of the actual interactions between contacting surface asperities [9, 21, 49, 88]. However, until

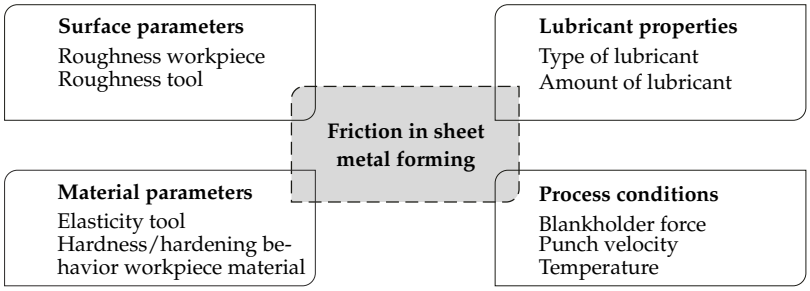

Figure 1.2 *Friction in sheet metal forming.*

now, these micro models were always regarded as too cumbersome to be used in large-scale forming simulations.

An improved friction model will enhance the predictive capabilities of FE simulation techniques, supporting 'first time right principles' in metal forming technology. Accounting for the surface texture evolution during forming will contribute to an enhanced control over the surface quality of a product, which will support the development of optimal surfaces for consistent pressing and painting. Regarding these topics, there is a clear call from industry to develop more sophisticated friction models.

1.3 Objective

The objective of this research project is to provide a physical based friction model, that is computationally attractive for use in full-scale *automotive* sheet metal forming simulations. To satisfy this goal, a proper description of the following lubrication conditions is required:

- In the automotive industry, parts are usually pressed by using the rust preventive lubricant present on the sheet. As the amount of lubricant is not enough to fill the roughness of the sheet, the load will be mainly carried by contacting surface asperities of the sheet and the tool. Friction under these conditions is referred to as boundary lubrication friction. To accurately describe friction in this regime, a model is required that accounts for the change in surface topology and the evolution of friction due to interacting surface asperities.
- As the roughness of the workpiece surface is liable to changes during the forming process, the roughness can become small enough for the lubricant to be trapped into non-contacting surface valleys. In this case, the lubricant

can start to carry some load, meaning that a lower fraction of the load is carried by contacting surface asperities. Friction in this regime is referred to as mixed lubrication friction, which is characterized by lower friction coefficients compared to boundary lubrication friction. An extension of the boundary lubrication friction model is required to account for mixed lubrication friction.

The project has been divided into two PhD research projects. The first PhD project (executed by Karupanassamy [32]) focused on the development of advanced micro-mechanical friction models. The second research project, discussed in this thesis, focused on the development of a stable and efficient algorithm that accounts for a pressure, deformation and velocity dependent friction coefficient in FE software.

1.4 Outline

The thesis starts with the description of a boundary lubrication friction model in Chapter 2. A methodology is presented that accounts for micro-mechanical friction mechanisms playing a role in sheet metal forming. The methodology consists of a modular framework in which models have been implemented to describe the change of surface topology and the evolution of friction. Existing, adapted and newly developed models are outlined and the translation from micro-contact modeling to macro-contact modeling is discussed. Moreover, a method is presented to efficiently implement the developed friction model in FE software codes, enabling the prediction of friction in full-scale forming simulations. In Chapter 3, an extension of the boundary lubrication friction model is discussed to account for friction in the mixed lubrication regime. A coupling with a hydrodynamic friction model has been made for this purpose. The coupling between the two friction models is discussed, and an FE solution procedure is presented to solve the governing differential equations. The implementation of the mixed lubrication friction model in FE software is outlined, introducing mixed lubrication interface elements. An experimental procedure to quantify model parameters is presented in Chapter 4. A method to obtain deterministic and stochastic descriptions of 3D rough surfaces is discussed and an experimental procedure is proposed to determine the interfacial shear strength of boundary layers. Results of loading and sliding experiments are used to calibrate the model parameters of the advanced friction model. In Chapter 5, the mixed lubrication friction model is used in FE forming simulations to demonstrate its applicability in metal forming processes. Two deep-drawing

applications are used for this purpose, i.e. a top-hat section and a cross-die product. The influence of boundary and mixed lubrication on the frictional behavior is demonstrated and a comparison is made between numerically and experimentally obtained punch force–displacement diagrams. In the final chapter, Chapter 6, conclusions and recommendations for future work are presented.

Chapter 2

Boundary lubrication friction modeling

A boundary lubrication friction model is proposed in this chapter. The model accounts for micro-mechanical friction mechanisms playing a role during sheet metal forming. Important friction mechanisms are outlined in Section 2.1. The friction model is based on a framework as described in Section 2.2. This framework includes models to describe surface changes of the workpiece material due to loading, straining and sliding actions. The theoretical background of these models is discussed in Section 2.3. A contact model is proposed in Section 2.4 to calculate friction under high fractional real contact areas, which accounts for both the influence of adhesion and ploughing on friction. The boundary lubrication friction model is implemented in an FE software code, enabling an accurate prediction of friction during sheet metal forming processes. Different strategies to implement the friction model in FE software codes are discussed in Section 2.5.

2.1 Boundary lubrication friction mechanisms

Boundary lubrication is the most common lubrication regime in sheet metal forming. In this regime, a normal contact load is solely carried by contacting surface asperities. The real area of contact, playing an important role in characterizing friction, relies on the roughness characteristics of both the tool and the workpiece surface. The workpiece surface is liable to changes due to flattening and roughening mechanisms, changing the real contact area.

The main flattening mechanisms during sheet metal forming, which tend to increase the real area of contact, are flattening due to normal loading, flattening due to sliding and flattening due to combined normal loading and deformation of the underlying bulk material. Roughening of asperities, observed during deformation of the bulk material without applying a normal load to the surface, tends to decrease the real area of contact [37, 65]. Most of the theoretical models describing the flattening behavior of asperities continue the pioneering work of Greenwood & Williamson [21], who proposed an elastic contact model that accounts for a stochastic description of rough surfaces. Over recent years, modifications have been made to this model to account for arbitrarily shaped asperities [81], plastically deforming asperities [53, 90], the interaction between asperities [81, 92] and the influence of stretching the underlying bulk material [69, 88]. Another technique to describe the flattening behavior of asperities relies on variational principles, first introduced by Tian & Bhushan [73]. Variational principles account for the fractal behavior of rough surfaces and include the long-range elastic coupling between contacting asperities. Elastic perfectly plastic contact conditions, including the unloading behavior of asperities, can be described using this approach. Besides the analytically based models described above, techniques can be used that account for a deterministic description of rough surfaces. In conjunction with, for example, FE techniques, realistic 3D surfaces can be examined under different loading and bulk straining conditions. Korzekwa et al. [35] was one of the first who adopted a plane strain FE approach to derive empirical relations for the description of asperity flattening under combined normal loading and straining of the bulk material. Although the FE approach has proven its applicability in many engineering applications, simplifying assumptions have to be made to ensure reasonable computation times with respect to modeling 3D rough surface textures.

Compared to normal loading only, a further increase in real contact area can be caused by sliding. Tabor [70] postulated that an increase in real contact area occurs before sliding occurs, which follows from the requirement to maintain a constant Von Mises stress at yielded contact points. This means that asperities

which were already plastically deformed by a given normal load, must grow when subjected to an additional tangential load. The increase in real contact area reduces the mean pressure at contact spots, accommodating the additional shear stresses. The increase in real contact area is referred to as junction growth [70], and is a known phenomenon for dry contacts [34, 44, 47, 48]. In this case, the required shear stress to initiate junction growth is introduced by the adhesion effect between dissimilar materials. For lubricated contacts, a similar effect such as junction growth has been observed by Emmens [15] and Lo & Tsai [39].

Friction is caused by ploughing and adhesion between contacting surface asperities. Wilson [84] and Challen & Oxley [9, 10] developed models to account for these effects. Wilson [84] treated the effect of adhesion and ploughing on friction separately, while Challen & Oxley took the combined effect of ploughing and adhesion into account. Challen & Oxley deduced slip-line fields to describe friction between one wedge-shaped asperity and a flat soft workpiece surface. Friction between multiple tool asperities and a flat soft counter surface can be obtained by describing the tool surface in terms of stochastic parameters [81]. To establish the translation from single asperity scale to multiple asperity scale, the summit height distribution of the tool, the asperity density and the mean radius of tool asperities is required. However, such ploughing models tend to lose their applicability under high fractional real contact areas. In these areas, tool asperities form contact patches which penetrate into the softer workpiece material [20, 46]. The frictional behavior of the contacting surfaces now depends on the geometry of the contact patches, rather than the geometry of the individual asperities. In addition, the required stochastic parameters are known to be dependent on the resolution of the measured surface texture [52]. That is, a different resolution of the surface scan can yield different stochastic parameters and hence, different model results. Ma et al. [41] proposed a multi-scale friction model that accounts for asperities forming contact patches under high fractional real contact areas. A deterministic surface description is used in their approach, which excludes the use of the summit height distribution, the asperity density and the mean asperity radius, and therefore excludes possible scale dependency problems.

2.2 Modeling approach

A boundary lubrication friction model is presented in this chapter. A friction framework has been developed that comprises three stages, see Figure 2.1. Existing, adapted and newly developed models have been implemented within

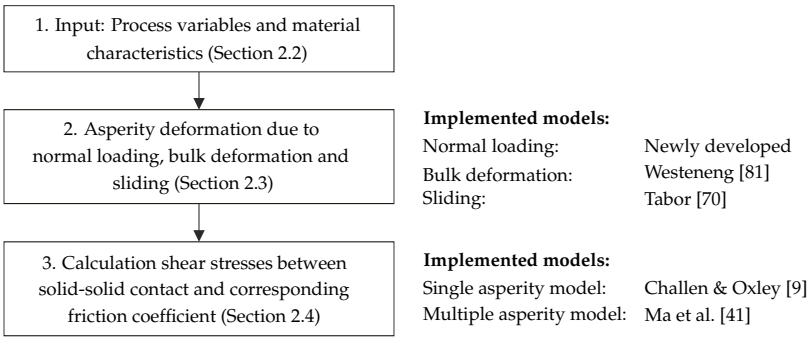

Figure 2.1 *Solving methodology.*

this framework. Because micro-mechanical friction models are generally regarded as too cumbersome to be used in large-scale FE simulations, the choice of the implemented models is a trade-off between accuracy and computational efficiency. This will yield a physically based friction model that is still computationally attractive for use in large-scale forming simulations.

In the first stage, the input step, surface characteristics and material properties are defined. A method to measure 3D surfaces and an experimental procedure to obtain the boundary layer shear strength of the interface is discussed in Chapter 4. Stage 2, the asperity deformation step, includes models to describe surface changes due to normal loading, deformation of the underlying bulk material and sliding (see Section 2.3). The models provide an expression for the fractional real contact area under the assumption of a flat tool surface and a rough workpiece surface. A non-linear work-hardening normal loading model has been developed in this research based on energy and volume conservation laws. Asperity flattening due to combined normal loading and deformation of the underlying bulk material has been described by the flattening model proposed by Westeneng [81]. The increase in real contact area due to sliding is captured by adopting the junction growth theory as proposed by Tabor [70]. The final stage, the friction evaluation step, accounts for the influence of ploughing and adhesion on friction. The contact model of Ma et al. [41], which was originally developed to describe friction in extrusion processes, has been adapted to model friction in metal forming processes (see Section 2.4). The calculated deformation of workpiece asperities in step 2 is used to adapt the deterministic description of the rough workpiece surface. The plateaus of the flattened workpiece asperities are assumed to be perfectly flat, in which the harder tool asperities are penetrating. The summation of shear forces acting on individual contact patches (collection of penetrating tool asperities) is used to finally obtain the friction coefficient.

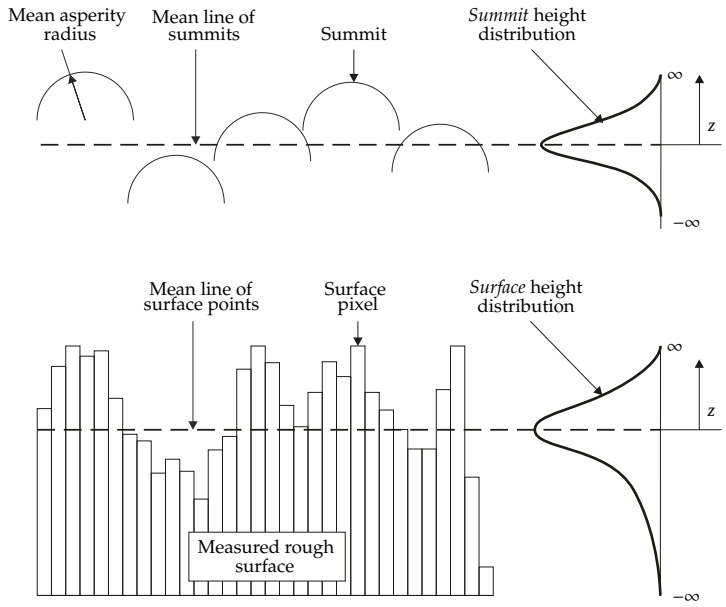

Figure 2.2 ***Top:*** *Schematic view summit height distribution (Greenwood & Williamson [21]).* ***Bottom:*** *Schematic view surface height distribution (Westeneng [81]).*

2.3 Modeling the deformation behavior of rough surfaces

The models implemented within the asperity deformation step are presented in this section. First, the newly developed normal loading model is discussed in Section 2.3.1. Next, the influence of sliding on the real contact area is outlined in Section 2.3.2. Finally, combined normal loading and deformation of the underlying bulk material is discussed in Section 2.3.3.

2.3.1 Flattening due to normal loading

In most of the contact models the asperity density, the mean asperity radius and the *summit* height distribution are used to calculate the amount of asperity deformation (see Figure 2.2 (top)), which was first introduced by Greenwood & Williamson [21]. A summit represents the peak of an asperity. The distribution of summit heights is represented in a *summit* height distribution. Summit based stochastic parameters depend on the resolution of the scanning method used.

That is, due to the fractal nature of rough surfaces, a finer scanning resolution will yield an increase in the summit density and a decrease in the mean asperity radius. Westeneng [81] proposed an ideal-plastic contact model that accounts for the *surface* height distribution instead of the *summit* height distribution to describe rough surfaces. The *surface* height distribution is based on measured surface points (see Figure 2.2 (bottom)), which excludes the use of summit based stochastic parameters.

The contact model proposed in this section is based on the normal loading model described by Westeneng. The newly developed contact model accounts for work hardening in deforming asperities. Moreover, compared to the contact model of Westeneng, the shear stress between crushing and raising asperities is accounted for.

Model assumptions

A rigid and perfectly flat tool is assumed contacting a soft and rough workpiece material. This is considered a valid assumption as the tool surface is in general much harder and smoother than the workpiece surface. The roughness texture of the workpiece is modeled by bars, which can represent arbitrarily shaped asperities, see Figure 2.3. The contact area of these bars is taken to be equal to the resolution of the measured (or digitally generated) 3D surface texture. Three stochastic variables are introduced to make the translation from micro-scale to macro-scale modeling of contact: The normalized surface height distribution function of the rough workpiece surface $\phi_w(z)$, the uniform raise of the non-contacting surface U_L (based on volume conservation) and the separation between the tool surface and the mean plane of the rough workpiece surface d_L. The suffix L in d_L and U_L refers to the normal loading step.

Material behavior

The crushing and raising behavior of deformed bars relies on a proper description of the material behavior. In this thesis, it is assumed that the maximum pressure a bar can carry equals the hardness H of the material. By approximation, the hardness H is given by:

$$H = B\sigma_y \tag{2.1}$$

with $B \approx 2.8$ for steel materials. The factor B is experimentally obtained using Brinell hardness tests by Tabor in [70]. It is noted that this relation holds for

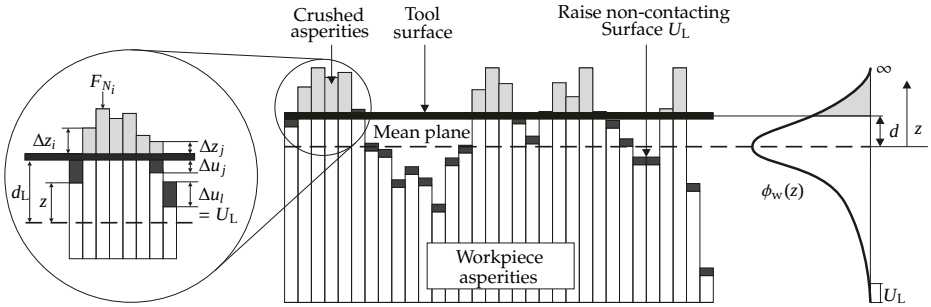

Figure 2.3 *A rough soft surface crushed by a smooth rigid surface.*

approximately ideal-plastic material behavior under a typical 3D stress state within the material, i.e. the stress state present during Brinell hardness testing. Hill [27] found that, for indenter angles larger than 45°, the same behavior holds for crushing a wedge-shaped asperity by a rigid flat tool as for penetrating a rigid wedge-shaped tool asperity into a soft flat surface. Changing the stress state within the material, as is introduced by non-linear hardening effects [67], changing the geometry of the indenter or adding an additional bulk strain to the material, will change the stress state and hence, the value of the factor B.

The physically based isothermal Bergström van Liempt [3, 78, 80] hardening relation is used to describe the yield strength σ_y. This relation decomposes the yield stress σ_y in a strain-dependent stress σ_{wh} and a strain-rate dependent stress σ_{dyn}. The relation accounts for the interaction processes between dislocations in cell structures including the changing shape of dislocation structures. Vegter [79] modified the Bergström van Liempt hardening relation for sheet metal forming processes, leading to the following formulation:

$$\sigma_y = \sigma_{wh} + \sigma_{dyn} \tag{2.2}$$

with

$$\sigma_{wh} = \sigma_{f0} + d\sigma_m \left(\beta_v (\varepsilon + \varepsilon_0) + \left\{1 - \exp\left[-\omega (\varepsilon + \varepsilon_0)\right]\right\}^n\right) \tag{2.3}$$

and

$$\sigma_{dyn} = \sigma_{v0} \left(1 + \frac{kT}{\Delta G_0} \ln \frac{\dot{\varepsilon}}{\dot{\varepsilon}_0}\right)^p \tag{2.4}$$

Table 2.1 *Nomenclature Bergström-Van Liempt hardening parameters.*

Symbol	
σ_{f0}	Initial static stress
$d\sigma_m$	Stress increment parameter
β_v	Linear hardening parameter
ω	Remobilization parameter
n	Hardening exponent
ε_0	Initial strain
$\dot{\varepsilon}_0$	Initial strain rate
σ_{v0}	Max. dynamic stress
T	Temperature
p	Dynamic stress power
ΔG_0	Activation energy
k	Boltzmann's constant

The nomenclature of the hardening parameters is given in Table 2.1. Although the strain-rate dependent stress can introduce an increase in yield strength of typically 10 – 20 % under sheet metal forming conditions, the influence of strain-rate dependency on the flattening behavior of asperities is not studied in this thesis.

The total plastic strain ε in the bars is related to the reference height λ. The reference height reflects a characteristic length, which is taken to be equal for all bars. Normal loading experiments have been conducted to obtain a value for the reference height by reducing the error between experimental and model results. Results of the experiments and the calibration procedure are discussed in Chapter 4.

By using the reference height λ, a definition for the strain ε can be derived for bars in contact with the tool and bars not in contact with the tool, see Equation (2.5) and Figure 2.3.

$$\varepsilon = \begin{cases} \ln\left(\left|1 + \dfrac{z - d_L}{\lambda}\right|\right) = \ln\left(\left|\dfrac{\lambda + z - d_L}{\lambda}\right|\right) & \text{for } z + U_L \geq d_L \text{ (contact)} \\ \ln\left(\left|1 + \dfrac{U_L}{\lambda}\right|\right) = \ln\left(\left|\dfrac{\lambda + U_L}{\lambda}\right|\right) & \text{for } z + U_L < d_L \text{ (no contact)} \end{cases} \tag{2.5}$$

Energy conservation

The amount of external energy must equal the internal energy in order to account for energy conservation. The amount of external energy is described by the energy required to crush contacting asperities. The internal energy is described by the energy absorbed by the crushed bars, the energy required to lift up the non-contacting bars and the energy required to shear bars which have a relative motion to each other. The variables used to describe the normal loading model are depicted in Figure 2.3. A distinction is made between bars in contact with the tool, bars which will come into contact due to the raise of asperities and bars which will not come into contact with the tool. The crushing height is described by the variable Δz while the raise of bars is described by the variable Δu. The number of bars in contact with the tool is indicated by N with corresponding crushing heights $\Delta z_i (i = 1, 2, ..., N)$. The number of bars coming into contact with the tool due to a raise of non-contacting asperities is described by N^* with crushing heights $\Delta z_j (j = 1, 2, ..., N^*)$. Hence, the total number of bars in contact with the tool after applying the normal load equals $N + N^*$. The number of bars which will not come into contact during the load step are indicated by N^{**} with corresponding raising heights $\Delta u_l (l = 1, 2, ..., N^{**})$. The total amount of bars $M = N + N^* + N^{**}$.

The external energy depends on the total number of bars in contact with the tool $(N + N^*)$. Normally, the non-contacting bars would raise with a distance Δu_l, but due to the presence of the tool, some of the bars are restricted to raise with a distance of Δu_j only (see bar j in Figure 2.3). A certain amount of external energy is required to prevent a raise of $\Delta z_j = \Delta u_l - \Delta u_j$. The energy required to indent contacting bars is given by:

$$W_{\text{ext}} = \sum_{i=1}^{N} F_{\text{N},i} \Delta z_i + \sum_{j=1}^{N^*} F_{\text{N},j} \Delta z_j = \sum_{k=1}^{N+N^*} F_{\text{N},k} \Delta z_k \tag{2.6}$$

with $F_{\text{N},k} = H_k \Delta A$ where H_k is obtained by $B\sigma_{\text{y},k}$, see Equation (2.1). ΔA represents the contact area of a single bar. In a later stage, the external and internal energy equations will be written in stochastic form for computational purposes. For this reason, Equation (2.6) is rewritten in the following form:

$$W_{\text{ext}} = F_{\text{N}} \omega \qquad \text{with} \qquad \omega = \frac{\sum_{k=1}^{N+N^*} F_{\text{N},k} \Delta z_k}{F_{\text{N}}} \tag{2.7}$$

In which F_{N} represents the total force and ω the indentation factor.

The internal energy is the energy absorbed by the crushed bars $W_{\text{int,ab}}$ and the energy required to raise the non-contacting bars $W_{\text{int,ri}}$. Shear stresses will be present between bars with a relative motion to each other, introducing an additional energy term $W_{\text{int,sh}}$ to the equilibrium equation:

$$W_{\text{int}} = W_{\text{int,ab}} + W_{\text{int,ri}} + W_{\text{int,sh}} \tag{2.8}$$

Knowing the definition of the deformation behavior of asperities (Equation (2.1)), the absorbed energy $W_{\text{int,ab}}$ over $N + N^*$ crushed bars can be written as:

$$W_{\text{int,ab}} = \sum_{k=1}^{N+N^*} H\Delta z_k \Delta A = B\Delta A \sum_{k=1}^{N+N^*} \sigma_{\text{y},k}\Delta z_k \tag{2.9}$$

or:

$$W_{\text{int,ab}} = B\gamma \qquad \text{with} \qquad \gamma = \Delta A \sum_{k=1}^{N+N^*} \sigma_{\text{y},k}\Delta z_k \tag{2.10}$$

Since the contact area of the bars is taken to be equal to the resolution of the scanned (or generated) surface texture, all bars have the same contact area ΔA. The yield strength $\sigma_{\text{y},k}(\varepsilon)$ is defined by Equation (2.2) with the strain ε defined by Equation (2.5). The change in $\sigma_{\text{y},k}$ should be accounted for as $\int \sigma_{\text{y},k}(\varepsilon)\text{d}\varepsilon$ to describe work-hardening effects properly. For computational efficiency, it is assumed that this integral can be approximated by the generalized midpoint rule, hence $\int \sigma_{\text{y},k}(\varepsilon)\text{d}\varepsilon = \sigma_{\text{y},k}(\xi\varepsilon)$. If $\xi = 0$ the initial yield strength is used, if $\xi = 1$ the yield strength at the end of the loading step is used. Since ξ only has an influence on the calculated strain ε, the same result could be obtained by changing the reference height λ (see Equation (2.5)). λ is obtained by calibrating experimental results to model results, see Chapter 4. The parameter ξ has therefore been set to one in the remainder of this research, knowing that the introduced error will be compensated by the calibration procedure of λ.

$W_{\text{int,ri}}$ is described by the sum of energy required to raise N^* bars which comes in contact with the tool after application of the normal load, and to raise N^{**} bars which do not come into contact with the tool:

$$\begin{aligned} W_{\text{int,ri}} &= \eta\left(\sum_{j=1}^{N^*} H\Delta u_j \Delta A + \sum_{l=1}^{N^{**}} H\Delta u_l \Delta A\right) \\ &= \eta B\Delta A\left(\sum_{j=1}^{N^*} \sigma_{\text{y},j}\Delta u_j + \sum_{l=1}^{N^{**}} \sigma_{\text{y},l}\Delta u_l\right) \end{aligned} \tag{2.11}$$

or:

$$W_{\text{int,ri}} = \eta B \beta \qquad \text{with} \qquad \beta = \Delta A \left(\sum_{j=1}^{N^*} \sigma_{\text{y},j} \Delta u_j + \sum_{l=1}^{N^{**}} \sigma_{\text{y},l} \Delta u_l \right) \tag{2.12}$$

Equation (2.11) includes a persistence parameter η which describes the amount of energy required to lift up the non-contacting bars [81]. A value of $\eta = 0$ means that no energy is required to raise the non-contacting bars, a value of $\eta = 1$ implies that the same amount of energy is required to raise bars as to crush bars. As for the reference height λ, the value of the persistence parameter will be calibrated as explained in Chapter 4.

The shear term $W_{\text{int,sh}}$ describes the shear energy between moving bars. Shear stresses only occur between bars which have a relative motion to each other. These are bars indented by the tool surface, surrounded by non-contacting bars which experience an upward raise due to volume consistency. The additional energy term is described by:

$$W_{\text{int,sh}} = \left(1 - \frac{A_{\text{real}}}{A_{\text{nom}}}\right) n_{\text{s}} \sum_{k}^{N+N^*} \tau_{\text{sh},k} A_{\text{sh},k} \Delta s_k \tag{2.13}$$

with n_{s} representing half of the number of surrounding bars (1 for a plane strain formulation and 2 for a 3D formulation), τ_{sh} the shear strength, A_{sh} the shearing area and Δs the shear distance. The shear distance is described by $\Delta s = z - d_{\text{L}} + U_{\text{L}}$, which represents the sum distance between a raising bar (U_{L}) and its neighboring crushing bar ($z - d_{\text{L}}$). It is assumed that the shearing area can be expressed as $A_{\text{sh}} = w\Delta s$ with w the width of a bar. The shear strength τ_{sh} can be expressed in terms of the yield stress by $\tau_{\text{sh}} = S\sigma_y$ with $S = 1/\sqrt{3}$ following the Von Mises yield criterion.

As mentioned before, the energy equations will be rewritten in stochastic form for computational reasons. By doing so, information about neighboring bars is lost, requiring an expression in terms of probabilities. The factor $1 - A_{\text{real}}/A_{\text{nom}}$ is therefore introduced in Equation (2.13) to account for the probability that an indented bar is actually surrounded by raising bars. A_{real} describes the real contact area ($(N + N^*)\Delta A$) and A_{nom} the nominal contact area ($M\Delta A$). If this factor is close to 0, almost all bars are indented and no relative motion will occur (there are no raising bars). On the other hand, if this factor is close to 1, the probability that an indented bar is surrounded by non-contacting bars is high (meaning that almost all crushed bars have raising neighboring bars).

Equation (2.13) can now be written as:

$$W_{\text{int,sh}} = S\left(1 - \frac{A_{\text{real}}}{A_{\text{nom}}}\right) n_{\text{s}} w \sum_{k}^{N+N^*} \sigma_{\text{y},k} \Delta s_k^2 \tag{2.14}$$

or:

$$W_{\text{int,sh}} = S\psi \qquad \text{with} \qquad \psi = \left(1 - \frac{A_{\text{real}}}{A_{\text{nom}}}\right) n_{\text{s}} w \sum_{k}^{N+N^*} \sigma_{\text{y},k} \Delta s_k^2 \tag{2.15}$$

The deterministic 3D rough surface texture is described by stochastic parameters to make an efficient translation from micro to macro contact modeling. The normalized surface height distribution $\phi_{\text{w}}(z)$ has been introduced for this purpose (see Figure 2.3). In the limit of an infinite number of bars, the following expressions hold:

$$\begin{aligned}
F_{\text{N}} &= BA_{\text{nom}} \int_{d_{\text{L}}-U}^{\infty} \sigma_{\text{y}}(z)\, \phi_{\text{w}}(z)\, \mathrm{d}z \\
\Delta A \sum_{i=1}^{N} \Delta z_i &= A_{\text{nom}} \int_{d_{\text{L}}}^{\infty} (z - d_{\text{L}})\, \phi_{\text{w}}(z)\, \mathrm{d}z \\
\Delta A \sum_{j=1}^{N^*} \Delta z_j &= A_{\text{nom}} \int_{d_{\text{L}}-U_{\text{L}}}^{d_{\text{L}}} (z - d_{\text{L}} + U_{\text{L}})\, \phi_{\text{w}}(z)\, \mathrm{d}z \\
\Delta A \sum_{j=1}^{N^*} \Delta u_j &= A_{\text{nom}} \int_{d_{\text{L}}-U_{\text{L}}}^{d_{\text{L}}} (d_{\text{L}} - z)\, \phi_{\text{w}}(z)\, \mathrm{d}z \\
\Delta A \sum_{l=1}^{N^{**}} \Delta u_l &= A_{\text{nom}} \int_{-\infty}^{d_{\text{L}}-U_{\text{L}}} U_{\text{L}} \phi_{\text{w}}(z)\, \mathrm{d}z \\
n_{\text{s}} w \sum_{k=1}^{N+N^*} \Delta s_k &= L_{\text{s}} \int_{d_{\text{L}}-U_{\text{L}}}^{\infty} (z - d_{\text{L}} + U_{\text{L}})\, \phi_{\text{w}}(z)\, \mathrm{d}z
\end{aligned} \tag{2.16}$$

with $A_{\text{nom}} = M\Delta A$ and $L_{\text{s}} = Mn_{\text{s}}w$.

The energy factors, in deterministic and stochastic form, can now be written as:

$$\begin{aligned}\omega &= \frac{\sum_{k=1}^{N+N^*} F_{\mathrm{N},k}\Delta z_k}{F_\mathrm{N}} \\ &= \frac{\int_{d_\mathrm{L}}^{\infty} \sigma_\mathrm{y}(z)(z-d_\mathrm{L})\phi_\mathrm{w}(z)\,\mathrm{d}z + \int_{d_\mathrm{L}-U_\mathrm{L}}^{d_\mathrm{L}} \sigma_\mathrm{y}(z)(z-d_\mathrm{L}+U_\mathrm{L})\phi_\mathrm{w}(z)\,\mathrm{d}z}{\int_{d_\mathrm{L}-U_\mathrm{L}}^{\infty} \sigma_\mathrm{y}(z)\phi_\mathrm{w}(z)\,\mathrm{d}z}\end{aligned} \tag{2.17}$$

$$\begin{aligned}\gamma &= \Delta A \sum_{k=1}^{N+N^*} \sigma_{\mathrm{y},k}\Delta z_k \\ &= A_\mathrm{nom}\left(\int_{d_\mathrm{L}}^{\infty} \sigma_\mathrm{y}(z)(z-d_\mathrm{L})\phi_\mathrm{w}(z)\,\mathrm{d}z + \int_{d_\mathrm{L}-U_\mathrm{L}}^{d_\mathrm{L}} \sigma_\mathrm{y}(z)(z-d_\mathrm{L}+U_\mathrm{L})\phi_\mathrm{w}(z)\,\mathrm{d}z\right)\end{aligned} \tag{2.18}$$

$$\begin{aligned}\beta &= \Delta A\left(\sum_{j=1}^{N^*} \sigma_{\mathrm{y},j}\Delta u_j + \sum_{l=1}^{N^{**}} \sigma_{\mathrm{y},l}\Delta u_l\right) \\ &= A_\mathrm{nom}\left(\int_{d_\mathrm{L}-U_\mathrm{L}}^{d_\mathrm{L}} \sigma_\mathrm{y}(z)(d_\mathrm{L}-z)\phi_\mathrm{w}(z)\,\mathrm{d}z + \int_{-\infty}^{d_\mathrm{L}-U_\mathrm{L}} \sigma_\mathrm{y}(z)U_\mathrm{L}\phi_\mathrm{w}(z)\,\mathrm{d}z\right)\end{aligned} \tag{2.19}$$

and:

$$\begin{aligned}\psi &= \left(1-\frac{A_\mathrm{real}}{A_\mathrm{nom}}\right) n_\mathrm{s} w \sum_{k=1}^{N+N^*} \sigma_{\mathrm{y},k}\Delta s_k^2 \\ &= L_\mathrm{s}\int_{-\infty}^{d_\mathrm{L}-U_\mathrm{L}} \phi_\mathrm{w}(z)\,\mathrm{d}z\left(\int_{d_\mathrm{L}-U_\mathrm{L}}^{\infty} \sigma_\mathrm{y}(z)(z-d_\mathrm{L}+U_\mathrm{L})^2\phi_\mathrm{w}(z)\,\mathrm{d}z\right)\end{aligned} \tag{2.20}$$

where the following relation has been used:

$$1-\frac{A_\mathrm{real}}{A_\mathrm{nom}} = 1-\alpha_\mathrm{L} = 1-\int_{d_\mathrm{L}-U_\mathrm{L}}^{\infty}\phi_\mathrm{w}(z)\,\mathrm{d}z = \int_{-\infty}^{d_\mathrm{L}-U_\mathrm{L}}\phi_\mathrm{w}(z)\,\mathrm{d}z \tag{2.21}$$

In which the fractional real contact area α_L has been introduced.

The variable ω can be regarded as an indentation factor while γ, β and ψ can be regarded as internal energy factors. The variable γ describes the energy required to crush contacting bars, β the energy required to raise non-contacting bars and ψ the energy required to shear bars which have a relative motion to each other.

All energy factors depend on the statistical parameters U_L (raise of bars) and d_L (separation between the tool surface and the mean plane of the rough surface). In addition, ω is a function of the normal forces acting on the bars $F_N(z)$. It is noted that an equal raise of bars U_L has been assumed, which corresponds to the experimental results of Pullen & Williamson [53].

Balancing the total internal energy (Equation (2.8)) with the external energy (Equation (2.7)) and introducing the nominal contact pressure p_{nom} defined as F_N/A_{nom}, finally gives:

$$p_{nom} = \frac{B}{A_{nom}}\left(\frac{\gamma}{\omega} + \eta\frac{\beta}{\omega}\right) + \frac{S}{A_{nom}}\frac{\psi}{\omega} \tag{2.22}$$

Volume conservation

Equation (2.22) provides the relation between the nominal contact pressure p_{nom}, the separation d_L and the constant raise of the non contacting surface U_L. Another equation is required to compute the separation d_L and raise U_L for a given normal load p_{nom}. Volume conservation is used for this purpose, which can be written as:

$$\sum_{i=1}^{N} \Delta z_i \Delta A = \sum_{l=1}^{N^{**}} \Delta u_l \Delta A + \sum_{j=1}^{N^{*}} \Delta u_j \Delta A \tag{2.23}$$

The equation for volume conservation can be written in stochastic form using the stochastic expressions as given in Equation (2.16):

$$\begin{aligned} A_{nom}\int_{d_L}^{\infty}(z-d_L)\,\phi_w(z)\,dz = A_{nom}\int_{-\infty}^{d_L-U_L} u(z)\,\phi_w(z)\,dz \\ + A_{nom}\int_{d_L-U_L}^{d_L}(d_L-z)\,\phi_w(z)\,dz \end{aligned} \tag{2.24}$$

Taking a constant raise U_L of the non-contacting asperities into account, Equation (2.24) can be rewritten as:

$$U_L(1-\alpha_L) = \int_{d_L-U_L}^{\infty}(z-d_L)\,\phi_w(z)\,dz \tag{2.25}$$

The separation d_L and the raise of the non-contacting surface U_L for a given normal pressure p_{nom} can be calculated by solving Equation (2.22) and Equation (2.25) simultaneously. Scheme 2.1 summarizes the equations to be

Solve U_L and d_L for a given p_{nom} such that:

$$p_{nom} - \frac{B}{A_{nom}}\left(\frac{\gamma}{\omega} + \eta\frac{\beta}{\omega}\right) + \frac{S}{A_{nom}}\frac{\psi}{\omega} = 0$$

$$U_L(1-\alpha_L) - \int_{d_L-U_L}^{\infty}(z-d_L)\,\phi_w(z)\,dz = 0$$

with the fractional real contact area α_L:

$$\alpha_L = \int_{d_L-U_L}^{\infty}\phi_w(z)\,dz$$

Output: U_L, d_L, α_L

Scheme 2.1 *Equations to solve U_L, d_L and α_L as function of p_{nom}.*

solved in the normal loading step. A Newton Raphson procedure has been used in this research to solve the non-linear set of equations.

2.3.2 Flattening due to normal loading + sliding

In this section, the normal loading model discussed in Section 2.3.1 is adapted to account for sliding effects, which increases the real contact area significantly (as will be demonstrated in Chapter 4). The initial value α_S^0 is obtained from the normal loading model (Section 2.3.1). The subscript S refers to the influence of sliding on the real contact area.

It is assumed that the increase in real contact area during sliding is caused by two mechanisms. First, the normal loading model assumes contact between a perfectly flat tool surface and a rough workpiece surface, see Figure 2.4 (left). Based on this assumption, energy equations are solved to meet force equilibrium between the applied load and the calculated real contact area. At a smaller scale, however, the tool surface is also rough and the harder tool asperities are penetrating into the softer (crushed) workpiece asperities, see Figure 2.4 (middle). If sliding occurs, only the frontal area of a penetrating tool asperity is actually in contact, see Figure 2.4 (right). Consequently, the real contact area must grow with a factor of approximately 2 in order to satisfy force equilibrium. It is assumed that the following relation holds:

$$\alpha_S^1 = 2\alpha_S^0 \tag{2.26}$$

Moreover, if asperities are already plastically deformed by a given normal load, they must grow when subjected to an additional tangential load (caused due to

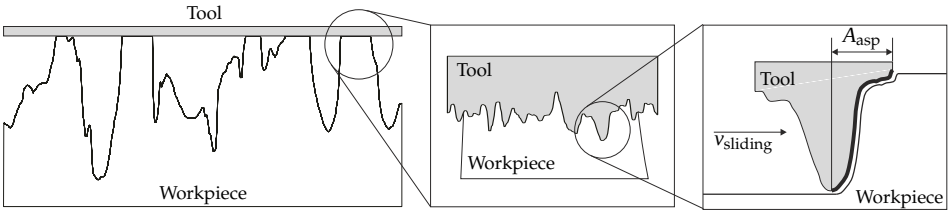

Figure 2.4 *Schematic view contacting tool asperities.* ***Left:*** *Rough crushed workpiece surface.* ***Middle:*** *Zoom-in on rough tool surface.* ***Right:*** *Zoom-in single asperity scale.*

sliding). In the literature, this mechanism is known as junction growth (see also Section 2.1). Based on the Von Mises yield criterion, Tabor derived the following relation to account for the influence of tangential loading on the real contact area:

$$\nu = \sqrt{1 + k\mu^2} \tag{2.27}$$

with ν the increase in fractional real contact area, μ the friction coefficient and k a constant shear factor. On theoretical grounds the constant k has a value 3 for a simple 2D body [70]. For a 3D contact situation there is no theoretical solution for k and hence, friction experiments are usually executed to determine this value. To find the increase in real contact area ν, an iterative scheme is required since the proposed relation relies on the friction coefficient $\mu(\alpha)$, see Scheme 2.2. To find the friction coefficient $\mu(\alpha)$, a deterministic ploughing model is adopted, as will be discussed in Section 2.4. Within an iteration step the real contact area is calculated by $\alpha_S^{n+1} = \nu^n \alpha_S^1$, by which the friction coefficient $\mu(\alpha_S)$ will change in the next iteration. The iterative procedure is repeated until $\left|\alpha_S^{n+1} - \alpha_S^n\right| < e$, where e is a predefined error threshold. If the error threshold is satisfied, the indentation d_S and raise of the surface U_S is solved from the definition of the real contact area (Equation (2.21)) and volume conservation (Equation (2.25)), see Scheme 2.2. A Newton Raphson procedure is used for this purpose. U_S and d_S are subsequently used to account for the effect of bulk deformation on the real contact area, see Section 2.3.3.

Input: α_S^0

Increase in α_S to satisfy force equilibrium:
$\alpha_S^1 = 2\alpha_S^0$

$n = 1$
while ($|e^n| >$ error) do
  Solve μ^n for α_S^n (Section 2.4)
  $\nu^n = \sqrt{1 + k(\mu^n)^2}$
  Update α_S:
  $\alpha_S^{n+1} = \nu^n \alpha_S^1$
  $e^n = |\alpha_S^{n+1} - \alpha_S^n|$
  $n = n + 1$
end while
$\alpha_S = \alpha_S^n$

Solve U_S and d_S for α_S such that:

$$\alpha_S - \int_{d_S - U_S}^{\infty} \phi_w(z)\,\mathrm{d}z = 0$$

$$U_S(1 - \alpha_S) - \int_{d_S - U_S}^{\infty} (z - d_S)\,\phi_w(z)\,\mathrm{d}z = 0$$

Output: U_S, d_S, α_S

Scheme 2.2 *Iterative scheme to solve ν, U_S, d_S and α_S.*

2.3.3 Flattening due to combined normal loading and stretching

When asperities are already in a plastic state due to normal loading, only a small stress in the underlying bulk material (perpendicular to the loading direction) initiates further plastic deformation of asperities. As a result, more indentation of contacting asperities will occur and hence, the real contact area will increase. In the literature this is known as the decrease in effective hardness due to bulk straining the underlying material [57, 69, 88]. The effective hardness H_{eff} is defined as:

$$H_{\text{eff}} = \frac{p_{\text{nom}}}{\alpha} \tag{2.28}$$

Westeneng [81] derived an analytical contact model to describe the influence of bulk straining on deforming, arbitrarily shaped, asperities. Analogue to the

normal loading model, this model considers contact between a flat hard surface and a soft rough surface. Plastic material behavior is assumed without work-hardening effects. The outcomes of the sliding model (U_S, d_S and α_S), as discussed in the previous section, are used as the initial values for U_ε^0, d_ε^0 and α_ε^0. The subscript ε indicates the variables that are bulk strain dependent.

Westeneng derived the following relation to describe the change in fractional real contact area α_ε as a function of the in-plane strain ε_p:

$$\frac{d\alpha_\varepsilon}{d\varepsilon_p} = lW\frac{d\alpha_\varepsilon}{d\left(U_\varepsilon - d_\varepsilon\right)} \tag{2.29}$$

in which W represents the velocity parameter, defined by:

$$W = \frac{v_a + v_b}{\dot{\varepsilon}_p l} \tag{2.30}$$

with v_a the downward velocity of crushing asperities, v_b the upward velocity of the non-contacting surface and l the mean half spacing between asperities:

$$l = \frac{1}{2\sqrt{\rho_w \alpha_\varepsilon}} \tag{2.31}$$

ρ_w describes the asperity density of the workpiece surface. A method to obtain the asperity density from measured 3D surface textures is discussed in Chapter 4. The definition for l is approximately true for surfaces with no particular roughness distribution. To describe the velocity parameter W an empirical relation is used, as is discussed at the end of this section.

The definition of the fractional real contact area (Equation (2.32)) is used to solve the differential equation in the right-hand side of Equation (2.29), see Equation (2.33).

$$\alpha_\varepsilon = \int_{d_\varepsilon - U_\varepsilon}^{\infty} \phi_w(z)\,dz \tag{2.32}$$

$$\frac{d\alpha_\varepsilon}{d\left(U_\varepsilon - d_\varepsilon\right)} = \frac{d}{d\left(U_\varepsilon - d_\varepsilon\right)} \int_{d_\varepsilon - U_\varepsilon}^{\infty} \phi_w(z)\,dz = \phi_w\left(d_\varepsilon - U_\varepsilon\right) \tag{2.33}$$

Substituting Equation (2.33) into Equation (2.29), yields:

$$\frac{d\alpha_\varepsilon}{d\varepsilon_p} = lW\phi_w\left(d_\varepsilon - U_\varepsilon\right) \tag{2.34}$$

To calculate the change in α_ε, the value of U_ε and d_ε needs to be solved simultaneously while ε_p is incrementally increased. Based on volume consistency and the fractional real contact area, α_ε, U_ε and d_ε can be obtained by following the procedure presented in Scheme 2.3. In this scheme, the Euler method is used to solve α_ε. A Newton Raphson procedure has been used to solve the corresponding values of U_ε and d_ε.

Input: ε_p, $\mathrm{d}\varepsilon_\mathrm{p}$, U_ε^0, d_ε^0, α_ε^0

$n = 0$, $\varepsilon^0 = 0$
while $\varepsilon_\mathrm{p} > \varepsilon^n$ do
  Solve $\mathrm{d}\alpha_\varepsilon^n$ for $\mathrm{d}\varepsilon_\mathrm{p}$:

$$\mathrm{d}\alpha_\varepsilon^n = \left(lW\phi_\mathrm{w}\left(d_\varepsilon^n - U_\varepsilon^n\right)\right)\mathrm{d}\varepsilon_\mathrm{p}$$

  Update α_ε

$$\alpha_\varepsilon^{n+1} = \alpha_\varepsilon^n + \mathrm{d}\alpha_\varepsilon^n$$

  Solve U_ε^{n+1} and d_ε^{n+1} for α_ε^{n+1} such that:

$$\alpha_\varepsilon^{n+1} - \int_{d_\varepsilon^{n+1}-U_\varepsilon^{n+1}}^{\infty} \phi_\mathrm{w}(z)\,\mathrm{d}z = 0$$

$$U_\varepsilon^{n+1}\left(1-\alpha_\varepsilon^{n+1}\right) - \int_{d_\varepsilon^{n+1}-U_\varepsilon^{n+1}}^{\infty} \left(z - d_\varepsilon^{n+1}\right)\phi_\mathrm{w}(z)\,\mathrm{d}z = 0$$

  $\varepsilon^{n+1} = \varepsilon^n + \mathrm{d}\varepsilon$
  $n = n + 1$
end while
$d_\varepsilon = d_\varepsilon^n$, $U_\varepsilon = U_\varepsilon^n$, $\alpha_\varepsilon = \alpha_\varepsilon^n$

Output: d_ε, U_ε, α_ε

Scheme 2.3 *Iterative scheme to solve U_ε, d_ε and α_ε.*

For readability purposes, the subscript ε will not be used in the remainder of this thesis, hence $\alpha = \alpha_\varepsilon$, $U = U_\varepsilon$ and $d = d_\varepsilon$.

Velocity parameter W

Time dependency is not accounted for within the proposed framework. Therefore, velocities are unknown and hence another definition for the velocity parameter W is required. Sutcliffe [69] performed slip-line analysis to describe

the deformation of wedge-shaped asperities under combined normal loading and straining of the underlying bulk material. Inherent to slip-line analysis, a plane strain state and rigid ideal plastic material behavior has been assumed. Based on slip-line results, Sutcliffe showed the relation between the velocity parameter W and the characteristic slip-line angle γ. γ is bounded by $0 \leq \gamma \leq \pi/2$ due to geometrical conditions. The expression of the slip-line angle is given by Sutcliffe in [69]:

$$\gamma = \frac{H_{\text{eff}}}{4k}(1 - \alpha_\varepsilon) \tag{2.35}$$

with k the shear strength of the workpiece material. The expression for k follows from the Von Mises yield criterion under pure shear, and is defined as $k = \frac{H}{B\sqrt{3}}$. H is the initial hardness of the material and B represents the hardness factor as described in Section 2.3.1. Based on the slip-line results presented in [69], Westeneng proposed in [81] the following semi-empirical relation to describe the velocity parameter W as a function of the fan angle γ:

$$W = -0.184 + 1.21\exp(1.47\gamma) \tag{2.36}$$

This expression is used in this work to solve the equations shown in Scheme 2.3.

2.4 Modeling the evolution of friction

Ma et al. [41] proposed a contact model that accounts for tool asperities forming contact patches under high fractional real contact areas. The model of Ma et al. was originally developed for extrusion processes, and is adapted to describe friction in sheet metal forming. First, the contact model of Challen & Oxley [9, 10] is outlined in Section 2.4.1. The model of Challen & Oxley is used to predict friction forces acting on individual contact patches. Next, the model of Ma et al. is discussed in Section 2.4.2 to describe the formation of contact patches between contacting surfaces. Finally, the total friction force is obtained by the individual contributions of all contact patches, see Section 2.4.3.

2.4.1 Single asperity friction model

Friction forces acting on individual contact patches are described by adopting the contact model of Challen & Oxley [9, 10]. Challen & Oxley deduced 2D slip-line fields, assuming a plane strain deformation state and ideal-plastic material behavior. The authors proposed relations describing the steady-state

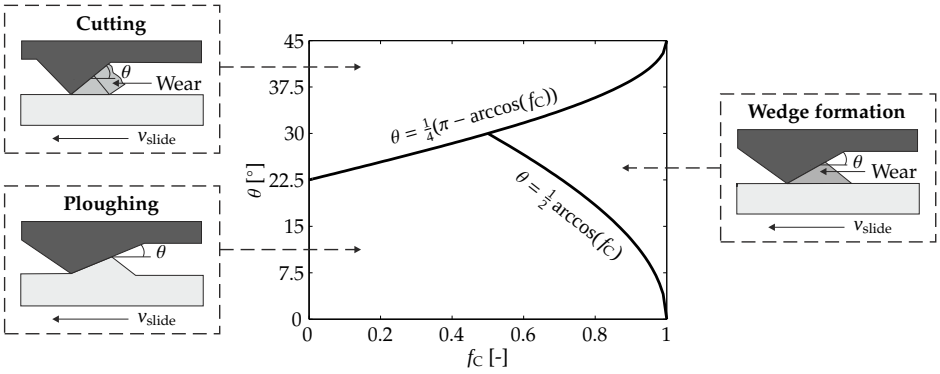

Figure 2.5 *Wear-mode diagram.*

friction between a wedge-shaped asperity indenting into a softer flat counter surface under cutting, ploughing and wear conditions. The active mode can be determined by so-called wear-mode diagrams [9, 28], see Figure 2.5. These diagrams describe friction modes as a function of the attack angle of a wedge-shaped asperity θ and the shear factor f_C, where the latter describes the shear strength of the interfacial boundary layer over the shear strength of the plastic deforming material (the workpiece material). A mathematical description of all regimes is required since different contact conditions occur during metal forming.

The cutting regime applies to sharp asperities that cause material to be removed in the form of chips and therewith creating a groove in the softer material. The expression for the friction coefficient μ in the cutting regime is given by Challen & Oxley in [9]:

$$\mu_{\text{cutting}} = \tan\left(\theta - \frac{1}{4}\pi + \frac{1}{2}\arccos\left(f_C\right)\right) \tag{2.37}$$

Ploughing is caused by blunt asperities causing material to shift to the sides of the created groove, expressed by Equation (2.38) [9].

$$\mu_{\text{ploughing}} = \frac{A_1 \sin\theta + \cos\left(\arccos\left(f_C - \theta\right)\right)}{A_1 \sin\theta + \sin\left(\arccos\left(f_C - \theta\right)\right)} \tag{2.38}$$

with:

$$A_1 = 1 + \frac{1}{2}\pi + \arccos\left(f_C\right) - 2\theta - 2\arcsin\left(\frac{\sin\left(\theta\right)}{\left(1 - f_C\right)^{1/2}}\right) \tag{2.39}$$

The wear regime is characterized by removal of deformed material producing

wear particles. The expression for the friction coefficient in this regime is given in [9]:

$$\mu_{\text{wear}} = \frac{\left\{1 - 2\sin A_2 + \left(1 - f_C^2\right)^{1/2}\right\}\sin\theta + f_C\cos\theta}{\left\{1 - 2\sin A_2 + \left(1 - f_C^2\right)^{1/2}\right\}\cos\theta - f_C\sin\theta} \tag{2.40}$$

with:

$$A_2 = 1 - \frac{1}{4}\pi - \frac{1}{2}\arccos f_C + \arcsin\left(\frac{\sin\theta}{(1 - f_C)^{1/2}}\right) \tag{2.41}$$

The value of the attack angle θ is determined based on the contact model proposed in the next section. The shear factor f_C is defined as τ/k. τ describes the shear strength of the interfacial boundary layer and k the shear strength of the plastic deforming material. The boundary layer shear strength τ is described by the following form:

$$\tau = C\left(\frac{p}{p_0}\right)^n \tag{2.42}$$

with the shear strength τ and the constant C in Pa. p describes the applied contact pressure and p_0 the reference pressure in Pa. Since full plasticity is assumed during ploughing, the contact pressure p equals the hardness H of the softer material, i.e. $\tau = C\,(H/p_0)^n$.

2.4.2 Multiple asperity friction model

The multiple asperity friction model relies on the projection of two deterministic rough surfaces onto each other. Since the model makes use of one-to-one pixel mapping, both surfaces should be equal in size and resolution. The surface texture of the workpiece material is adapted for the amount of flattening and raise of asperities, which is calculated from the flattening models discussed in Section 2.3, see Figure 2.6. The plateaus of the flattened workpiece asperities are assumed to be perfectly flat, in which the harder tool asperities are penetrating. The separation between the mean plane of the tool surface and the flattened peaks of the workpiece surface is calculated based on force equilibrium, obtained by the summation of the load carried by the formed contact patches.

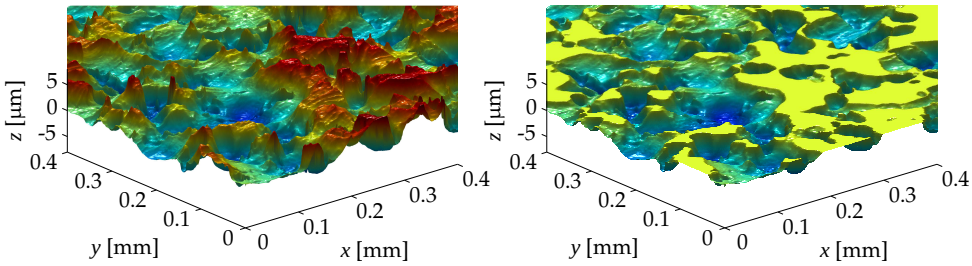

Figure 2.6 *3D surface textures.* ***Left:*** *Measured undeformed workpiece texture.* ***Right:*** *Impression of numerically deformed workpiece texture.*

Definition of contact patches

Contact patches are determined by binary image processing techniques. A contact patch is identified by a cluster of pixels (penetrating into the softer counter surface) connected together by either sharing pixel edges or by sharing pixel edges and pixel corner points, see Figure 2.7 (left). An elliptical paraboloid is fitted through the height data of the contact patch to determine the attack angle of the contact patch in sliding direction (see Figure 2.7 (middle) and Figure 2.7 (right)). The geometrical characteristics of the equivalent contact patch are indicated in Figure 2.7 (right).

Definition of elliptical paraboloids

The base of the elliptical paraboloid is approximated by an ellipse having the same normalized second central moments as the combined pixels of the patch [29], which is a common technique used in image processing. The geometrical parameters defining this ellipse are the major axis a and the minor axis b at the penetration depth ω, and the orientation angle φ between the horizontal and the major axis of the ellipse (see Figure 2.7 (right)).

The volume V_{ell} of the elliptical paraboloid, indented a distance ω into the softer counter surface, is defined as:

$$V_{\text{ell}} = \int_0^{\omega} \pi a'(z) b'(z) \mathrm{d}z = \int_0^{\omega} \frac{\pi a b}{\omega} z \mathrm{d}z = \frac{\pi a b \omega}{2} = \frac{A_{\text{ell}} \omega}{2} \tag{2.43}$$

with $a'(z) = a\sqrt{\frac{\omega - z}{\omega}}$ and $b'(z) = b\sqrt{\frac{\omega - z}{\omega}}$ the major and minor axis of the elliptical paraboloid as a function of z. The area of the base ellipse is $A_{\text{ell}} = \pi a b$. The height ω of the elliptical paraboloid is calculated such that the volume and contact area

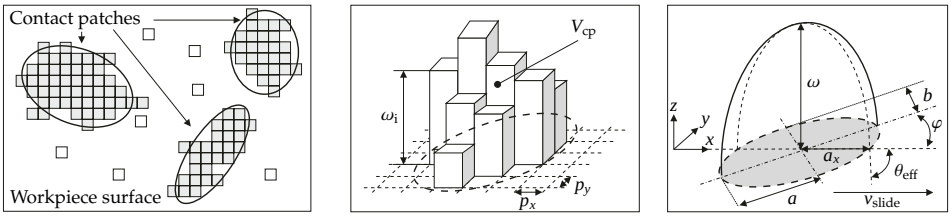

Figure 2.7 *Schematic view contact patches [41].* ***Left:*** *Definition contact patches.* ***Middle:*** *Volume of a contact patch.* ***Right:*** *Geometrical characteristics elliptical paraboloid.*

of the representative paraboloid are the same as the actual contact patch:

$$\omega = \frac{2V_{ell}}{A_{ell}} = \frac{2V_{cp}}{A_{cp}} = \frac{2p_x p_y \sum_{i=1}^{n} \omega_i}{n p_x p_y} = \frac{2}{n} \sum_{i=1}^{n} \omega_i \tag{2.44}$$

with n the number of discrete surface points spanned by the contact patch and p_x and p_y the pixel size of the rough tool surface. The suffix *ell* refers to the elliptical paraboloid, the suffix *cp* refers to the discrete contact patch.

The effective attack angle θ_{eff} between between the elliptical paraboloid and the counter surface, see Figure 2.7 (right), is defined as:

$$\theta_{eff} = \arctan\left(\frac{2\omega}{a_x}\right) \tag{2.45}$$

in which $\frac{2\omega}{a_x}$ is the tangent of the elliptical paraboloid in the direction of sliding (at $z = 0$). The characteristic length a_x relies on the geometry and orientation of the elliptical paraboloid, expressed by:

$$a_x = \frac{ab}{\sqrt{(b\cos\varphi)^2 + (a\sin\varphi)^2}} \tag{2.46}$$

From which the definition for the effective attack angle can be obtained:

$$\theta_{eff} = \arctan\left(\frac{2\omega\sqrt{(b\cos\varphi)^2 + (a\sin\varphi)^2}}{ab}\right) \tag{2.47}$$

The attack angle is used to obtain the friction force acting on one contact patch

according to Challen & Oxley. The model of Challen & Oxley describes ploughing and adhesion effects in a 2D plane strain expression, interpreting the effective attack angle θ_{eff} as an infinite cylinder. A translation is therefore required to capture the 3D nature of the contact patch into a 2D expression. To satisfy this requirement, Hokkirigawa & Kato [28] introduced the shape factor χ to modify the effective attack angle θ_{eff}, see Equation (2.48). They found values of $\chi = 0.8$ by indenting a spherical shaped indenter into brass, carbon steels and austenitic stainless steels. However, sliding experiments should be executed for every unique tool-workpiece combination for a reliable determination of the shape factor χ [28], reducing the differences found between experimental and theoretical results (see Chapter 4).

$$\theta = \arctan\left(\frac{2\omega\sqrt{(b\cos\varphi)^2 + (a\sin\varphi)^2}}{\chi ab}\right) \tag{2.48}$$

2.4.3 Calculation of friction coefficients

The above-mentioned procedure is carried out for all contact patches between the workpiece and the tool surface. Knowing the effective attack angle of each contact patch in the direction of sliding, the total friction force becomes the summation of all individual contributions. The coefficient of friction is obtained by dividing the total friction force by the total load carried by the contact patches:

$$\mu = \frac{F_{\text{w}}}{F_{\text{N}}} = \frac{\sum_{i=1}^{m} \mu_i(\theta_i) A_i H}{\sum_{i=1}^{m} A_i H} \tag{2.49}$$

with m the number of contact patches and μ_i the friction coefficient of a single contact patch. The friction coefficient μ_i is described by Equation (2.37), Equation (2.38) or Equation (2.40), depending on the attack angle θ (Equation (2.48)) and the shear factor f_{C}.

The anisotropy of contact patches is captured by this approach. That is, if a different orientation of asperities is used, the shape of the elliptical paraboloids will change. For isotropic surfaces, one would expect circular shaped base ellipses ($a \approx b$). For anisotropic surfaces, however, ellipses with a higher ellipticity ($a > b$) can be expected. This means that the direction of sliding has an influence on the evaluated friction coefficient. Recall Figure 2.7 (left), if the

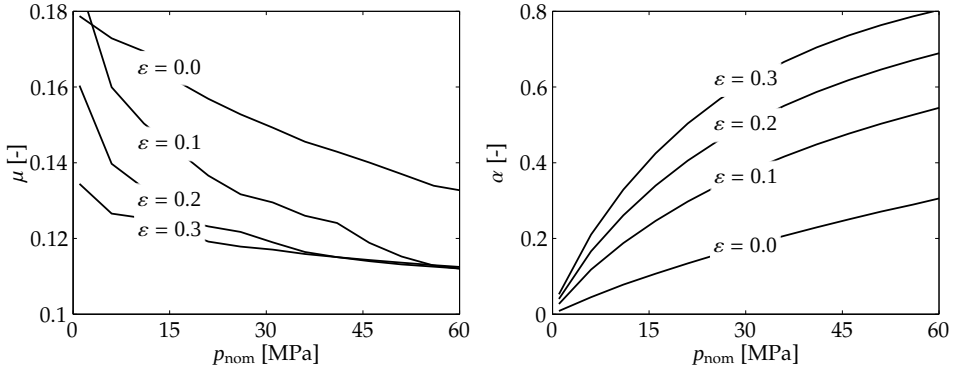

Figure 2.8 ***Left:*** *Development of the friction coefficient for different bulk strains.* ***Right:*** *Development of the real contact area for different bulk strains.*

sliding direction is changed from the positive x-axis to the positive y-axis different attack angles, and hence a different friction coefficient, will be found. Therefore, a direction dependent friction coefficient can be obtained by this friction model, which depends on the asperity orientation of both the tool and the workpiece surface.

2.5 Implementation in FE software codes

In Chapter 5, the application of the boundary lubrication friction model to two deep-drawing applications is discussed. The boundary lubrication friction model has been implemented in an FE software code for this purpose.

Two strategies can be chosen for the implementation. One way is to implement the friction model directly into the FE code, and solve the friction model once a node of the workpiece contacts the tool surface. However, this will yield a significant increase in computation time since all equations have to be solved for each node in contact, for every time step of the FE simulation. A computationally more efficient approach is to construct a friction matrix for a predefined range of nominal contact pressures exerted on the surface and strains occurring in the bulk material. This friction matrix can be used in an FE simulation, from which nodal friction coefficients are obtained based on linear interpolation. An additional advantage of this approach is the possibility to generate friction matrices for specific metal-lubricant combinations. A friction matrix has to be constructed only once for such a specific combination, after which it can be used to describe friction in different FE forming simulations.

Figure 2.8 (left) shows calculated friction coefficients for a pressure range of 1-60 MPa using a bulk strain of 0 %, 10 %, 20 % and 30 %. The material and surface parameters used for the friction analysis are discussed in Chapter 4. The non-smooth development of friction coefficients is introduced by the deterministic nature of the ploughing model (see Section 2.4). Increasing the nominal contact pressure p_{nom} or increasing the bulk strain ε both result in decreasing friction coefficients, which can be attributed to the increase in real contact area, see Figure 2.8 (right). Contact patches are joining together for increasing real contact areas resulting in a decrease in effective attack angles and a decrease in the number of active contact patches. Smaller attack angles yield less resistance against sliding, resulting in lower friction coefficients. The influence of the nominal contact pressure on calculated friction coefficients is further discussed in Chapter 4.

The strain in the bulk material is obtained by normal shell or solid elements during the forming simulation, and is subsequently used to find nodal friction coefficients from the friction matrix. The nominal contact pressure is calculated by the contact algorithm of the FE software.

Closure

A boundary lubrication friction model has been developed based on a modular approach. Micro-mechanical friction models, describing both the change in surface topography and the evolution of friction have been implemented within this framework. Friction matrices on user-defined metal-lubricant combinations can be generated, enabling the implementation in FE software. The extension of the proposed framework to account for friction in the mixed-lubrication regime is discussed in the next chapter.

Chapter 3

Mixed lubrication friction modeling

In this chapter, a friction model is proposed that enables the prediction of friction in the mixed lubrication regime. The boundary lubrication friction model presented in Chapter 2 has been coupled to a hydrodynamic friction model for this purpose. First, a general introduction to mixed lubrication modeling is given in Section 3.1 and Section 3.2. Next, the theoretical background of the mixed lubrication friction model is discussed in Section 3.3. To solve the differential equations governed by the mixed lubrication model, an interface element has been developed. The FE formulation and the implementation in an existing FE software code is presented in Section 3.4. Finally, the interface element has been applied to several 1D and 2D fluid flow test cases to demonstrate the performance of the developed element. Results on thick film, thin film and mixed lubrication test cases are discussed in Section 3.5.

3.1 Modeling lubrication in metal forming

Four main lubrication regimes can be defined to describe lubricant flow under metal forming conditions [83]. The lubrication regime is called the boundary lubrication regime if the normal load is totally carried by contacting surface asperities. Hydrodynamic stresses within the lubricant do not affect friction in this regime. Therefore, friction can be described by the boundary lubrication friction model as proposed in Chapter 2. In the remaining regimes, the load is either totally carried by the lubricant (thick film and thin film lubrication regime) or partly carried by the lubricant and partly carried by contacting surface asperities (mixed lubrication regime). These lubrication regimes are distinguished by the ratio between the fluid film thickness h and the composite RMS surface roughness S_q [83]. The lubrication regime is called the thick film lubrication regime for $h/S_q > 10$, the thin film lubrication regime for $3 < h/S_q < 10$ and the mixed lubrication regime for $h/S_q < 3$.

The contact load is carried completely by the lubricant in the thin film and thick film lubrication regime. Friction in the thick film lubrication regime relies on the rheological properties of the lubricant, and follows from viscous shear stresses at the fluid-solid interfaces. The hydrodynamic pressure distribution within the lubricant can be calculated from the Reynolds equation. The basic differential equations governed by the Reynolds equation was first derived by Reynolds in [55] for incompressible fluids, and formed the foundation for calculations of thick film lubricated systems. The Reynolds equation can be derived from the Navier–Stokes equations and continuity equations if assumed that the lubricant flow is laminar, the film thickness h is thin compared to the contact zone, the lubricant is Newtonian, zero-slip occurs at the fluid–solid interfaces and that surfaces are smooth.

In the thin film lubrication regime, the Reynolds equation loses its applicability due to the influence of surface roughness on fluid flow. Patir & Cheng [49, 50] proposed an averaged form of the Reynolds equation which considers the combined roughness of mating surfaces. The averaged Reynolds equation describes the average pressure and shear driven flow between rough surfaces by using so-called flow factors. Flow factors can be obtained from numerical flow simulations [1, 49] which inspired many researchers to derive flow factor expressions applicable in the thin film and the mixed lubrication regime.

In the mixed lubrication regime, part of the load is carried by contacting surface asperities and part of the load is carried by the lubricant. Friction mechanisms active in both the boundary lubrication regime and thin film lubrication regime act simultaneously in this regime [83]. Surface changes due

to asperity deformations influence the load-carrying capacity of the lubricant [83, 84]. As for the thin film lubrication regime, the averaged Reynolds equation can be used to calculate the load-carrying capacity of the lubricant. Flow factors determined under high fractional real contact areas should be used in this case. As an example, flow factors under severe contact conditions have been proposed by Lo [38] for porous media, by Wilson & Chang [86] for simple longitudinal saw-tooth asperities and by Wilson & Marsault [87] for more realistic surfaces with different height distributions.

3.2 FE techniques in lubrication technology

Most of the existing methods to solve the (averaged) Reynolds equation are derived for a particular forming process. For these cases, external process parameters like e.g. tooling radii, sheet thickness and size of the lubrication zone appear explicitly in the lubrication equations. Moreover, the lubrication analysis is generally split into an inlet zone, controlling the formation of the lubricant film, and a working zone, describing lubricant flow underneath the tooling of the forming process. This approach was first introduced by Wilson & Wang [89]. Wilson & Wang demonstrated their approach by a hydrodynamically-lubricated stretch forming process. The same approach has been adopted to describe lubricated strip-rolling processes in Wilson & Sheu [64], hemispherical punch stretching in Martinet & Chabrand [43] and axisymmetric cup drawing in Karupannasamy et al. [33]. For 2D forming processes, this approach has proved its applicability, however, the applicability is bounded by the process for which the method is developed and becomes extremely complicated for 3D forming processes.

In order to describe lubricant flow during 3D non-stationary forming processes, a more general formulation is required. A reliable approach can be obtained by making a coupling between the (already existing) FE mesh of a forming simulation and a discretized finite element form of the (averaged) Reynolds equation (sharing the same nodal locations). Solving the Reynolds equation by adopting an FE approach finds its first application in bearing mechanics, see for example Booker & Huebner [5]. Hu & Liu [30] first adopted this approach to describe a thick film lubricated steady-state strip rolling process. They solved the Reynolds equation by using an arbitrary Lagrangian Eulerian (ALE) formulation of the Reynolds Equation. Yang & Lo [91] applied the FE method to solve thin film lubrication problems during axisymmetric cup stretching. Boman & Ponthot [4] proposed a more general form of the (ALE) FE formulation of

the averaged Reynolds equation, making the description of arbitrary forming processes possible. As for the other cases, Boman & Ponthot considered contact conditions occurring in the thick film and/or thin film lubrication regime, excluding possible mixed lubrication friction during forming.

3.3 Development of a mixed lubrication friction model

A mixed lubrication friction model is proposed in this section. First, a method to describe lubricant flow in the mixed lubrication regime is presented in Section 3.3.1. The hydrodynamic friction model requires a definition for the fluid film thickness which is related to the amount of asperity deformation in Section 3.3.2. Finally, a methodology to solve shear stresses active between the fluid–solid and solid–solid interfaces is discussed in Section 3.3.3.

3.3.1 Lubricant flow in the mixed lubrication regime

The Reynolds equation describes the hydrodynamic pressure distribution in a fluid film for a given gap between two smooth surfaces. The 2D Reynolds equation for incompressible fluids can be written in tensorial form as [24, 55]:

$$\underbrace{\nabla \cdot \left(\frac{h^3}{12\eta} \nabla p_{\text{lub}} \right)}_{\text{Poiseuille}} = \underbrace{\nabla \cdot \left(\frac{h\,(\mathbf{v}_1 + \mathbf{v}_2)}{2} \right)}_{\text{Couette}} + \underbrace{\frac{\partial h}{\partial t}}_{\text{Squeeze}} \tag{3.1}$$

with $\nabla = \left(\frac{\partial}{\partial x}, \frac{\partial}{\partial y} \right)$, $p_{\text{lub}} = p_{\text{lub}}(x, y)$ the hydrodynamic pressure within the fluid, η the dynamic viscosity and $h = h(x, y)$ the fluid film thickness. Velocities of the fluid are described in a Eulerian framework, where $\mathbf{v_1} = \mathbf{v_1}(x, y)$ represents the velocity in x- and y-direction at the lower surface and $\mathbf{v_2} = \mathbf{v_2}(x, y)$ the velocity in x- and y-direction at the upper surface. The velocity components and the coordinate system used are shown in Figure 3.1. The terms governed by the Reynolds equation describe Poiseuille flow, Couette flow and squeeze flow. The Poiseuille term represents the pressure driven flow, the Couette term the induced flow by sliding velocities and the squeeze term the induced flow by the change in fluid film thickness. The squeeze term can be decomposed in a normal squeeze term and a translate squeeze term, as is discussed in Section 3.4. The term expressing

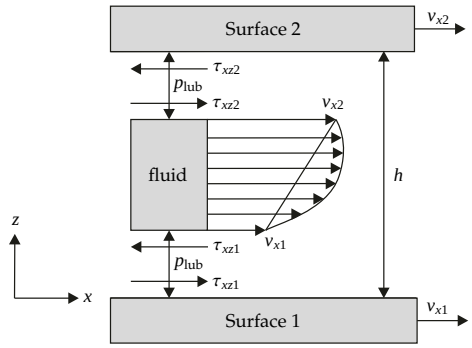

Figure 3.1 *Schematic view hydrodynamic equilibrium.*

Couette flow can be written as:

$$\nabla \cdot \left(\frac{h\left(\mathbf{v}_1 + \mathbf{v}_2\right)}{2} \right) = \underbrace{\frac{\mathbf{v}_1 + \mathbf{v}_2}{2} \cdot \nabla h}_{\text{Physical wedge}} + \underbrace{\frac{h}{2} \nabla \cdot \left(\mathbf{v}_1 + \mathbf{v}_2\right)}_{\text{Stretch}} \tag{3.2}$$

describing flow introduced by the translation of inclined surfaces (physical wedge term) and flow introduced due to stretching of the surfaces (stretch term). Viscous shear stresses acting in a Newtonian fluid are obtained by [24]:

$$\boldsymbol{\tau} = \eta \frac{\partial \mathbf{v}}{\partial z} = \frac{\eta\left(\mathbf{v}_2 - \mathbf{v}_1\right)}{h} + \frac{(2z - h)}{2} \nabla p_{\text{lub}} \tag{3.3}$$

with $\boldsymbol{\tau} = \left(\tau_{xz}, \tau_{yz}\right)$ the shear stress as a function of the height z (at a specific xy-location). The shear stresses acting at the lower and upper solid–fluid interfaces are:

$$\begin{aligned} \boldsymbol{\tau}_1(z = 0) &= \frac{\eta\left(\mathbf{v}_2 - \mathbf{v}_1\right)}{h} - \frac{h}{2} \nabla p_{\text{lub}} \\ \boldsymbol{\tau}_2(z = h) &= \frac{\eta\left(\mathbf{v}_2 - \mathbf{v}_1\right)}{h} + \frac{h}{2} \nabla p_{\text{lub}} \end{aligned} \tag{3.4}$$

with $\boldsymbol{\tau}_1$ shear stresses acting on the lower surface and $\boldsymbol{\tau}_2$ shear stresses acting on the upper surface. See Figure 3.1 for the definition of shear stress components.

Influence of roughness on fluid flow

Surface roughness will disturb fluid flow in the mixed lubrication regime [85]. The averaged Reynolds equation, first introduced by Patir & Cheng in [49], has

been used in this work to account for surface roughness. The averaged Reynolds equation can be written as [30, 87]:

$$\nabla \cdot \left(\frac{h^3}{12\eta} \mathbf{\Phi}_\mathrm{p} \cdot \nabla p_\mathrm{lub} \right) = \nabla \cdot \left(\frac{h\,(\mathbf{v}_1 + \mathbf{v}_2)}{2} + \frac{S_\mathrm{q}}{2} (\mathbf{v}_1 - \mathbf{v}_2) \cdot \mathbf{\Phi}_\mathrm{s} \right) + \frac{\partial h}{\partial t} \tag{3.5}$$

with $\mathbf{\Phi}_\mathrm{p}$ and $\mathbf{\Phi}_\mathrm{s}$ both second order tensors and S_q the composite RMS surface roughness of the undeformed surfaces. $\mathbf{\Phi}_\mathrm{p}$ compensates for the average pressure flow between rough surfaces. Values of $\mathbf{\Phi}_\mathrm{p}$ larger than unity reflect the channeling effect of valleys running in flow direction, while values lower than unity reflect the blocking effect of ridges running perpendicular to the flow direction [87]. The term in Equation (3.5) covering the flow factor $\mathbf{\Phi}_\mathrm{s}$ accounts for additional flow transport due to sliding between rough surfaces. Values of $\mathbf{\Phi}_\mathrm{s}$ other than zero reflect the ability of a rough surface to carry lubricant in its valleys. The flow factors become $\mathbf{\Phi}_\mathrm{p} \rightarrow \mathbf{I}$ and $\mathbf{\Phi}_\mathrm{s} \rightarrow \mathbf{0}$ in the case of smooth surfaces ($h/S_\mathrm{q} \rightarrow \infty$). For this situation, the averaged Reynolds equation reduces to the standard form of the Reynolds equation.

Shear flow factors can be used to compensate shear stresses at the fluid–solid interface. These flow factors are defined such that the mean hydrodynamic shear stress is given in terms of average quantities [50]. In this research, it is assumed that lubricant shear stresses will only have a limited influence on the total shear stress. Since lubricant flow is only considered in the mixed lubrication regime, a large part of the total shear stress will be introduced by interacting surface asperities. For this reason, the influence of roughness on lubricant shear stresses has not been studied in this research.

3.3.2 Relating fluid flow to the amount of asperity deformation

To solve the hydrodynamic pressure distribution p_lub from the averaged Reynolds equation, a definition for the fluid film thickness h is required. In this work, the fluid film thickness is related to the amount of asperity deformation obtained from the boundary lubrication friction model (see Chapter 2). The fluid film thickness is derived from the fluid present in non-contacting pockets and the fluid film area, in which it is assumed that there is enough lubricant to fill the pockets. The fluid volume present in non-contacting pockets is described by Equation (3.6), in which the rough surface texture and the lubricant are discretized by bars (see Figure 3.2).

$$V_\mathrm{lub} = \sum_{i=1}^{Q} (d_i - z_i - U_i)\, \Delta A_i = \Delta A \sum_{i=1}^{Q} (d_i - z_i - U_i) \tag{3.6}$$

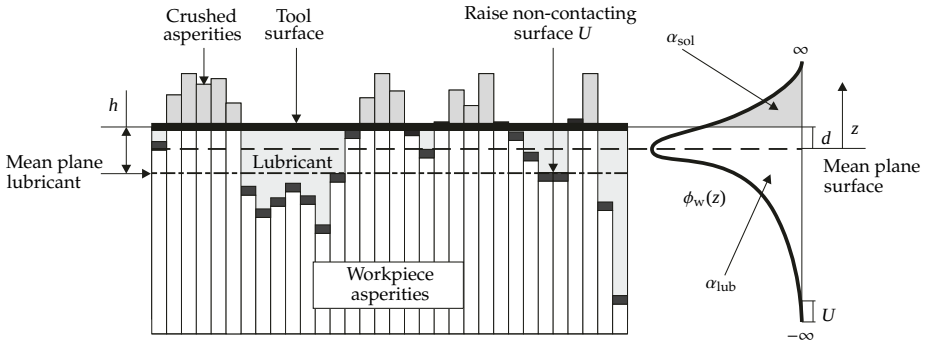

Figure 3.2 *Fluid film thickness between rough surfaces.*

With ΔA the contact area of a single bar. The dimensions of the bars are obtained from the resolution of a scanned (or digitally generated) surface texture. This means that all bars have the same contact area ΔA. The parameter Q in Equation (3.6) represents the number of non-contacting bars, z is the height of bars with respect to the mean plane of the rough surface, d is the crushing height of asperities and U represents the raise of the non-contacting surface. Values of d and U are obtained from the micro-mechanical contact models implemented in the boundary lubrication friction model, see Section 2.3.

The fluid volume has been rewritten in stochastic form by making use of the stochastic expressions given in Equation (2.16). By doing so, the fluid volume becomes:

$$V_{\text{lub}} = A_{\text{nom}} \int_{-\infty}^{d-U} (d - U - z)\, \phi_{\text{w}}(z)\, \mathrm{d}z \tag{3.7}$$

with $A_{\text{nom}} = M\Delta A$ where M represents the total number of bars. The normalized surface height distribution ϕ_{w} has been introduced to calculate the fluid film thickness in an efficient way. The integral from $-\infty$ till $d - U$ represents the part of the surface height distribution ϕ_{w} which is not in contact with the tool, see Figure 3.2. The fluid film area A_{lub}, required to calculate the fluid film thickness h, in deterministic and stochastic form reads:

$$A_{\text{lub}} = \sum_{i=1}^{Q} \Delta A_i = A_{\text{nom}} \int_{-\infty}^{d-U} \phi_{\text{w}}(z)\, \mathrm{d}z \tag{3.8}$$

Knowing the fluid volume V_{lub} and the fluid film area A_{lub}, the fluid film thickness

h is obtained by:

$$h = \frac{V_{\text{lub}}}{A_{\text{lub}}} = \frac{A_{\text{nom}} \int_{-\infty}^{d-U} (d - U - z)\, \phi_{\text{w}}(z)\, \mathrm{d}z}{A_{\text{nom}} \int_{-\infty}^{d-U} \phi_{\text{w}}(z)\, \mathrm{d}z} = \frac{\int_{-\infty}^{d-U} (d - U - z)\, \phi_{\text{w}}(z)\, \mathrm{d}z}{\int_{-\infty}^{d-U} \phi_{\text{w}}(z)\, \mathrm{d}z} \tag{3.9}$$

The fluid film thickness can be calculated as a function of x and y by following this approach, with x and y representing the location within the lubrication zone. The lubrication zone reflects the contact zone in which the lubricant is active. When the fluid film thickness distribution in the lubrication zone is known, the averaged Reynolds equation can be solved accordingly, as is discussed in detail in Section 3.4.

Starvation of lubricant

So far, it has been assumed that enough lubricant is present to fill the non-contacting pockets. In reality, however, a pre-defined amount of lubricant is applied to the workpiece surface. Starvation of lubricant occurs depending on the amount of lubricant. Starvation means that there is not enough lubricant to fill the pockets, meaning that the applied load is totally carried by contacting surface asperities.

The mean fluid film thickness h_{applied} can be calculated from the amount of lubricant applied to the surface. The required fluid film thickness h to fill the non-contacting pockets is calculated from Equation (3.9). If $h > h_{\text{applied}}$ insufficient lubricant is present to fill the asperity pockets, meaning that starvation of lubricant will occur. For this situation the hydrodynamic pressure p_{lub} is set to zero and the load is completely carried by solid–solid contact. Friction in this case is described by the boundary lubrication friction model.

3.3.3 Describing friction in the mixed lubrication regime

To describe mixed lubrication friction, a coupling has been made between the hydrodynamic friction model and the boundary lubrication friction model as presented in Chapter 2. The 3-step methodology to describe boundary lubrication friction has been extended to account for lubrication effects, see Scheme 3.1. The mixed lubrication friction model has been implemented in an FE software code. This means that the friction model is called each increment of a forming simulation for each node of the blank in contact with the tooling. Four steps can be distinguished in Scheme 3.1, which are discussed next.

```
Input:  μ^0 = μ_ini,  h^0 = h_ini,  v_1^0 = 0,  v_2^0 = 0

n = 1
Do (n=1:nr of FE increments)

   Step 1:
     Solve p_nom^n and p_lub^n:
       Solve p_nom^n, v_1^n and v_2^n from μ^(n-1) by the
        FE contact algorithm
       Solve p_lub^n from v_1^(n-1), v_2^(n-1) and h^(n-1)
        (see Section 3.4.3)
     Calculate fluid shear stresses τ_1^n and τ_2^n
      from Equation (3.4)

   Step 2:
     Solve d^n, U^n, α_sol^n and τ_sol^n from the
      boundary lubrication friction model (Chapter 2)

   Step 3:
     Calculate τ_tot^n from Equation (3.11)

   Step 4:
     Update field variables:
       Calculate μ^n from Equation (3.13)
       Calculate h^n from Equation (3.9)

  n = n + 1
end do
```

Scheme 3.1 *Solving methodology for p^n_{sol}, p^n_{lub}, h^n and μ^n. Executed each increment of an FE simulation.*

Step 1:

The nominal contact pressure p_{nom} and lubricant pressure p_{lub} are solved and used to calculate mixed lubrication friction. The nominal contact pressure p_{nom} follows from the contact algorithm present within the FE software. Within this research, a penalty based contact algorithm has been used. To solve the lubricant pressure distribution p_{lub}, the nodal fluid film thickness h and the nodal velocities of the fluid $\mathbf{v}_1$ and $\mathbf{v}_2$ are taken from the previous increment. The initial fluid film thickness h_{ini} is obtained from the roughness profile of an undeformed surface. To solve the hydrodynamic pressure distribution an FE approach has

been adopted, which is discussed in detail in Section 3.4. Viscous shear stresses at the fluid–solid interfaces ($\boldsymbol{\tau}_1$ and $\boldsymbol{\tau}_2$) are calculated based on the obtained hydrodynamic pressure distribution using Equation (3.4).

Step 2:

The pressure in the lubricant p_{lub}, the nominal contact pressure p_{nom} and the strain within the workpiece material ε_{p} are used to solve the boundary lubrication friction model. The strain ε_{p} is the nodal strain within the blank material and is calculated by shell or solid elements during the forming simulation. The nominal contact pressure p_{nom} and lubricant pressure p_{lub} are used from step 1 to calculate the load carried by contacting surface asperities, i.e. $p_{\text{sol}} = p_{\text{nom}} - p_{\text{lub}}$. Based on p_{sol}, the deformation of asperities (d and U) and the shear stresses τ_{sol} between contacting asperities are determined (see Section 2.4).

Step 3:

The hydrodynamic shear stresses $\boldsymbol{\tau}_1$ and $\boldsymbol{\tau}_2$ (step 1) and the shear stress between contacting surface asperities τ_{sol} (step 2) are used to obtain the total shear stress τ_{tot}. τ_{tot} is a scalar value and will be used to calculate the friction coefficient μ in step 4. The Euclidean norm of hydrodynamic shear stresses acting on the lower surface ($\boldsymbol{\tau}_1$) is used to calculate the nodal shear stress τ_{lub}:

$$\tau_{\text{lub}} = \sqrt{\tau_{xz1}^2 + \tau_{yz1}^2} \tag{3.10}$$

From which the total shear stress τ_{tot} can be obtained by:

$$\tau_{\text{tot}} = \tau_{\text{sol}} + \alpha_{\text{lub}} \tau_{\text{lub}} \tag{3.11}$$

Lubricant shear stresses are obtained on a global level by using the averaged fluid film thickness h. Therefore, τ_{lub} is multiplied with the fractional fluid film area α_{lub} (defined by Equation (3.12)), representing shear stresses in the fluid film pockets. Shear stresses between contacting asperities have already been defined on a local level, multiplication with α_{sol} is therefore not required.

$$\alpha_{\text{lub}} = \int_{-\infty}^{d-U} \phi_{\text{w}}(z)\, \mathrm{d}z \tag{3.12}$$

Step 4:

Based on the applied load and obtained shear stresses, the nodal friction

coefficient μ is calculated by:

$$\mu = \frac{\tau_{\text{tot}}}{p_{\text{nom}}} \tag{3.13}$$

Finally, based on the amount of asperity deformation, the average fluid film thickness h is updated using Equation (3.9).

The fluid film thickness h and the friction coefficient μ are used in the next increment to solve the mixed lubrication friction model. In order to solve the hydrodynamic pressure distribution p_{lub}, an FE approach has been used. The FE discretization of the mixed lubrication model is discussed in the next section.

3.4 Development of a mixed lubrication interface element

To solve the mixed lubrication friction model an interface element has been developed. First, the modeling approach is discussed in Section 3.4.1. Next, the theoretical background of the discretized FE model is presented in Section 3.4.2. The FE formulation has been implemented within an FE software code, which is discussed in Section 3.4.3.

3.4.1 Modeling approach

The hydrodynamic part of the mixed lubrication model is solved based on an FE approach and implemented in an existing contact formulation. A 3D wedge-shaped interface element has been used for this purpose [31, 77], describing the incremental x-, y-, and z-displacements in its corner nodes. The coupling of the hydrodynamic friction part with the interface element is realized by adding additional pressure degrees of freedom (d.o.f.) to the element. The pressure degrees of freedom describe the hydrodynamic pressure distribution p_{lub} within the element. Nodal locations and degrees of freedom are shown in Figure 3.3.

To obtain the displacement and hydrodynamic pressure fields, the following set of equations has to be solved for each increment of the FE simulation:

$$\mathbf{K}_{\text{c}} \cdot \mathbf{du} = \mathbf{R}_{\text{F}} \tag{3.14}$$

$$\mathbf{K}_{\text{p}} \cdot \Delta\mathbf{P} = \mathbf{R}_{\text{p}} \tag{3.15}$$

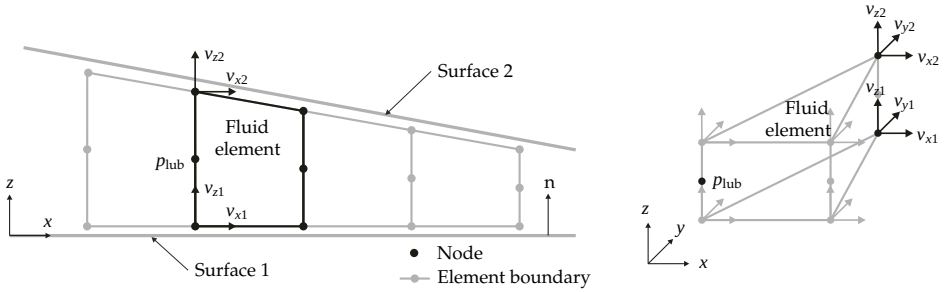

Figure 3.3 *Schematic view mixed lubrication interface elements.* ***Left:*** *Side view showing the elements.* ***Right:*** *3D view showing degrees of freedom.*

In which $\mathbf{K}_c$ is the contact stiffness matrix excluding hydrodynamic effects, $\mathbf{K}_p$ the fluidity matrix describing the pressure variation, $\mathbf{R}_F$ the residual force vector and $\mathbf{R}_p$ the residual fluidity vector describing film entrainment and squeeze effects. Equation (3.14) represents a non-linear set of equations which is solved based on a Newton–Raphson scheme within each incremental step. The total incremental displacement field $\Delta\mathbf{u}_n$, during the Newton–Raphson procedure, is updated by:

$$\Delta\mathbf{u}_i^n = \Delta\mathbf{u}_{i-1}^n + \mathrm{d}\mathbf{u} \tag{3.16}$$

where $\Delta u_i^0 = 0$. n represents the number of the increment and i the number of the Newton–Raphson iteration. As will be shown in this section, Equation (3.15) represents a linear set of equations. This means that the incremental hydrodynamic pressure field $\Delta\mathbf{P}$ is only solved in the first iteration of the Newton–Raphson procedure, and will remain unchanged during subsequent iterations.

It is noted that the equations describing contact conditions in the interface element and the equations describing the lubricant pressure build-up are decoupled. This means that the influence of the load-carrying capacity of the lubricant on the nodal displacements of the interface elements is not accounted for. Nodal velocities are required to calculate the right-hand side-vector $\mathbf{R}_p$. The nodal velocity is calculated by $\mathbf{v} = \Delta\mathbf{u}/\Delta t$, with $\Delta\mathbf{u}$ the incremental displacement found in the previous time increment. The hydrodynamic pressure distribution $\Delta\mathbf{P}$ is used to update the nodal fluid film thickness h, the shear stresses τ_{lub} and τ_{sol} and the friction coefficient μ at the end of an increment. The procedure used to update these variables is discussed in Section 3.3. In the current section, the hydrodynamic part of the friction model is rewritten in FE form to obtain the fluidity matrix $\mathbf{K}_p$ and residual fluidity vector $\mathbf{R}_p$.

3.4.2 FE formulation mixed lubrication friction model

The averaged Reynolds equation is solved to obtain the hydrodynamic pressure distribution in the lubricant. The lubricant film thickness h, obtained from the amount of asperity deformation as described in Section 3.3, is used to calculate the spatial and time derivatives in Equation (3.5). The lubricant film thickness is defined from a fixed point on surface 1 projected to surface 2, see Figure 3.3 for the definition of surfaces and the coordinate system used. Since this point is attached to a moving boundary, the squeeze term $\frac{\partial h}{\partial t}$ in Equation (3.5) is described by the material time derivative $\frac{\mathrm{D}h}{\mathrm{D}t}$ plus a spatial derivative taking into account the motion of surface 1, hence:

$$\frac{\partial h}{\partial t} = \frac{\mathrm{D}h}{\mathrm{D}t} - \mathbf{v}_1 \cdot \nabla h \tag{3.17}$$

The $\frac{\mathrm{D}h}{\mathrm{D}t}$ term and $-\mathbf{v}_1 \cdot \nabla h$ term are referred to as the normal squeeze term and the translate squeeze term, respectively. Substituting Equation (3.17) in Equation (3.5) and rewriting all terms in weak form, the discretized form of the averaged Reynolds equation yields:

$$\begin{aligned}\int_A \delta p_{\mathrm{lub}} \nabla \cdot \left(\frac{h^3}{12\eta} \mathbf{\Phi}_{\mathrm{p}} \cdot \nabla p_{\mathrm{lub}} \right) \mathrm{d}A = \\ \int_A \delta p_{\mathrm{lub}} \left[\nabla \cdot \left(\frac{h\,(\mathbf{v}_1 + \mathbf{v}_2)}{2} + \frac{S_{\mathrm{q}}}{2} (\mathbf{v}_1 - \mathbf{v}_2) \cdot \mathbf{\Phi}_{\mathrm{s}} \right) \right] + \\ \int_A \delta p_{\mathrm{lub}} \left(\frac{\mathrm{D}h}{\mathrm{D}t} - \mathbf{v}_1 \cdot \nabla h \right) \mathrm{d}A \qquad \forall\ \delta p_{\mathrm{lub}}\end{aligned} \tag{3.18}$$

In which δp_{lub} describes the virtual pressure field and A the contact zone where the lubricant is active (lubrication domain). Differentiation by parts of the left-hand side and the first term in the right-hand side gives:

$$\begin{aligned}-\int_A \nabla \delta p_{\mathrm{lub}} \cdot \frac{h^3}{12\eta} \mathbf{\Phi}_{\mathrm{p}} \cdot \nabla p_{\mathrm{lub}}\, \mathrm{d}A + \int_A \nabla \cdot \left(\delta p_{\mathrm{lub}} \frac{h^3}{12\eta} \mathbf{\Phi}_{\mathrm{p}} \cdot \nabla p_{\mathrm{lub}} \right) \mathrm{d}A = \\ \int_A \delta p_{\mathrm{lub}} \left(\frac{(\boldsymbol{v}_1 + \boldsymbol{v}_2)}{2} \cdot \nabla h + \frac{h}{2} \nabla \cdot (\boldsymbol{v}_1 + \boldsymbol{v}_2) \right) \mathrm{d}A + \\ \int_A \delta p_{\mathrm{lub}} \left(\frac{S_{\mathrm{q}}}{2} (\boldsymbol{v}_1 - \boldsymbol{v}_2) \cdot \nabla \cdot \mathbf{\Phi}_{\mathrm{s}} + \frac{S_{\mathrm{q}}}{2} \mathbf{\Phi}_{\mathrm{s}}^{\mathrm{T}} : \nabla (\boldsymbol{v}_1 - \boldsymbol{v}_2) \right) \mathrm{d}A + \\ \int_A \delta p_{\mathrm{lub}} \left(\frac{\mathrm{D}h}{\mathrm{D}t} - \mathbf{v}_1 \cdot \nabla h \right) \mathrm{d}A \qquad \forall\ \delta p_{\mathrm{lub}}\end{aligned} \tag{3.19}$$

Rearranging terms and introducing the relative velocity $\mathbf{u} = \mathbf{v_1} - \mathbf{v_2}$ and the sum velocity $\mathbf{v} = \mathbf{v_1} + \mathbf{v_2}$, Equation (3.19) can be written as:

$$
\begin{aligned}
-\int_A \nabla\delta p_{\text{lub}} \cdot \frac{h^3}{12\eta}\mathbf{\Phi}_{\text{p}} \cdot \nabla p_{\text{lub}}\,\mathrm{d}A + \int_C \delta p_{\text{lub}} \frac{h^3}{12\eta}\mathbf{\Phi}_{\text{p}} \cdot \nabla p_{\text{lub}} \cdot \mathbf{n}\,\mathrm{d}C = \\
\int_A \delta p_{\text{lub}} \left(\frac{-\boldsymbol{u}}{2} \cdot \nabla h + \frac{S_{\text{q}}}{2}\boldsymbol{u} \cdot \nabla \cdot \mathbf{\Phi}_{\text{s}} + \frac{S_{\text{q}}}{2}\mathbf{\Phi}_{\text{s}}^{\text{T}} : \nabla \boldsymbol{u} \right) \mathrm{d}A + \\
\int_A \delta p_{\text{lub}} \frac{h}{2} \nabla \cdot \boldsymbol{v}\,\mathrm{d}A + \int_A \delta p_{\text{lub}} \frac{\mathrm{D}h}{\mathrm{D}t}\,\mathrm{d}A \qquad \forall\ \delta P
\end{aligned}
\tag{3.20}
$$

The $\int_C \mathrm{d}C$ term in Equation (3.20) is evaluated over the boundary C of the domain A, referred to as q. $\mathbf{n}$ represents the outward-pointing unit normal vector on the boundary C. q equals zero if the fluid flow is continuous and the lubricant pressure is prescribed at the boundary of the lubrication domain A. That is, $\delta p_{\text{lub}} = 0$ at locations where the lubricant pressure is prescribed. Since both conditions are satisfied in the proposed FE discretization, the term q is not accounted for in the remainder of this research.

The lubrication domain A is discretized by a number of elements in an FE formulation, see Figure 3.3. To make the spatial discretization of the variables p_{lub}, $\mathbf{v}$ and $\mathbf{u}$, the interpolation matrix $\mathbf{N}$ (containing linear shape functions) is introduced:

$$
\begin{aligned}
p_{\text{lub}} &= N^\beta P^\beta, \\
\mathbf{v} &= N^\beta \mathbf{V}^\beta, \\
\mathbf{u} &= N^\beta \mathbf{U}^\beta, \\
\dot{h} &= N^\beta \dot{H}^\beta
\end{aligned}
\tag{3.21}
$$

Where P^β ,$\mathbf{V}^\beta$, $\mathbf{U}^\beta$ and $\dot{H}^\beta$ are functions of the d.o.f.'s for node β. The $\dot{H}$ term describes the material time derivative, i.e. $\dot{H} = \frac{\mathrm{D}h}{\mathrm{D}t}$.

The discretized form of the averaged Reynolds equation is obtained by substituting Equation (3.21) into Equation (3.20). Galerkin's method is used to interpolate the virtual pressure and velocity fields, hence:

$$
-\delta P^\beta \left(K_{\text{p}}^{\beta\gamma} P^\gamma - \mathbf{K}_{\text{v}}^{\beta\gamma} \cdot \mathbf{V}^\gamma - \mathbf{K}_{\text{u}}^{\beta\gamma} \cdot \mathbf{U}^\gamma - K_{\text{h}}^{\beta\gamma} \dot{H}^\gamma \right) = 0 \qquad \forall\ \delta P
\tag{3.22}
$$

with:

$$
\begin{aligned}
K_{\mathrm{p}}^{\beta\gamma} &= \int_A \frac{h^3}{12\eta} \left(\mathbf{B}^{\beta}\right)^{\mathrm{T}} \cdot \mathbf{\Phi}_{\mathrm{p}} \cdot \mathbf{B}^{\gamma} \, \mathrm{d}A \\
\mathbf{K}_{\mathrm{v}}^{\beta\gamma} &= \frac{1}{2} \int_A h N^{\beta} \mathbf{B}^{\gamma} \, \mathrm{d}A \\
\mathbf{K}_{\mathrm{u}}^{\beta\gamma} &= \frac{1}{2} \int_A \left(-N^{\beta} \nabla h N^{\gamma} + \frac{S_{\mathrm{q}}}{2} N^{\beta} \nabla \cdot \mathbf{\Phi}_{\mathrm{s}} N^{\gamma} + \frac{S_{\mathrm{q}}}{2} N^{\beta} \left(\mathbf{\Phi}_{\mathrm{s}}\right)^{\mathrm{T}} \cdot \mathbf{B}^{\gamma} \right) \mathrm{d}A \\
K_{\dot{\mathrm{h}}}^{\beta\gamma} &= \int_A N^{\beta} N^{\gamma} \, \mathrm{d}A
\end{aligned}
\tag{3.23}
$$

with:

$$
\mathbf{B}^{\beta} = \nabla N^{\beta} \tag{3.24}
$$

To describe the film viscosity η, a uniform distribution throughout the element has been assumed. The tensors $K_{\mathrm{p}}^{\beta\gamma}$, $\mathbf{K}_{\mathrm{v}}^{\beta\gamma}$, $\mathbf{K}_{u}^{\beta\gamma}$ and $K_{\dot{\mathrm{h}}}^{\beta\gamma}$ in Equation (3.22) are called the fluidity tensors and relate to the pressure variation ($K_{\mathrm{p}}^{\beta\gamma}$), film entrainment ($\mathbf{K}_{\mathrm{v}}^{\beta\gamma}$ and $\mathbf{K}_{\mathrm{u}}^{\beta\gamma}$) and squeeze effect ($K_{\dot{\mathrm{h}}}^{\beta\gamma}$).

3.4.3 Implementation in FE software codes

The discretized averaged Reynolds equation has been rewritten in incremental form to solve the set of equations given in Equation (3.15). This means that the increase in fluid film pressure $\Delta\mathbf{P}$ is calculated per incremental step, and updated at the end of the step ($\mathbf{P}^n = \mathbf{P}^{n-1} + \Delta\mathbf{P}^n$), with n the number of the increment. To solve $\Delta\mathbf{P}$, the fluid film thickness and velocity terms are used from the previous increment and treated as knowns in the current increment (see also Section 3.3). This is a valid approach as long as the incremental step is sufficiently small. By doing so, the $\Delta\mathbf{P}$ term is the only unknown degree of freedom. Equation (3.22) can now be written as:

$$
\begin{aligned}
-\delta P^{\beta} K_{\mathrm{p}}^{\beta\gamma} \Delta P^{\gamma,n} =& \delta P^{\beta} \left(K_{\mathrm{p}}^{\beta\gamma} P^{\gamma,n-1} + \mathbf{K}_{\mathrm{v}}^{\beta\gamma} \cdot \mathbf{V}^{\gamma,n-1} + \right. \\
& \left. \mathbf{K}_{\mathrm{u}}^{\beta\gamma} \cdot \mathbf{U}^{\gamma,n-1} + K_{\dot{\mathrm{h}}}^{\beta\gamma} \dot{H}^{\gamma,n-1} \right) \\
K_{\mathrm{p}}^{\beta\gamma} \Delta P^{\gamma,n} =& R_{\mathrm{p}}^{\beta} \qquad \forall\ \delta P
\end{aligned}
\tag{3.25}
$$

All terms governed by the fluidity matrix $\mathbf{K}_{\mathrm{p}}$ and residual fluidity vector $\mathbf{R}_{\mathrm{p}}$ in Equation (3.15) are now known. The contact stiffness matrix $\mathbf{K}_{\mathrm{c}}$ and residual force vector $\mathbf{R}_{\mathrm{F}}$ follow from the mechanical part of the interface element. The calculated

hydrodynamic pressure distribution $\Delta\mathbf{P}$ is used to update the fluid film thickness h and friction coefficient μ as discussed in Section 3.3. These variables are then used in the next increment to determine the incremental pressure increase ΔP as discussed in this section.

3.5 Thick film, thin film and mixed lubrication test cases

The interface element described in the previous section has been applied to multiple 1D and 2D fluid flow test cases. Results of the test cases are discussed to demonstrate the correct functioning of the interface element. Results of thick film lubrication and thin film lubrication test cases are discussed in Section 3.5.1 and Section 3.5.2, respectively. The capability of the interface element to describe friction in the boundary lubrication and the mixed lubrication regime is illustrated by generating Stribeck curves under different process conditions, as is discussed in Section 3.5.3.

3.5.1 Modeling thick film lubricant flow

Numerical results have been compared with 1D fluid flow test cases for which the analytical solution is known. For these test cases, the fluid film thickness h has been prescribed instead of calculated by the amount of asperity deformation. By doing so, the interface element as developed in Section 3.3 can be used to describe thick film and thin film lubricant flow. Side leakage is neglected to mimic 1D fluid flow, meaning that the natural boundary conditions for the hydrodynamic pressure p_{lub} are used at $y = 0$ and $y = w$ and that the hydrodynamic pressure is prescribed to be zero at $x = 0$ and $x = l$ (see Figure 3.4 (left) and Table 3.1 for the nomenclature). Two test cases are used to validate the different terms of the Reynolds equation. The first case describes the pressure driven flow (Poiseuille flow) activated by shear induced flow (Couette flow), see Figure 3.4 (left). The second case describes the Poiseuille flow activated by the squeeze effect, see Figure 3.6 (left). Model parameters are given in Table 3.1.

Fixed-incline slider bearing

The first case describes a fixed-incline slider bearing, consisting of two nonparallel plane surfaces separated by an oil film, see Figure 3.4 (left). The lower plane moves with a constant velocity while the upper surface remains stationary.

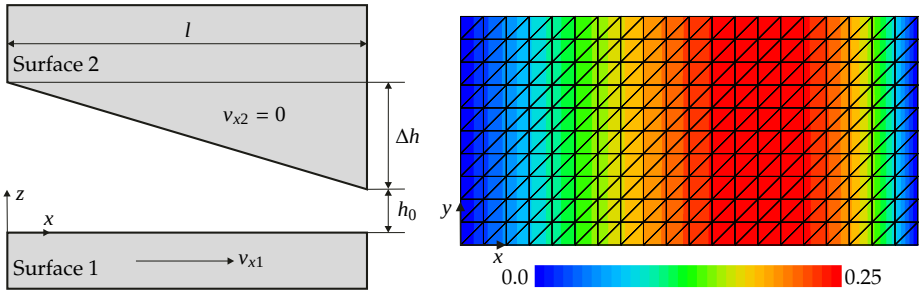

Figure 3.4 *Test case 1.* ***Left:*** *Schematic view fixed-incline slider bearing.* ***Right:*** *Numerical (non-dimensional) pressure distribution (top view).*

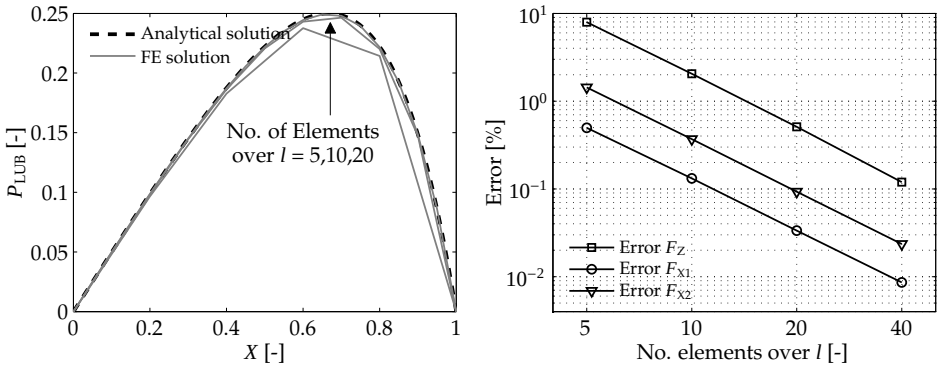

Figure 3.5 *Test case 1.* ***Left:*** *Pressure distribution for different mesh densities.* ***Right:*** *Error between numerical and analytical results.*

The inclination of the planes form a converging oil film, generating a pressure build-up within the lubricant if a motion in the direction of the physical wedge is present.

The hydrodynamic pressure distribution p_{lub} and shear forces f_{x1} and f_{x2} can be written in non-dimensional form as given by Hamrock et al. [24]:

$$P_{\text{LUB}} = \frac{p_{\text{lub}} \Delta h^2}{\eta v_{x1} l}, \tag{3.26}$$

$$F_{\text{X}i} = \frac{f_{xi} \Delta h}{\eta v_{x1} l} \tag{3.27}$$

with $i = 1, 2$ representing the lower and upper surface. The analytical solution for the non-dimensional hydrodynamic pressure distribution P_{LUB} and the total

Table 3.1 *Parameters FE interface test cases.*

Length	l	10 mm
Width	w	5 mm
Outlet height	h_0	2 mm
Height increase	Δh	2 mm
x velocity lower surface	v_{x1}	10 mm/s
z velocity upper surface	v_{z2}	10 mm/s
Dynamic viscosity	η	0.06 Pa s

non-dimensional shear force acting on the lower and upper bounding surface (F_{X1} and F_{X2}) is given by Equation (3.28) and Equation (3.29), respectively [24].

$$P_{\mathrm{LUB}} = \frac{6X(1-X)}{(H_0+1-X)^2(1+2H_0)} \tag{3.28}$$

$$\begin{aligned} F_{X1} &= 4\ln\left(\frac{H_0}{H_0+1}\right) + \frac{6}{1+2H_0} \\ F_{X2} &= 2\ln\left(\frac{H_0}{H_0+1}\right) + \frac{6}{1+2H_0} \end{aligned} \tag{3.29}$$

with:

$$H_0 = \frac{h_0}{\Delta h} \qquad \text{and} \qquad X = \frac{x}{l} \tag{3.30}$$

The numerically predicted pressure build-up underneath the wedge for an element mesh of 10×20 ($w \times l$) elements is shown in Figure 3.4 (right). As expected, a pressure increase underneath the wedge is predicted. A comparison between the analytical and numerical hydrodynamic pressure build-up is shown in Figure 3.5 (left). 4 different mesh densities have been used to obtain the numerical results, i.e. 5, 10, 20 and 40 elements over the contact length l and 10 elements over the contact width w. It can be seen that the numerical results converge to the analytical solution using a finer mesh density. The error between the analytical and numerical results for both the total normal force F_{Z} (calculated from the pressure distribution) and shear forces F_{X1} and F_{X2} is shown in Figure 3.5 (right). The error definition is given in Equation (3.31), with $\hat{F}$ the numerically obtained force and i referring to Z, $X1$ or $X2$. Both shear forces and the normal force converge quadratically to the analytical solution for an increasing mesh density (slope of the log-log graph equals -2). This comparison

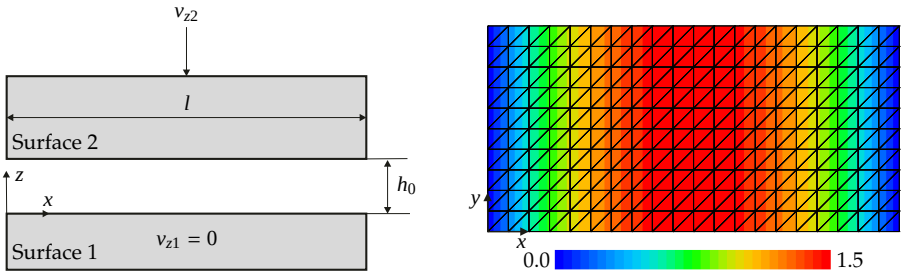

Figure 3.6 *Test case 2.* ***Left:*** *Schematic view of parallel-surface squeeze film bearing.* ***Right:*** *Numerical (non-dimensional) pressure distribution (top view).*

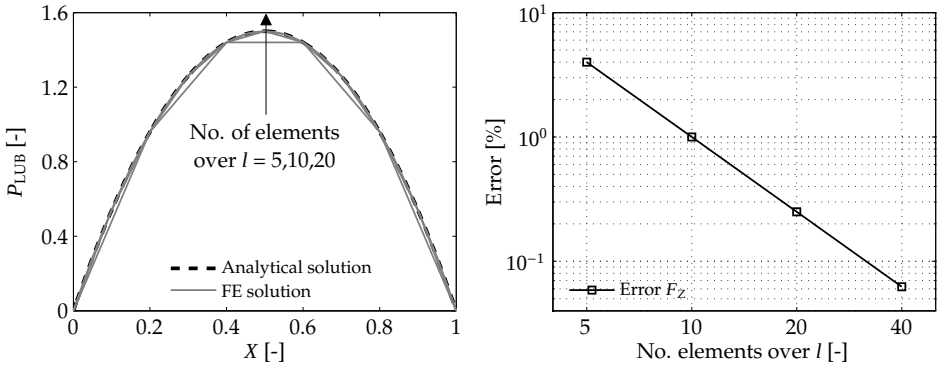

Figure 3.7 *Test case 2.* ***Left:*** *Pressure distribution for different mesh densities.* ***Right:*** *Error between numerical and analytical results.*

shows that the terms describing Couette and Poisseuille flow are solved correctly using the interface elements. An accurate prediction of the normal and shear forces is achieved when using $\geq$ 20 elements over the contact length l (error $< 1\,\%$).

$$\text{Error} = \frac{|F_i - \hat{F}_i|}{F_i} \times 100\,\% \tag{3.31}$$

Parallel-surface squeeze film bearing

The second test case describes a parallel-surface squeeze film bearing, consisting of two parallel plane surfaces separated by an oil film, see Figure 3.6 (left). A

positive pressure within the oil film is generated when the two surfaces are moving towards each other. This squeezing action provides a cushioning effect between the surfaces, introduced by the finite time to squeeze the fluid out of the gap. Negative pressures in the liquid film are introduced when moving the surfaces apart from each other. The numerically predicted pressure distribution p_{lub} can be written in non-dimensional form by [24]:

$$P_{\text{LUB}} = \frac{p_{\text{lub}} \Delta h^3}{\eta v_{z2} l^2} \tag{3.32}$$

The analytical solution for the non-dimensional pressure distribution within the film P_{LUB} is given by Equation (3.33) [24]. The total non-dimensional shear force acting on the bounding surfaces (F_{X1} and F_{X2}) equals zero.

$$P_{\text{LUB}} = 6X(1 - X) \tag{3.33}$$

with $X = x/l$.

The numerically predicted pressure build-up underneath the bounding surfaces is shown in Figure 3.6 (right). A symmetrical pressure distribution underneath the surfaces is predicted. A comparison between the analytical and numerical pressure distribution is shown in Figure 3.7 (left). A mesh-density of 5, 10, 20 and 40 elements over the contact length l and 10 elements over the contact width w has been used to obtain the FE results. The normal force F_{Z} converges quadratically to the analytical solution, as was also observed from the fixed-incline slider bearing, see Figure 3.7 (right). The error drops below 1 % when using a mesh density of ≥ 10 elements over the contact length l, proving a correct implementation of the terms describing squeeze flow.

2D fluid flow

Side leakage of lubricant flow was neglected in the previous test cases, enabling a comparison with the known analytical solution of 1D fluid flow test cases. Side leakage should be accounted for to model 2D fluid flow, which is introduced by prescribing the lubricant pressure to $p_{\text{lub}} = 0$ at $y = 0$ and at $y = w$. The pressure distribution and shear stress distribution for 2D fluid flow are shown in Figure 3.8 and Figure 3.9 for the fixed-incline slider bearing and the parallel-surface squeeze film bearing, respectively.

A lubricant pressure concentration underneath the converging wedge is obtained for the fixed-incline slider bearing, see Figure 3.8 (left). The lubricant pressure p_{lub} equals zero around the boundaries, which matches the prescribed boundary

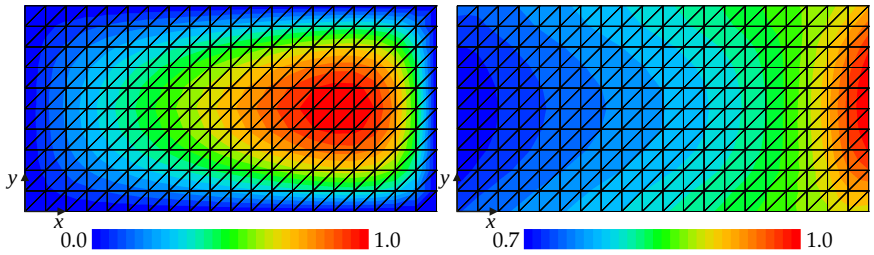

Figure 3.8 *Results fixed-incline slider bearing for 2D fluid flow.* ***Left:*** *Non-dimensional pressure distribution* ***Right:*** *Non-dimensional shear stress distribution.*

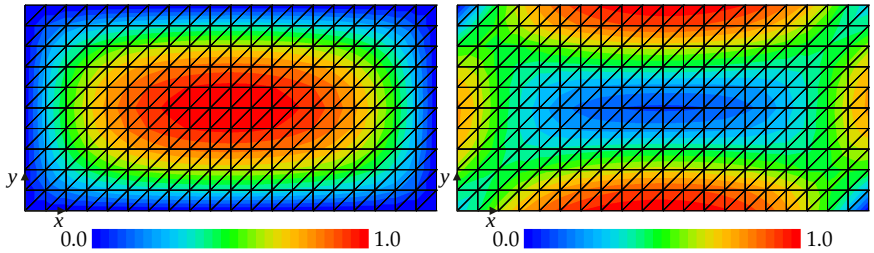

Figure 3.9 *Results parallel-surface squeeze film bearing for 2D fluid flow.* ***Left:*** *Non-dimensional pressure distribution* ***Right:*** *Non-dimensional shear stress distribution.*

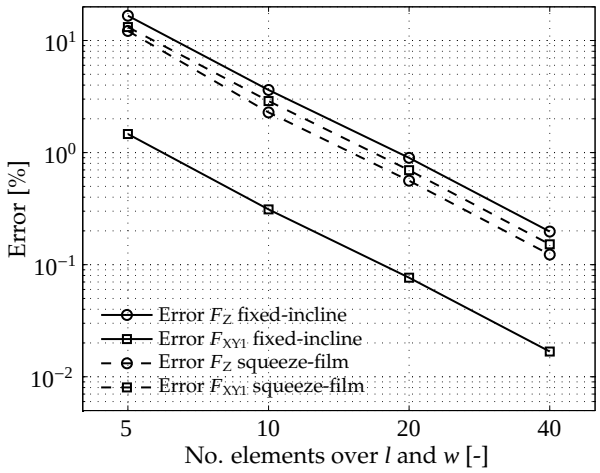

Figure 3.10 *Error in F_Z and F_{XY1} for 2D fixed-incline slider bearing and parallel-surface squeezing film bearing.*

conditions. Figure 3.8 (right) shows the corresponding distribution of shear stresses, acting between the lubricant and the lower bounding surface. The shear stress shown equals the Euclidean norm of the shear stress in both x and y direction at the lower fluid–solid interface. As shown in Equation (3.4), the Euclidean norm depends on the surface velocities and the gradient of the hydrodynamic pressure p_{lub} in both x and y directions.

Figure 3.9 (left) and 3.9 (right) show the pressure distribution and shear stress distribution for the 2D parallel-surface squeeze film bearing. A symmetric pressure distribution is predicted with its maximum centered in the middle. The pressure decreases to the prescribed boundary conditions of $p_{\text{lub}} = 0$ at the edges. The corresponding Euclidean shear stress depends on the gradient of the pressure p_{lub} only, since both in plane surface velocities are zero. Consequently, the shear stress equals zero in the center and obtains its maximum at the edges.

Since a structured mesh is used to solve the 2D test cases, a small influence of mesh orientation can be observed in the predicted results. See, for example, the predicted shear stress at the corners of Figure 3.9 (right). The influence of mesh orientation decreases by using an unstructured mesh.

Simulations have been executed using different mesh-densities to show the convergence behavior of both the total normal force and the shear force. The shear force F_{XY1} has been obtained from the Euclidean shear stress distribution. Values have been compared with FE results obtained using a fine mesh-density of 100×100 elements. Figure 3.10 shows the convergence of error values for both the fixed-incline slider bearing and parallel-surface squeeze film bearing. Identical behavior in error values is observed as was found for the 1D test cases. As can be seen, the error in normal and shear forces drops below 1 % for both 2D test cases when using a mesh-density of $\geq 20 \times 20$ elements.

3.5.2 Modeling thin film lubricant flow

The *averaged* Reynolds equation is implemented in the interface element, which enables the description of roughness effects on thin film and mixed lubrication fluid flow. The 1D fixed-incline slider bearing has been used to demonstrate the functioning of the discretized averaged Reynolds equation. Parameters of the test case can be found in Table 3.1.

Expressions for the flow factors $\mathbf{\Phi}_{\text{p}}$ and $\mathbf{\Phi}_{\text{s}}$ (Equation (3.5)) are required to solve the averaged Reynolds equation. Flow factors are usually classified by the surface ratio h/S_{q}, in which S_{q} describes the composite RMS surface roughness of the

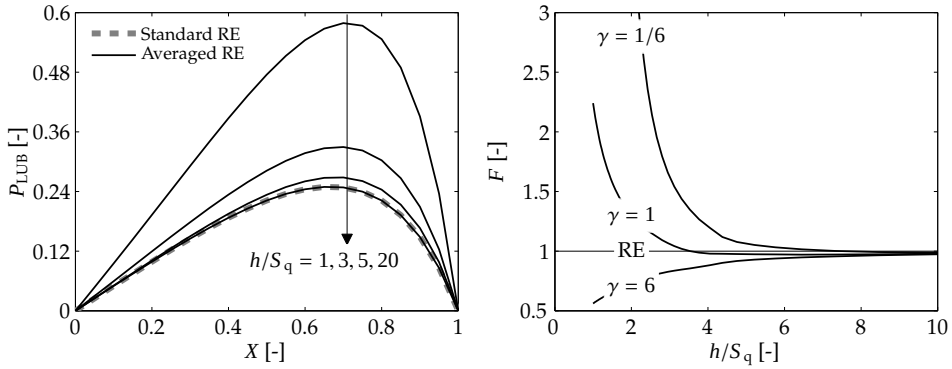

Figure 3.11 *Influence roughness on fluid flow for the fixed incline slider bearing.* ***Left:*** *Influence on pressure distribution.* ***Right:*** *Influence on load-carrying capacity.*

lower and the upper surface:

$$S_q = \sqrt{S_{q1}^2 + S_{q2}^2} \tag{3.34}$$

The flow factor expressions proposed by Patir & Cheng [50] and Wilson & Marsault [87] are used to illustrate thin film lubricant flow. Patir & Cheng proposed flow factors applicable for surface ratios of $h/S_q > 3$, describing lubricant flow from the thin film lubrication regime till the thick film lubrication regime. Wilson & Marsault derived flow factor expressions for surface ratios of $h/S_q < 3$, which can be used to describe lubricant flow in the mixed lubrication regime. Flow factors for 1D fluid flow are provided in Appendix A. The flow factors account for the geometrical orientation of asperities by using a Peklenik surface pattern parameter γ [51]. γ has a value of 1 for isotropic surface patterns, $\gamma < 1$ for transversely oriented asperities and $\gamma > 1$ for longitudinally oriented asperities (with respect to the direction of sliding). The value of γ describes the correlation length of the asperities, $\gamma = \infty$ for 1D longitudinal and $\gamma = 0$ for 1D transversal oriented asperities. The asperity orientation will have an influence on the channeling and/or blocking effect on lubricant flow, and will increase for a decreasing h/S_q ratio. An extensive study on the influence of the roughness orientation γ, the S_q value of the tool and workpiece surface and the height of the fluid film separation h on the load-carrying capacity of the lubricant can be found in [50].

The lubricant pressure distribution for different surface ratios is shown in Figure 3.11 (left). As can be seen, the lubricant pressure increases for a decreasing

h/S_q value. The pressure increase is introduced by the load-carrying capacity of fluid entrapped into rough surface valleys and by the increased flow transport due to sliding of rough surfaces. For high surface separations $h/S_q > 10$ the averaged form of the Reynolds equation degenerates to the standard form of the Reynolds equation.

Figure 3.11 (right) shows the load-carrying capacity F of the lubricant for different surface orientations, indicated by γ. The non-dimensional load-carrying capacity F is normalized to the load-carrying capacity obtained from the standard Reynolds equation. Results are shown for $\gamma = 6$, representing longitudinal oriented asperities and $\gamma = 1/6$ for transversal oriented asperities. A longitudinal lay facilitates the flow, resulting in a lower load-carrying capacity compared to isotropic oriented asperities. On the other hand, a transverse lay restricts the fluid flow which results in a higher load-carrying capacity, see Figure 3.11 (right). For high surface separations, the load-carrying capacity reduces to the load-carrying capacity calculated by the standard form of the Reynolds equation. The observed trends satisfy expectations and correspond with trends found by Patir & Cheng in [50], demonstrating a correct functioning of the interface element.

3.5.3 Modeling mixed lubrication and generating Stribeck curves

The fluid film thickness is related to the amount of asperity deformation in the mixed lubrication regime (Section 3.3). Lubricant flow can be introduced by the Poiseuille effect and/or Couette flow due to variations in nominal contact pressure and bulk strain within the contact zone.

A linear increasing nominal contact pressure is applied to the upper surface of the test case, see Figure 3.12. It is assumed that the upper surface represents the rigid tool surface and the lower surface the deformable workpiece surface. Depending on the process settings used (velocity, viscosity, geometry), the nominal contact pressure is either carried by contacting surface asperities, the lubricant, or by a combination of both. Figure 3.12 shows the deformation of surface asperities at two locations. An increasing amount of asperity deformation is observed along the contact length l, since a linear increasing load is applied to the upper surface. Consequently, calculated from the amount of asperity deformation (Equation (3.9)), a decrease in fluid film thickness is found, see Figure 3.13 (left). The decrease in fluid film thickness generates a physical converging wedge between the 2 contacting surfaces. The wedge generates a pressure build-up within the lubricant if a velocity of v_{x1} is applied to the lower surface, as was also observed from the fixed-incline slider bearing examples. A velocity range

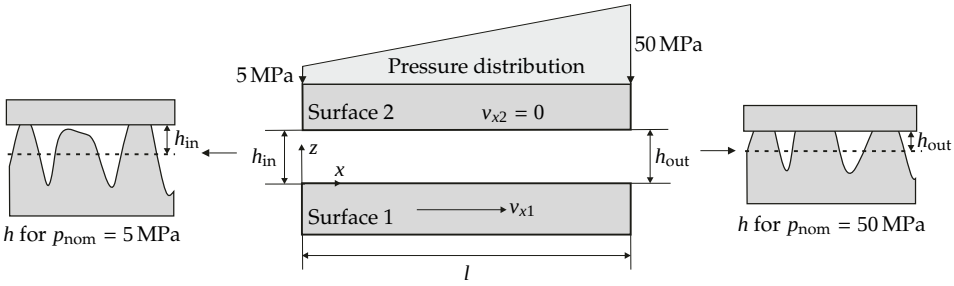

Figure 3.12 *Schematic view mixed lubrication regime test case.*

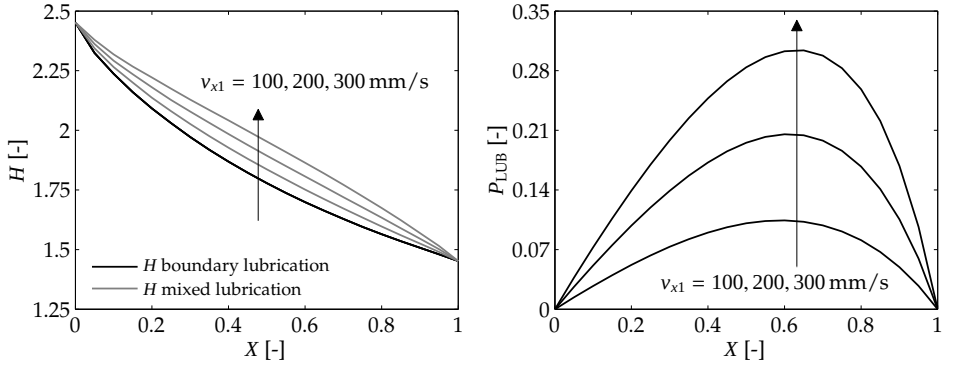

Figure 3.13 *Results mixed lubrication test case using different sliding velocities.* ***Left:*** *Fluid film thickness.* ***Right:*** *Pressure distribution.*

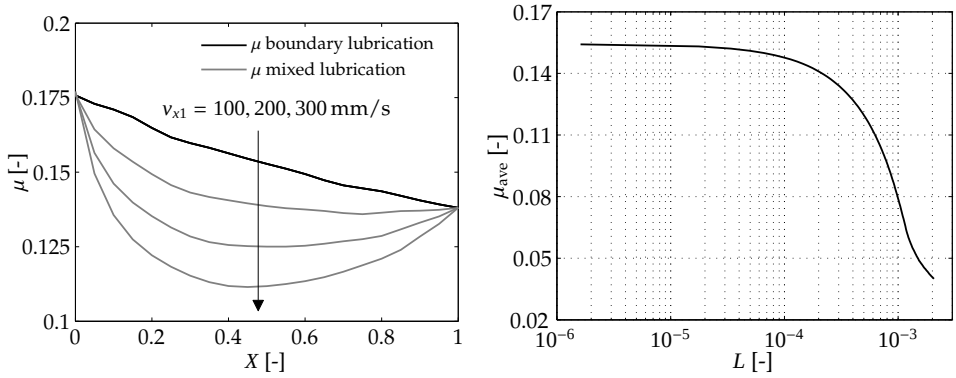

Figure 3.14 *Results mixed lubrication test case using different sliding velocities.* ***Left:*** *Friction coefficient.* ***Right:*** *Stribeck curve.*

of v_{x1} = 100-300 mm/s and a linear increasing pressure from 5-50 MPa has been prescribed to perform the mixed-lubrication analysis. Parameters not indicated in Figure 3.12 are given in Table 3.1.

The development of the fluid film thickness, lubricant pressure and friction coefficient along the contact length is shown in Figure 3.13 and Figure 3.14, respectively (see Equation (3.26) and Equation (3.30) for the dimensionless parameters used). As can be seen, increasing the sliding velocity generates a higher pressure build-up within the lubricant. The lubricant pressure supports the load-carrying capacity of the lubricant, meaning that less load is carried by contacting surface asperities. Consequently, higher lubricant pressures decrease the shear stress between contacting surfaces, represented by lower values for the friction coefficient, see Figure 3.14 (left). The hydrodynamic pressure build-up also influences the fluid film thickness. A higher load-carrying capacity of the lubricant yields less deformation of the contacting surface asperities, leading to a higher fluid film thickness (Figure 3.13 (left)).

Generation of Stribeck curves

Figure 3.13 (right) clearly shows the influence of the sliding velocity on the load-carrying capacity of the lubricant. For a certain velocity, the load-carrying capacity of the lubricant will be high enough to carry the total applied load, representing thin film lubrication. Decreasing the velocity decreases the load-carrying capacity of the lubricant, until the total load is carried by interacting surface asperities, representing boundary lubrication. The characteristic curve describing the transition from boundary lubrication to mixed lubrication and from mixed lubrication to thin film lubrication is often referred to as the Stribeck curve [68].

The Stribeck curve plots the mean value of the friction coefficient μ_{ave} as a function of one or more operational parameters. In this work, the dimensionless lubrication number L, introduced by Schipper in [62], has been used. L is a function of the viscosity η, sum velocity v, mean pressure $\bar{p}$ and the surface roughness S_{a}, see Equation (3.35). The latter parameter is liable to changes since the amount of asperity deformation, and therefore the surface roughness, depends on the pressure build-up p_{lub} in the lubricant. μ_{ave} represents the average friction coefficient over the contact length l, see Figure 3.14 (left).

$$L = \frac{\eta v}{\bar{p} S_{\text{a}}} \tag{3.35}$$

Figure 3.14 (right) shows a generated Stribeck curve obtained from the mixed lubrication test case. A velocity range of v_{x1} = 1-1500 mm/s has been used to obtain the corresponding friction coefficients. A clear transition from boundary to mixed lubrication and the start of the transition from mixed to thin film lubrication is visible. Contact between the surfaces is required to solve the mixed lubrication friction model, which follows from the definition of the fluid film thickness h (see Section 3.3). Hence, friction in the thin film or thick film lubrication regime cannot be described by the current approach. The shape of the calculated Stribeck curve corresponds to the characteristic S-shape known from Stribeck curves. Credible friction coefficients in between 0.15 and 0.04 are found from the boundary lubrication regime till the thin film lubrication regime.

Influence of process conditions on transition points

Changing the process conditions (nominal contact pressure, viscosity and size of the lubrication zone) will influence the hydrodynamic pressure build-up in the lubricant. From practice, it is known that transition points shift to lower L values for increasing the mean pressure $\overline{p}$, see for example [15, 63]. Stribeck curves for different nominal contact pressures and contact lengths have been generated to represent this change in transition points. Generated Stribeck curves are shown in Figure 3.15, and discussed next.

Influence of pressure on transition points

Figure 3.15 (left) shows generated Stribeck curves for an increasing nominal contact pressure p_{nom} along the contact length l. The nominal contact pressure at the outlet of the fluid inclusion has been varied such that Δp_{nom} ranges from 1 MPa to 40 MPa. The expression of Δp_{nom} and of the mean pressure $\overline{p}$ is given in Equation (3.36). A higher Δp_{nom} value results in an increasing amount of asperity deformation along the contact length, leading to an increase in the converging wedge between the 2 surfaces. Increasing the physical wedge between surfaces results in an increase in the load-carrying capacity of the lubricant, leading to a decreasing value of the friction coefficient. Consequently, a shift in transition points to a lower lubrication number L can be observed for an increasing value of Δp_{nom}. In addition, lower friction coefficients are found within the boundary lubrication regime when increasing the nominal contact pressure p_{nom}. The decrease in friction coefficients is explained in Section 2.5.

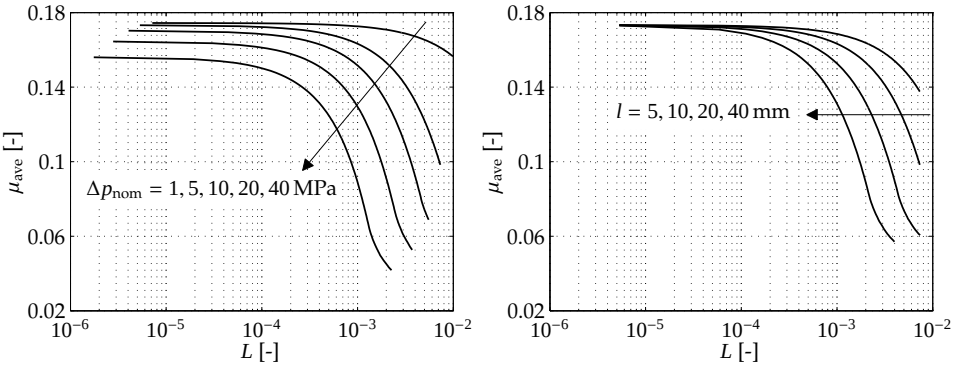

Figure 3.15 *Generation of Stribeck curves.* ***Left:*** *Influence of pressure on transition points.* ***Right:*** *Influence of contact length on transition points.*

$$\Delta p_{nom} = p_{nom}(x = l) - p_{nom}(x = 0)$$
$$\bar{p} = \frac{1}{2}\left(p_{nom}(x = 0) + p_{nom}(x = l)\right) \tag{3.36}$$

Influence of contact length on transition points

Increasing the contact length l of the lubrication zone, while keeping the mean pressure $\bar{p}$ equal, increases the load-carrying capacity of the lubricant. The trend in asperity deformation, and therefore the shape of the Stribeck curve, is not affected by changing the length of the contact zone. Due to the increased load-carrying capacity of the lubricant a horizontal shift in transition points from boundary to mixed and from mixed to thin film lubrication is introduced, as can be seen in Figure 3.15 (right).

Changing the nominal contact pressure p_{nom} or the contact length l results in a change of the Stribeck transition points, which corresponds to experimentally obtained results [15, 63]. The size of the contact zone, nominal contact pressure and strain within the blank material changes during forming processes, changing the location of transition points in time. The results show that boundary lubrication, mixed lubrication and the transition from boundary to mixed lubrication can be accounted for by the mixed lubrication friction model. A credible distribution in friction coefficients is found, demonstrating the potential of the advanced friction model in FE forming simulations.

Closure

A mixed lubrication friction model is proposed in this chapter. A coupling between a hydrodynamic friction model and the boundary lubrication friction model, as described in Chapter 2, has been made for this purpose. An interface element has been developed to solve the hydrodynamic part of the friction model, which has been implemented in an existing FE software code.

Application of the interface element to 1D fluid flow test cases showed a correct FE discretization of the mixed lubrication friction model. Application to 2D fluid flow test cases illustrated the capabilities of the element to describe more realistic fluid film problems. It was shown that a mesh-density of $\geq 20 \times 20$ elements within the contact zone is already able to describe fluid film situations with an error of less than 1 %.

The potential of the mixed lubrication friction model has been illustrated by the generation of Stribeck curves under different process conditions. The change in transition points from boundary to mixed lubrication and from mixed to thin film lubrication can be predicted. The range of friction coefficients is in the order of what to expect from practice.

Chapter 4

Determination of model parameters

The accuracy of the mixed lubrication friction model depends on a proper description of input parameters. An experimental procedure is presented in this chapter to obtain these parameters. First, a method is presented in Section 4.2 to measure representative 3D rough surface textures. Next, the formation and shear strength of boundary layers is discussed in Section 4.3. Finally, input parameters of the micro-mechanical friction mechanisms discussed in Chapter 2 are obtained by calibrating model results to experimental results. The real contact area is used in Section 4.4 and Section 4.5 to quantify parameters introduced by the asperity deformation models. In Section 4.6, results of friction experiments are used to obtain parameters of the ploughing model and to demonstrate the predictive capabilities of the mixed lubrication friction model.

4.1 Introduction

Over recent years, different experimental studies have been performed to describe the tribological behavior between forming steels and tool steels under dry and lubricated conditions [15, 62, 66, 71]. Emmens [15] stated that care must be taken in comparing results obtained from different friction testers, since there are fundamental differences between friction tests on concentrated contacts and tests on flat contacts. He also showed that changing the dimensions of the flat contact spots (under the same process conditions) can lead to different results. Sniekers [66] stated that extrapolation of experimental data from one situation to another can lead to erroneous results. Therefore, experiments have to be carried out under similar process conditions as used in the actual forming process. That is, the experimental workpiece/tool roughness characteristics, lubrication properties, sliding velocities, nominal contact pressures and strains in the material should match process conditions present during the forming process of interest.

In Chapter 5 the performance of the mixed lubrication friction model is demonstrated by two deep-drawing applications. For this reason, the same metal–lubricant combination and comparable process conditions have been used for the friction experiments discussed in this chapter.

4.2 Surface parameters

The mixed lubrication friction model requires both a deterministic description and a stochastic description of the tool and the workpiece surface. A method to obtain 3D surface scans is presented in Section 4.2.1. The determination of stochastic surface parameters is discussed in Section 4.2.2.

4.2.1 Deterministic surface description

3D surface scans are obtained by confocal microscopy measurements. Figure 4.1 (left) shows a surface measurement onto electro discharged textured (EDT) sheet material. Figure 4.1 (right) shows a surface measurement onto a ground tool surface. Measured surface textures must be corrected on two aspects before they can be used for a friction analysis. First, errors are introduced during the measurement represented by sharp peaks, called spikes. A noise filter is required to remove these spikes from the measurement data. A filter often used in the field of image and signal processing is the median filter, a non-linear digital

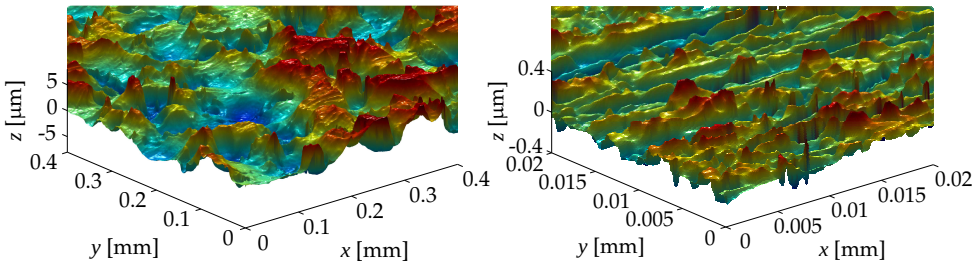

Figure 4.1 *3D surface impression measured by confocal microscopy.* ***Left:*** *Workpiece surface.* ***Right:*** *Tool surface.*

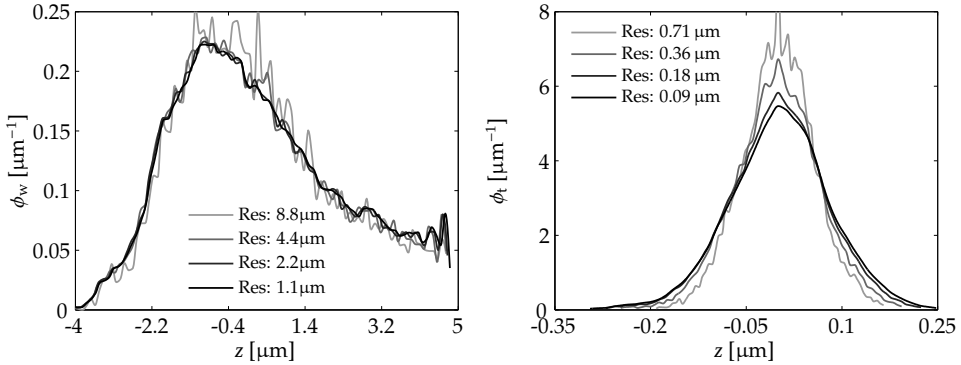

Figure 4.2 *Height distributions for different pixel sizes.* ***Left:*** *Workpiece surface.* ***Right:*** *Tool surface.*

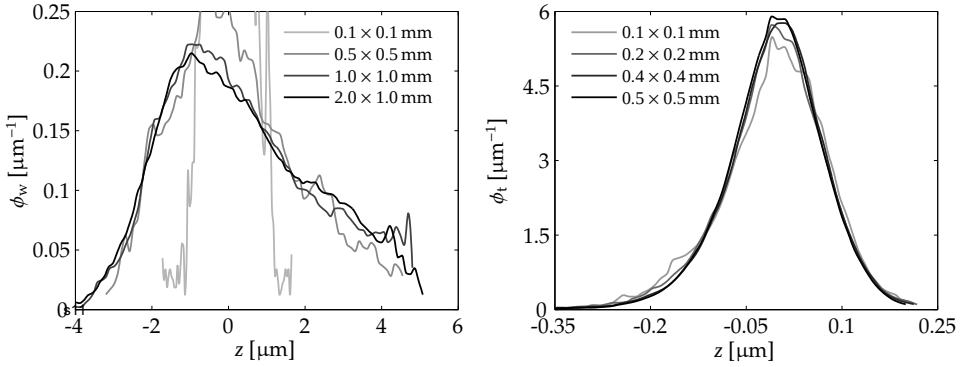

Figure 4.3 *Height distributions for different measurement areas.* ***Left:*** *Workpiece surface.* ***Right:*** *Tool surface.*

filtering technique [36]. A kernel size of 3 is used in this research, meaning that a matrix of 3×3 points is used to determine the median of each point. Secondly, a tilt or curvature might be present in the measured surface texture due to the geometry of the specimen, or due to misalignments of the specimen during the measurements. The surface measurement should be corrected for these two aspects since perfectly aligned surfaces are required to perform a friction analysis. For this purpose, a 2^{nd} order polynomial function is fitted through the measurement data. The measurement data is shifted, tilted and straightened to its origin by subtracting the polynomial function from the measurement data. Corrected surfaces of both the workpiece and the tool material are shown in Figure 4.1.

Moreover, a representative surface scan of both the tool material and the workpiece material is required. Representative means that a resolution is used which is fine enough, while the size of the measurement area is large enough, to capture the most important details of the surface. The representativeness of a surface measurement is related to the surface height distribution in this section. That is, given a finer resolution and a larger measurement area the shape of a surface height distribution will converge. For computational purposes, the measurement size and pixel size is used for which the shape of the surface height distribution is close to the converged shape. The validity of this approach will be demonstrated in Section 4.7 by performing friction analyses on different measured surface textures.

Figure 4.2 (left) shows surface height distributions of the workpiece surface for 4 different pixel sizes, using a measurement area of $1 \times 1\,\text{mm}$. It is observed that the difference in surface height distributions is small for pixel sizes less than $2.2\,\mu\text{m}$. Hence, a pixel size of $2.2\,\mu\text{m}$ is used in this thesis. Figure 4.3 (left) show surface height distributions for 4 different area sizes. It is concluded that a measurement area of $1 \times 1\,\text{mm}$ captures enough detail to ensure a representative surface scan of the workpiece. The same analysis has been performed on the tool surface, see Figure 4.2 (left) and Figure 4.3 (right) for the pixel size comparison and measurement area size comparison, respectively. A maximum pixel size of $0.18\,\mu\text{m}$ and a minimum measurement area of $0.4 \times 0.4\,\text{mm}$ ensures a representative surface scan of the tool surface. However, due to computer resources, a pixel size of $0.36\,\mu\text{m}$ and an area of $0.4 \times 0.4\,\text{mm}$ is used in this research. The difference in measurement area and scanning resolution between the tool surface and workpiece surface is caused by the difference in roughness values. Hence, the relatively smooth tool surface ($S_q = 0.06\,\mu\text{m}$) allows a smaller measurement area and requires a finer scanning resolution than the rougher workpiece surface ($S_q = 1.9\,\mu\text{m}$).

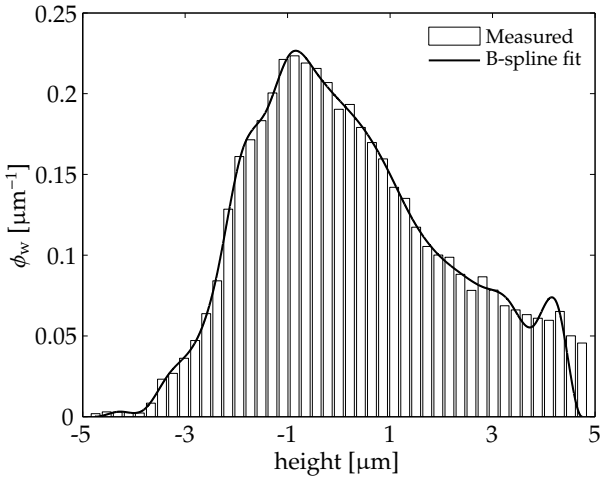

Figure 4.4 *Measured surface height distribution of the workpiece surface approximated by a B-spline function.*

4.2.2 Stochastic surface description

The asperity deformation models discussed in Section 2.3 depend on a stochastic description of the rough workpiece surface. This means that the surface height distribution of the workpiece ϕ_w is used to make an efficient translation from micro-scale contact modeling to macro-scale contact modeling. Moreover, to describe flattening of asperities due to combined normal loading and straining of the underlying bulk material the asperity density ρ_w is required.

The surface height distribution is obtained from 3D rough surface measurements. Various methods exist to describe surface height distributions by continuous functions, which is desirable for efficiency reasons. Often a normal distribution function is used. However, the surface height distribution of the undeformed material is usually asymmetric, requiring a more advanced method to approximate the surface height distribution. By using B-splines [12, 75], asymmetric surface height distributions can be approximated. The accuracy of the approximation depends on the order of the splines and the number of splines used to construct the curve. A surface height distribution of the workpiece surface is shown in Figure 4.4, for which 15 cubic splines have been used to describe the B-spline function. An accurate representation of the surface height distribution can be made, noting that the error can be reduced further by using more splines. The B-spline function is used in this work to approximate surface height distributions.

The second stochastic parameter is described by the asperity density ρ_w. The location of asperities can be obtained by using a 3-point summit rule (for 2D line profiles) or using a nine-point summit rule (for 3D surfaces) [13]. A summit refers to the tip of an asperity, and is defined as a surface point which is higher than its neighboring points. If the location and number of summits is known, the asperity density can be obtained.

4.3 Boundary layer shear strength

The ploughing model presented in Chapter 2 requires a relation to describe the adhesive forces between ploughing asperities. These forces are described by the shear strength of interfacial boundary layers, as outlined in Section 4.3.1. Adhesive forces will dominate the ploughing forces in the case of smooth and clean contacting surfaces. Sliding experiments have therefore been conducted using polished surfaces. The process specifications of the experimental procedure is presented in Section 4.3.2. Experimental results are discussed in Section 4.3.3, in which a relation to describe the boundary layer shear strength is proposed.

4.3.1 Formation of boundary layers

Although solid–solid contact occurs between two sliding surfaces in the boundary lubrication regime, a boundary film is still present between the surfaces. This boundary layer is formed by physical absorption, chemical absorption or chemical reaction [19] of the lubricant with the surfaces. The formation of boundary layers was first postulated by Lord Rayleigh [54] and Hardy and Doubleday [25]. The layer prevents direct contact between the solids which reduces the coefficient of friction significantly.

Different empirical models exist to calculate the shear strength of boundary layers. Timsit & Pellow [74] and Briscoe & Evans [7] performed experiments on glass, gold and aluminum with stearic acid types of lubricants. The derived models are based on a measured shear strength as a function of the mean Hertzian contact pressure. A review on the influence of pressure, temperature, speed and the thickness of the boundary layer on the shear strength for different lubricant–base material combinations can be found in [81]. It was stated here that an increase in pressure causes an increase in shear strength while an increase in temperature lowers the shear strength. The author also mentioned that the influence of sliding speed on the shear strength largely depends on the type of lubricant used.

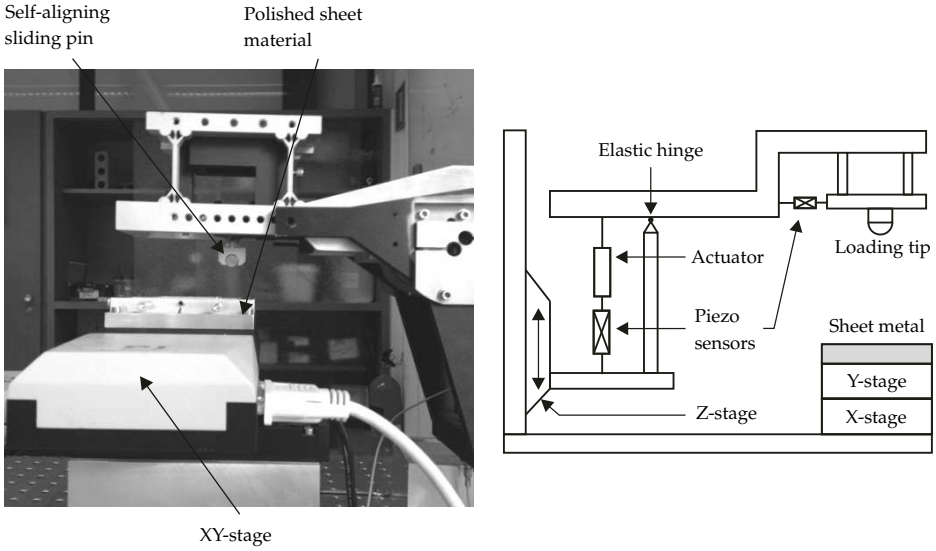

Figure 4.5 ***Left:*** *Sliding friction tester.* ***Right:*** *Schematic view of friction tester.*

Table 4.1 *Process specifications linear friction tester.*

Parameter	Specification
Blank material	DC06 EN10130:2006
Tool material	DIN 100Cr6
Lubricant	Quaker FERROCOAT® N6130
Lubrication amount	0.6 g/m^2 and 2.0 g/m^2
Pin radius	5 mm
Length pin	10 mm
Speed	1 mm/s
Pressure	20-110 MPa
Sliding distance	20 mm

The empirical models readily available in the literature do not, however, apply for the metal–lubricant combination discussed in this thesis. Hence, the aim of this section is to derive an empirical relation for the metal–lubricant combination of interest, see Table 4.1.

4.3.2 Linear friction tester

A linear sliding friction tester has been used to study the dependence of nominal contact pressure and lubrication amount on the shear strength, see Figure 4.5 (left). The frictional force was measured during sliding of a cylindrical pin over sheet material under a prescribed normal load. The cylindrical pin is made of ball bearing steel (100Cr6 steel), which has similar mechanical properties as tool steels used in metal forming. Experiments have been executed at room temperature. The process specifications are listed in Table 4.1.

The friction tester has an X-Y linear positioning stage separately driven by actuators. The loading tip is supported by a horizontal beam, which can be positioned in z direction by a linear actuator (coarse displacement) and a piezo actuator (fine displacement). The normal force is applied by a force controlled piezo actuator in z direction. The friction force is measured by a piezo sensor as schematically shown in Figure 4.5 (right). The normal force and friction force can be measured and controlled within a range of 0.1-50 N. The sliding pin is self-aligning, which ensures complete contact with the sheet material during sliding.

Polishing of the relatively rough sheet material (S_q = 1.9 μm) is required to maximize the real contact area over the width of the sliding pin. This ensures that the measured friction force is mainly caused by the shear between boundary layers, avoiding ploughing effects as much as possible. Polishing is done by using a rotating disc polisher using Kemet liquid diamond solution of type 25 μm, 6 μm and 3 μm.

4.3.3 Describing the boundary layer shear strength

Figure 4.6 shows 3D measured surface textures of the sliding pin and the polished sheet material before sliding. Surfaces after sliding with a nominal contact pressure of 20 MPa and 50 MPa are shown in Figure 4.7. The surfaces have been measured by white light inteference microscopy, and post-processed as discussed in Section 4.2. Different workpiece samples have been used for surface measurements, meaning that surface profiles shown are measured at different locations.

From the surface measurements on slided test samples (Figure 4.7) some light scratches can be observed. These scratches are caused by a few higher asperities of the slider pin. Hardly any material transfer was observed during the tests and no asperity flattening can be observed from the surface height distributions, see Figure 4.8. From the relatively small amount of material deformation during

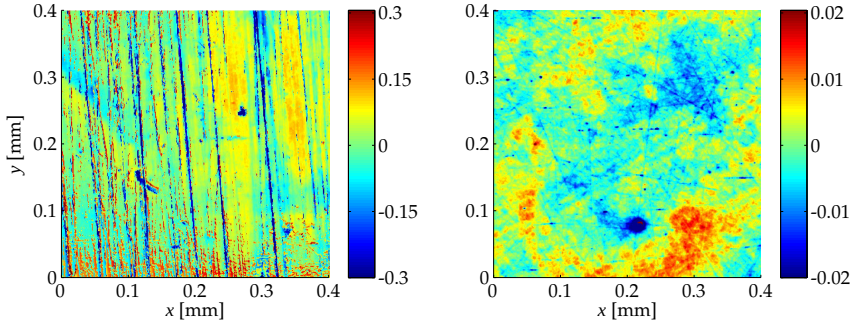

Figure 4.6 *Measured surface height textures (in µm).* ***Left:*** *Sliding pin (S_q = 0.12 µm).* ***Right:*** *Polished workpiece surface (S_q = 0.006 µm).*

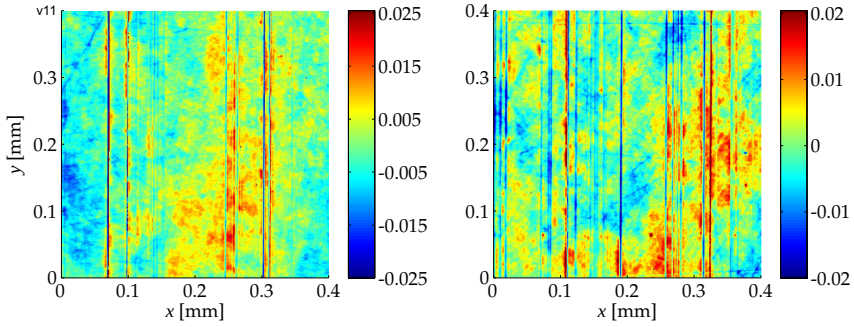

Figure 4.7 *Measured surface height textures of polished workpiece surface after sliding (in µm).* ***Left:*** p_{nom} = 20 *MPa*, S_q = 0.006 µm. ***Right:*** p_{nom} = 50 *MPa*, S_q = 0.006 µm.

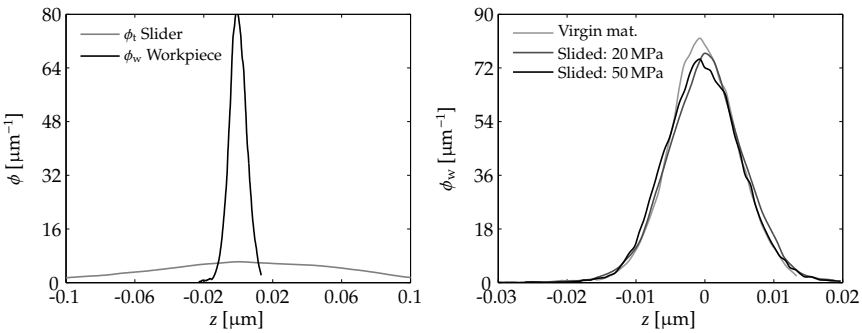

Figure 4.8 *Measured surface height distributions.* ***Left:*** *Slider and undeformed polished workpiece.* ***Right:*** *Undeformed and deformed polished workpiece.*

sliding, it is assumed that the measured friction forces are mainly induced by the shear stresses acting in the boundary layers.

A repeatability study has been performed using a nominal contact pressure of 20 MPa. The coefficient of friction is measured for subsequent sliding tracks, results are shown in Figure 4.9 (top). No significant difference is found for the first 4 traverses. An increase in friction coefficient can be observed after the 4^{th} traverse, indicating that the boundary layer is partially destroyed due to sliding.

In sheet metal forming, the lubrication amount is normally controlled within a range of 0.6-2.0 $\mathrm{g/m^2}$. These two amounts are used within 0.1 $\mathrm{g/m^2}$ accuracy to study its influence on the boundary layer shear strength. It is expected that a higher amount of lubricant does not have a significant influence on the boundary layer shear strength, since the experiments are executed in the boundary lubrication regime. Experiments have been conducted using a range of nominal contact pressures of 20 till 110 MPa, and a constant sliding velocity of 1 mm/s (see Table 4.1). The friction force F_{w} is measured over a sliding distance of 20 mm. The contact area A is obtained by adopting the Hertzian theory for line contacts between a cylindrical surface and a flat surface. The shear strength $\tau = F_{\mathrm{w}}/A$ is calculated over a sliding distance of 6 till 20 mm, excluding static friction effects at the start of the sliding measurements. The influence of the lubrication amount and the nominal contact pressure on the boundary shear strength is shown in Figure 4.9 (bottom). The error bar indicates the standard deviation of three different sliding traverses, demonstrating the repeatability of the experiments. The shear strength increases with increasing nominal contact pressure, which was also observed by [7, 74]. It can be seen that the amount of lubrication has no significant influence on the shear strength in between a pressure range of 20-70 MPa. From 70-110 MPa the shear strength for the 2.0 $\mathrm{g/m^2}$ experiments starts diverging from the 0.6 $\mathrm{g/m^2}$ experiments. This behavior contradicts the expectations that an increasing lubrication amount does not influence the boundary layer shear strength. In addition, compared to the 0.6 $\mathrm{g/m^2}$ experiments, a different trend in shear strength as a function of nominal contact pressure is observed for the 2.0 $\mathrm{g/m^2}$ experiments. Hence, additional research is recommended to characterize the shear strength for the 2.0 $\mathrm{g/m^2}$ case, when required.

Timsit and Pelow [74] proposed a power-law relation of the form $\tau = C\left(\frac{p_{\mathrm{nom}}}{p_0}\right)^n$ to describe the shear strength for stearic acid on aluminum. The same relation is used in this work with C, τ and p_0 in Pa. Experimental results of the 0.6 $\mathrm{g/m^2}$ case have been used to obtain the power law parameters, resulting in $C = 0.38$ and $n = 0.93$ (see Figure 4.9 (bottom)).

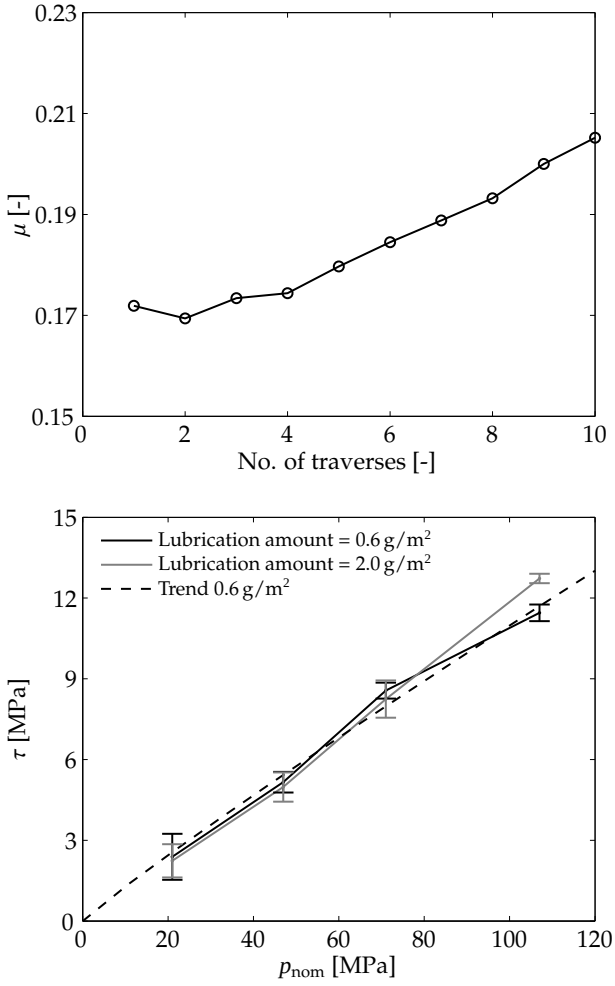

Figure 4.9 ***Top:*** *Development friction coefficient for increasing no. of traverses (p_{nom} = 20 MPa, v = 1 mm/s).* ***Bottom:*** *Development boundary layer shear strength for increasing nominal contact pressures p_{nom}.*

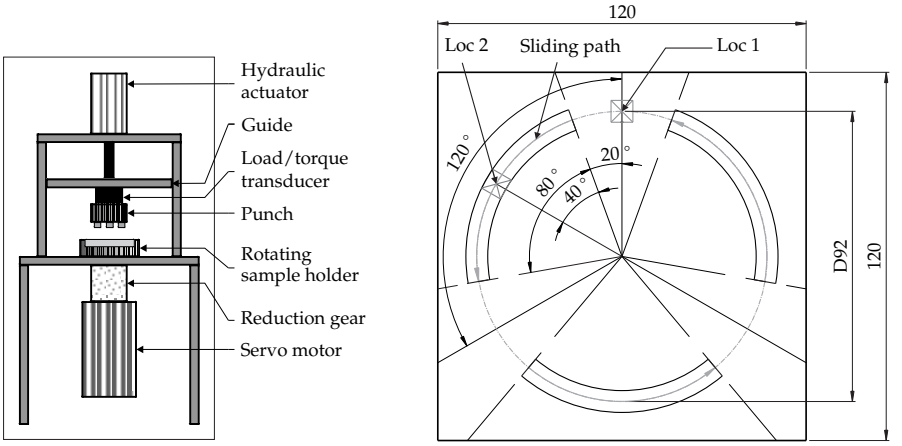

Figure 4.10 ***Left:*** *Rotational friction tester.* ***Right:*** *Workpiece sample for loading/sliding experiments.*

4.4 Input parameters load-dependent deformation models

Three parameters have been introduced in the asperity deformation models discussed in Section 2.3. These parameters have been quantified by calibrating model results to results obtained by normal loading only and normal loading + sliding experiments. The Rotational Friction Tester (RFT) has been used for this purpose. First, the experimental procedure is outlined in Section 4.4.1. Next, results obtained by RFT experiments are reviewed in Section 4.4.2-4.4.4. Finally, the model parameters are determined in Section 4.4.5 based on experimental results.

4.4.1 Rotational friction tester

The amount of asperity deformation, and consequently the real contact area, depends on the nominal contact pressure. The RFT experiment [15], developed at Tata Steel, has been used to investigate this dependency.

The RFT consists of a stationary punch and a rotating workpiece holder, see Figure 4.10 (left). The workpiece holder is driven by a computer controlled brushless servo drive with a low inertia reduction gear. The punch consists of 3 small notches having a flat polished contact area, aligned in one plane and

Table 4.2 *Process specifications RFT.*

Parameter	Specification
Blank material	DC06 EN10130:2006
Tool material	DIN 1.2379
Lubricant	Quaker FERROCOAT® N6130
Lubrication amount	$0.6\,g/m^2$
Notch size	$8 \times 8\,mm$
Punch center-notch radius	46 mm
Workpiece size	$120 \times 120\,mm$
Speed	$10\,mm/s$
Pressure	10,20,30,45,60 MPa
Sliding angle	80° / 120°

positioned at the same radius from the center of the punch. The tool is pressed on the workpiece by a hydraulic actuator. The applied load to the workpiece and induced torque due to sliding are measured by a load/torque transducer. The feasible pressure range applied to the notches depends on the nominal contact area of these notches. By using a tooling with larger or smaller notch areas, the feasible pressure range can be decreased or increased, respectively. The tool is rotated over a user defined rotation angle after applying the load. The conditions of the tests are listed in Table 4.2.

4.4.2 Asperity deformation due to normal loading

For the normal loading only case, the tool was pressed on the workpiece till a specific pressure was reached. To investigate the development in real contact area, pre-defined locations on the workpiece have been scanned by 3D confocal microscopy before and after the loading experiments. Figure 4.10 (right) shows an example of the workpiece and the location of confocal measurements, indicated by 'Loc 1'. Measurements are performed on the same location within an accuracy of 1 μm.

Figure 4.11 presents 3D surface textures obtained from the undeformed surface (top) and deformed surface (bottom). The deformed surface is obtained by loading the undeformed surface by a constant pressure of 60 MPa. The same asperities before and after loading can be easily traced back from the figures. It can be observed that the higher asperities are deformed by the applied load and that a negative of the tool asperities can be found back on top of the deformed

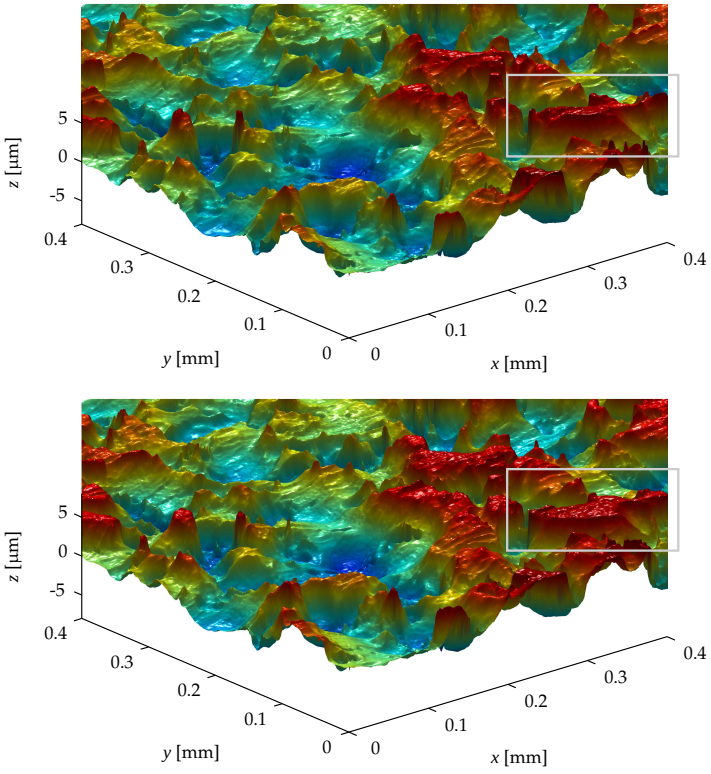

Figure 4.11 *3D measured surface textures of the workpiece surface.* ***Top:*** *Before loading.* ***Bottom:*** *After loading with 60 MPa.*

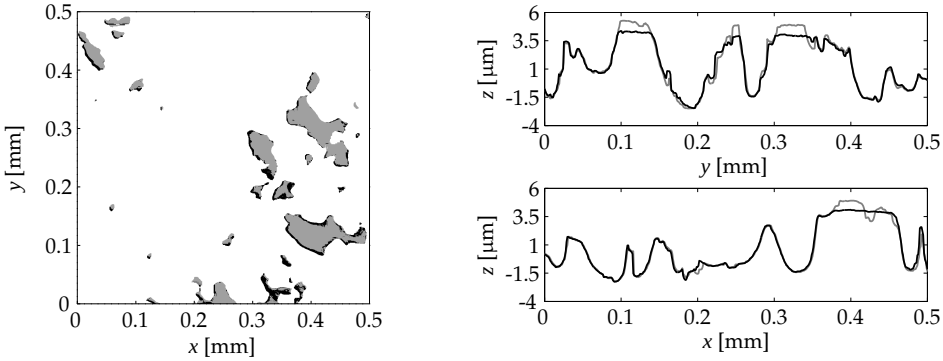

Figure 4.12 ***Left:*** *Top view undeformed (gray) and deformed (black) surface.* ***Right:*** *Cross-section undeformed (gray) and deformed (black) surfaces at $x = 0.39$ mm (top) and $y = 0.31$ mm (bottom).*

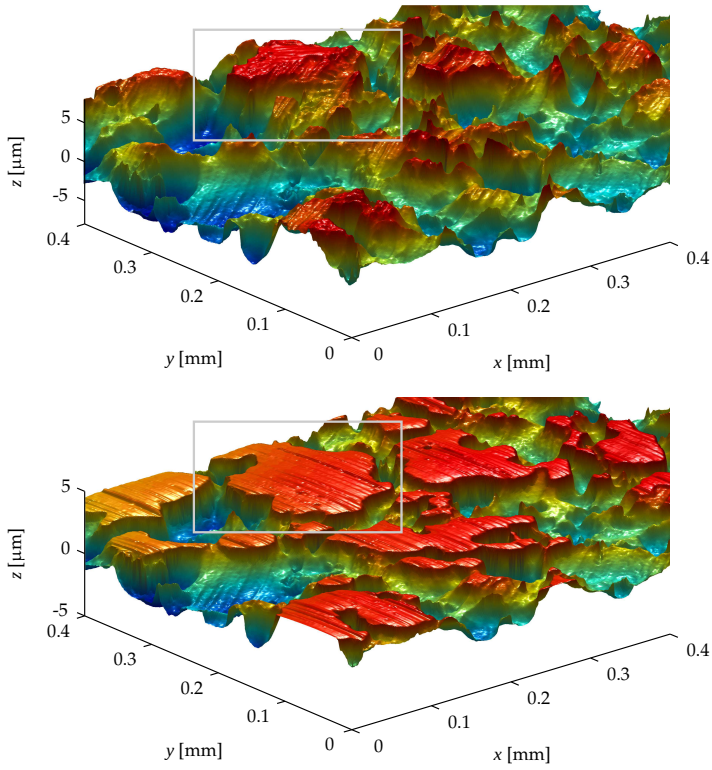

Figure 4.13 *3D measured surface textures of the workpiece surface.* ***Top:*** *Before sliding.* ***Bottom:*** *After sliding with 60 MPa.*

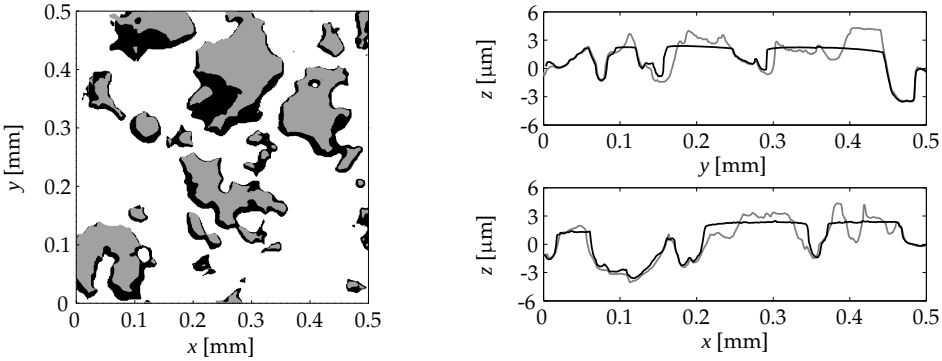

Figure 4.14 ***Left:*** *Top view undeformed (gray) and deformed (black) surface.* ***Right:*** *Cross-section undeformed (gray) and deformed (black) surface at* $x = 0.23\,mm$ *(top) and* $y = 0.38\,mm$ *(bottom).*

workpiece peaks, see for example the highlighted section in Figure 4.11. A top view of both the deformed and undeformed surface is shown in Figure 4.12 (left). This figure shows the projection of the undeformed surface asperities (gray) on the flattened plateaus of the deformed surface asperities (black). By doing so, the black areas visualize the deformation of surface asperities in x and y direction. Figure 4.12 (right) shows cross sections in x and y direction of the undeformed and deformed surface. The undeformed surface is indicated by gray lines, the deformed surface is indicated by black lines. Contact spots are indicated by locations where asperities have been flattened. It can be observed from both the top-view figure and the cross-section figure that the deformation of surface asperities is more or less equal in x and y direction. Surface points close to the crushed asperities experience an upward movement, see Figure 4.12 (right) at 0.4 mm (lower figure). No influence in surface heights is observed for surface points further away from the crushed asperities.

4.4.3 Asperity deformation due to normal loading + sliding

In the case of normal loading + sliding, the tool was rotated 20° with respect to the normal loading position ('Loc 1'), and subsequently loaded and slided over a sliding angle of 80°. 'Loc 2' in Figure 4.10 (right) indicates the position where confocal measurements have been performed.

Figure 4.13 presents 3D measured surface textures showing sliding-induced asperity deformation. The lower surface experienced sliding under a load of 60 MPa in the negative y direction. A significantly higher amount of asperity deformation is observed in comparison with the normal loading only case. Shallow ploughing tracks of the tool asperities are clearly visible, e.g. the highlighted section in Figure 4.13. A top view and cross sections of both the deformed and undeformed surface are shown in Figure 4.14. The undeformed surface is indicated by gray lines/surfaces, the deformed surface is indicated by black lines/surfaces. It can be observed from both figures that asperities are smeared out in sliding direction (negative y direction).

4.4.4 Real contact area

Figure 4.15 shows the initial surface height distributions (dashed lines) and the surface height distributions of the deformed surfaces (solid lines) for 3 different normal loading pressures. The left figures correspond to the normal loading only case, the right figures correspond to the normal loading + sliding case. For all cases, a peak is visible at the location where asperities have been flattened by the

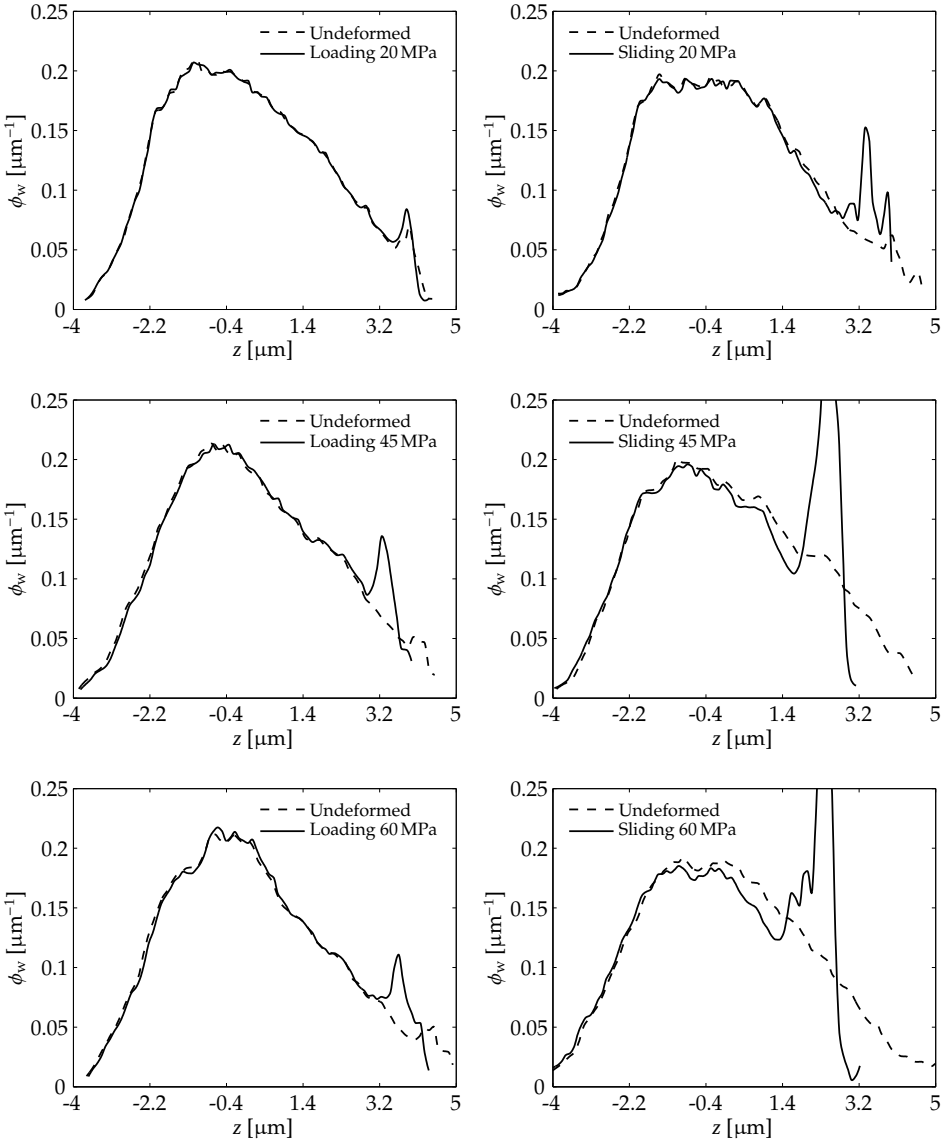

Figure 4.15 *Undeformed and deformed surface height distributions for different normal loading pressures.* ***Left:*** *Normal loading only.* ***Right:*** *Normal loading + sliding.*

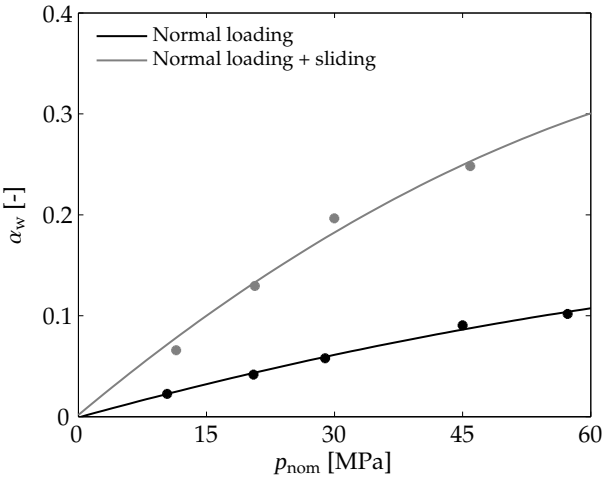

Figure 4.16 *Development real contact area α due to normal loading only and due to normal loading + sliding.*

tool. The height of the peak indicates the amount of deformed surface points. The width of the peak refers to the combined effect of tool asperity indentation and springback of the crushed workpiece asperities after releasing the tool from the workpiece. Since the surface height distributions have been normalized, the area underneath the initiated peak is used as a measure for the fractional real contact area α_w. This fraction reflects the ratio between the surface points which have been in contact with the tool and the total number of surface points.

Figure 4.15 (left) shows that the surface height distribution of non-contacting surface points does not change (part of the solid curves before the initiated peak). This indicates that the non-contacting surface texture is marginally affected by the loading action, which was also observed from the cross-section comparison in Figure 4.12 (right). Comparing the surface height distributions for the loading + sliding case (Figure 4.15 (right)) shows a deviation between the curves for the surfaces in the non-contacting areas. Hence, the shape of the non-contacting surface is slightly affected by the sliding action.

The fractional real contact area is determined by calculating the area underneath the peak caused by deformation, starting from the start of the peak till the right end of the curve. The relation between nominal contact pressure and fractional real contact area is shown in Figure 4.16 for both normal loading only and normal loading + sliding cases. Experimental results are expressed by dots, the overall trend is fitted by a 2^{nd} order polynomial function (the solid lines). It can be seen that the influence of sliding on the fractional real contact area is significant. An

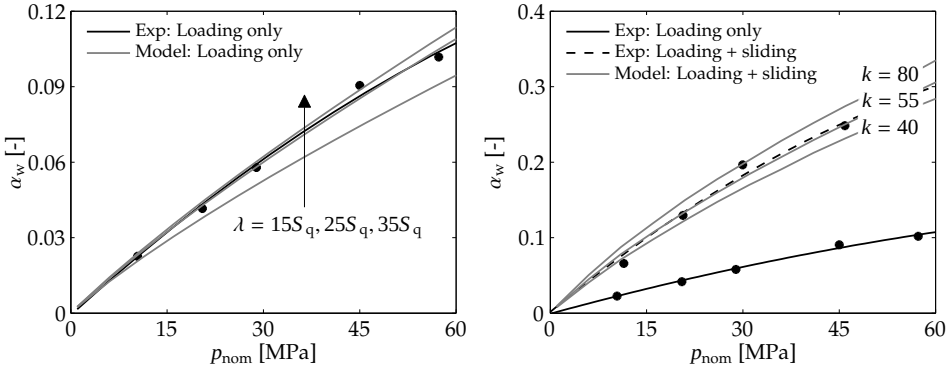

Figure 4.17 *Development real contact area α_w.* ***Left:*** *Due to normal loading.* ***Right:*** *Due to normal loading + sliding.*

increase by a factor of 3 is found over the complete range of nominal contact pressures. For both cases, non-linear behavior of the real contact area as a function of the loading/sliding pressure is observed. The non-linearity is induced by work-hardening effects of the deformed asperities, resulting in a lower than proportional increase in real contact area with nominal contact pressure [15].

4.4.5 Determination of model parameters

The mixed lubrication friction model requires three model parameters to describe the flattening behavior of surface asperities. Two model parameters are introduced in the normal loading model. When accounting for sliding-induced asperity deformation, an additional model parameter is introduced.

Normal loading only

The normal loading model presented in Section 2.3 introduced the persistence parameter η and the reference height of bars λ. The persistence parameter describes the amount of energy required to lift up non-contacting asperities. The reference height of asperities is used to calculate strains and thereby work-hardening effects in deforming surface asperities. Regarding the persistence parameter η, a value of $\eta = 0$ means that no energy is required to lift up the non-contacting surface, while a value of $\eta = 1$ implies that the same energy is required to lift up the surface as to crush the surface. The amount of deformation of raising asperities is difficult to quantify. From the confocal study, see Figure 4.12 and

Figure 4.14, the amount of raising asperities seems insignificant in comparison with the amount of deformation of the crushed asperities. For this reason, the persistence value is set to $\eta = 0$. This implies that a raise of the surface will be calculated by the model, but that no energy is required to do this. Hence, it only costs energy to crush and to shear asperities. To minimize the error between the analytical and experimental real contact area, the value of the reference height λ has been adapted (see Figure 4.17 (left)). The amount of strain build-up in the asperities, and therefore work-hardening effects, will be lower when using a higher value for λ. Consequently, the development in real contact area will be higher. Results using different values for λ are shown in Figure 4.17 (left). The value of λ has been expressed as a function of the RMS surface roughness parameter S_q. It can be observed that the trend in fractional real contact area can be predicted accurately when using a value of $\lambda = 25S_q$ (mean error = 1.4 % compared to the trend line).

Normal loading + sliding

The contact model proposed in Section 2.3.2 accounts for the increase in real contact area due to sliding of contacting surfaces. This model introduced the shear factor k, which modifies the calculated tangential load between the contacting surfaces. The value of k is usually determined based on experiments.

McFlare & Tabor [44] and Courtney-Pratt & Eisner [11] showed that k values around 3 (for sliding steel on indium) and values around 12 (on platinum surfaces), can be expected. Kayaba & Kato [34] found values ranging from 4 till 20 for experiments executed on brass, phosphor-bronze, aluminum and mild steel. Large differences in k values are found in the literature which could either be attributed to the measurement accuracy (different authors used different measurement techniques), or the difference in friction coefficients [34]. Friction coefficients of $\mu \approx 5$ were found by McFlare & Tabor and values of $\mu \approx 0.5$ were found by the other authors.

In this work, the real contact area obtained from normal loading + sliding experiments is used to find a proper value of k. The influence of k on the real contact area is shown in Figure 4.17 (right). An accurate prediction of the development in real contact area is obtained if a value of 55 is used (mean error = 1.5% compared to the trend line). The fitted value for k is higher than found in the literature, which can attributed to the low friction coefficients found, around $\mu = 0.15$, in combination with the relatively high increase in real contact area.

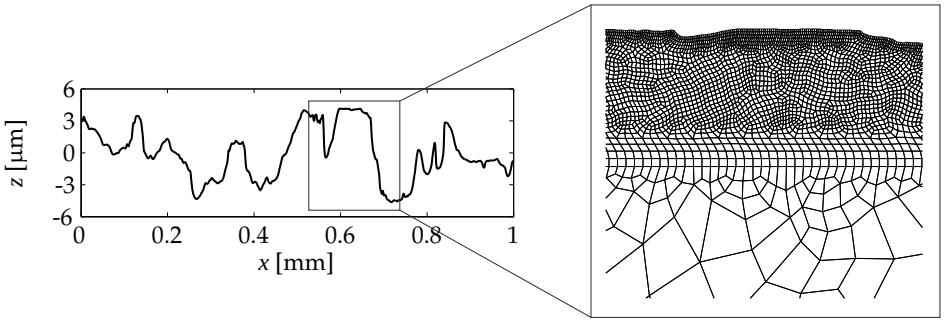

Figure 4.18 ***Left:*** *2D line profile rough surface.* ***Right:*** *FE mesh.*

4.5 Input parameters strain-dependent deformation model

Results obtained from the stretching model presented in Section 2.3.3 are discussed in this section. The stretching model accounts for the increase in real contact area due to combined normal loading and stretching of the underlying bulk material. Results have been compared with FE results on 2D rough surface profiles. The numerical set-up is outlined in Section 4.5.1. The functioning of the analytical strain model for different loading and straining conditions is discussed in Section 4.5.2. Differences have been found between the FE results and the model results, which have been minimized by modifying the input parameters of the strain model, as presented in Section 4.5.3.

4.5.1 Numerical set-up

FE simulations have been performed to simulate the deformation behavior of 2D rough surfaces. For this purpose, surfaces have been deformed by a given normal load and stretched till a predefined strain was present in the underlying bulk material (perpendicular to the direction of normal loading). 2D line profiles have been used to model the deformable rough workpiece surfaces. These line profiles have been subtracted from 3D rough surface measurements, see for an example Figure 4.18 (left). The normal load was applied to a tool surface, which was described by a rigid, perfectly flat surface.

Simulations have been performed using three different roughness profiles, having a length of 4 mm each. See Figure 4.19 (left) for the roughness profiles used and Figure 4.19 (right) for the corresponding surface height distributions.

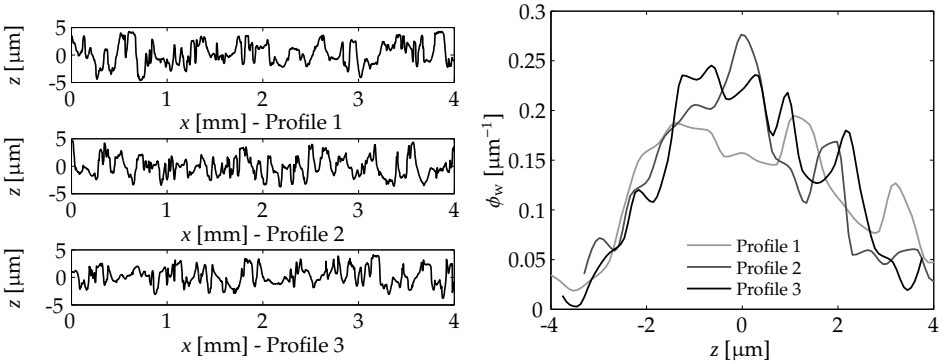

Figure 4.19 ***Left:*** *Roughness profiles used in FEM analyses.* ***Right:*** *Corresponding surface height distributions.*

The height of the bulk material was taken to be 1 mm. The rough surfaces were modeled by quadrilateral 2D plane strain elements, see Figure 4.18 (right). The yield surface was described by the Von Mises yield criterion using the Bergström van Liempt hardening relation to describe work-hardening effects [3, 78, 80]. Material parameters are listed in Table 4.3. The surface height distribution used to solve the analytical normal loading/straining model equals the 2D roughness

Table 4.3 *Von Mises and Bergström-Van Liempt hardening parameters for DC06.*

Material parameter	Value	Unit
Elasticity modulus (E)	210	GPa
Poisson ratio (ν)	0.3	
Initial static stress (σ_{f0})	101.47	MPa
Stress increment parameter ($d\sigma_m$)	251.83	MPa
Linear hardening parameter (β_v)	0.5	
Remobilization parameter (ω)	9.951	
Hardening exponent (n)	0.75	
Initial strain (ε_0)	0.005	
Initial strain rate ($\dot{\varepsilon}_0$)	10^8	
Max. dynamic stress (σ_0^*)	600	MPa
Temperature (t)	300	K
Dynamic stress power (p)	2.2	
Activation energy (ΔG_0)	0.8	J
Boltzmann's constant (k)	8.617×10^{-5}	eV

distribution of the FE simulations. The development in real contact area has been traced during the FE simulations to make a comparison with analytically obtained real contact areas.

4.5.2 Real contact area

Compared to the normal loading only, combined normal loading and stretching the underlying bulk material increases the amount of asperity deformation, see Section 2.3.3. FE simulations using different normal contact pressures and bulk strains have been conducted to validate the analytical strain model. A nominal contact pressure of 1, 5, 10 and 20 MPa was applied to the rough surfaces, after which the underlying bulk material was stretched till a predefined bulk strain of 10 % was reached. Results of both FE simulations and model results are shown in Figure 4.20.

As can be seen, the same trend in fractional real contact areas is found (as a function of strain) and an increase in nominal contact pressure increases the fractional real contact area. However, a significant overestimation in the development of real contact area is made by the analytical strain model. A small overestimation was expected since ideal plastic behavior of deforming surface asperities is assumed within the strain model, while non-linear plastic material behavior was assumed during the FE analysis. Most conceivably, the assumptions made within the analytical strain model do not apply for arbitrary rough surface profiles. First of all, a definition of the velocity parameter W (see Section 2.3.3) is required to describe the flattening behavior of asperities. The expression proposed by Sutcliffe [69] is used for this purpose. Sutcliffe conducted a slip-line analysis based on wedge-shaped asperities, requiring a plane strain assumption and rigid-plastic material behavior. This expression might lose its applicability when applied to arbitrary shaped asperities. In addition, the velocity parameter W requires a definition for the mean half distance l between contacting asperities. An expression for l was proposed in Section 2.3.3 that depends on the asperity density ρ_w (obtained from a 3D rough surface measurement). If ρ_w is obtained from a line profile, the definition of l reads:

$$l = \frac{1}{2\rho_w \alpha_w} \tag{4.1}$$

The asperity density is known to be scale dependent, i.e. different scanning resolutions will yield different values for the asperity density. This means that the results of the analytical strain model relies on the scanning method used, introducing another uncertainty to the model.

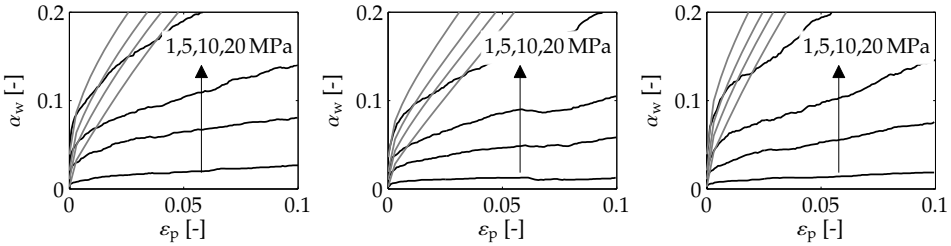

Figure 4.20 *Development real contact area due to straining of surface 1 (left), surface 2 (middle) and surface 3 (right).* ***Black lines:*** *Results of FE simulations.* ***Gray lines:*** *Results of analytical strain model.*

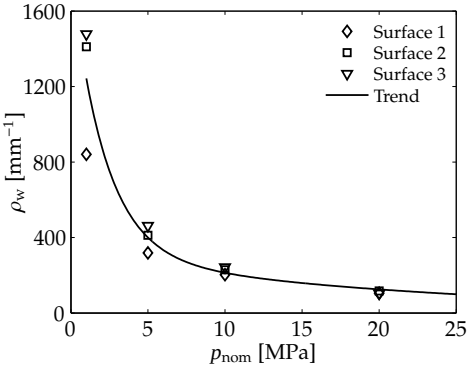

Figure 4.21 *Optimized values for the asperity density ρ_w to adapt the mean half spacing l between asperities.*

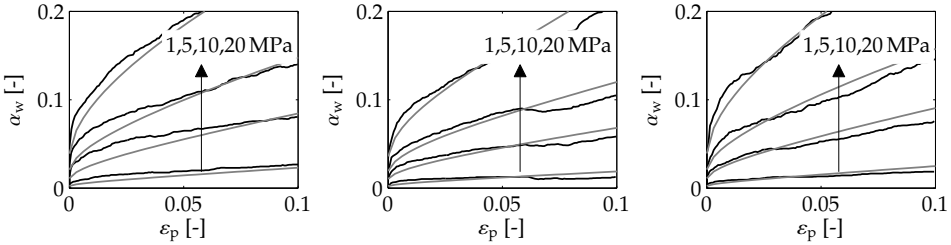

Figure 4.22 *Development real contact area due to straining of surface 1 (left), surface 2 (middle) and surface 3 (right).* ***Black lines:*** *Results of FE simulations.* ***Gray lines:*** *Results of analytical strain model using adapted asperity density ρ_w.*

4.5.3 Determination of model parameters

In the previous section, it was mentioned that the asperity density can be obtained by using a 3-point summit rule, see also Section 4.2. However, to reduce the discrepancy between analytical and FE results, the asperity density has been used as a fitting parameter. That is, the value of ρ_w has been adapted until an error of less than 1 % between the model results and the FE results was found (for the 12 FE results shown in Figure 4.20). The mean value of the fractional real contact area α_w over ε = 0.0-0.1 has been used as an error measure. The calibrated values of ρ_w for the different surfaces, as a function of the nominal contact pressure p_{nom}, are shown in Figure 4.21.

As can be seen, a large decrease in asperity density is found for increasing the nominal contact pressure p_{nom}. The same trend is found for the three different surface profiles, starting with a high value of $\rho_w \approx 1.2 \times 10^3\,\mathrm{mm}^{-1}$ and decreasing towards a value of $\rho_w \approx 100\,\mathrm{mm}^{-1}$ for higher nominal contact pressures. It is noted that these values are unrealistically high, especially for low pressures ($p_{nom} < 10\,\mathrm{MPa}$). Values of $\rho_w \approx 50\,\mathrm{mm}^{-1}$ are found by adopting the 3-point summit rule on the rough surfaces discussed (using a pixel size of 2.2 µm). The asperity density should therefore be seen as a fitting parameter to acquire more reliable results from the analytical strain model, rather than a physical parameter.

An exponential relation is proposed in Equation (4.2) to describe the decrease in asperity density as a function of nominal contact pressure, with ρ_w in mm^{-1} and p_{nom} in MPa. The trend is shown in Figure 4.21. Equation (4.2) is implemented within the analytical strain model, and used to obtain the development in real contact area for the three surfaces discussed. Results are shown in Figure 4.22. It is observed that the FE results can be described well by using the proposed relation. For this reason, the exponential relation is used in the remainder of this thesis to describe the deformation behavior of asperities due to combined normal loading and straining.

$$\rho_w = 1.49 \times 10^3 \exp\left(-0.458 p_{nom}\right) + 3.14 \times 10^2 \exp\left(0.0460 p_{nom}\right) \tag{4.2}$$

Although a good approximation can be made by following this approach, it is noted that the approach does not rely on a physical basis. Other, more advanced models are required to describe the influence of bulk straining effects more accurately, omitting the fitting procedure as discussed in this section.

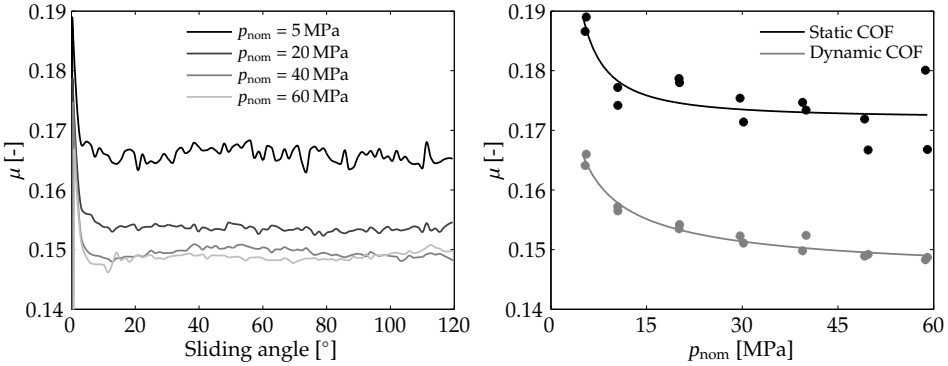

Figure 4.23 ***Left:*** *Friction coefficient as a function of sliding distance.* ***Right:*** *Static and dynamic friction coefficient as a function of nominal contact pressure.*

4.6 Input parameters ploughing model

A deterministic surface description has been used in Section 2.4 to model the influence of ploughing on friction. A parameter has been introduced in this model, which is obtained by friction experiments as discussed in this section. First, results of the friction experiments are presented in Section 4.6.1. Next, experimentally obtained results are used in Section 4.6.2 to quantify the model parameter.

4.6.1 Friction experiments

The rotational friction tester has been used to obtain the relation between the friction coefficient and the applied nominal contact pressure. The same experimental set-up has been used as discussed in Section 4.4.1, except that a larger sliding angle has been used to obtain the dynamic friction coefficient (120° instead of 80°). Conditions of the sliding tests can be found in Table 4.2.

The friction coefficient is derived from the measured load and torque, obtained from the load/torque transducer. The development of the friction coefficient as a function of sliding distance is shown in Figure 4.23 (left). Experiments have been conducted for different constant loading conditions. A clear transition from static to dynamic friction is visible. The friction coefficient starts at a high value, the static friction coefficient, and decreases towards the dynamic friction coefficient at the moment sliding starts. For all measurements, the dynamic friction coefficient evolves to a constant value. The noise on the friction coefficient decreases for

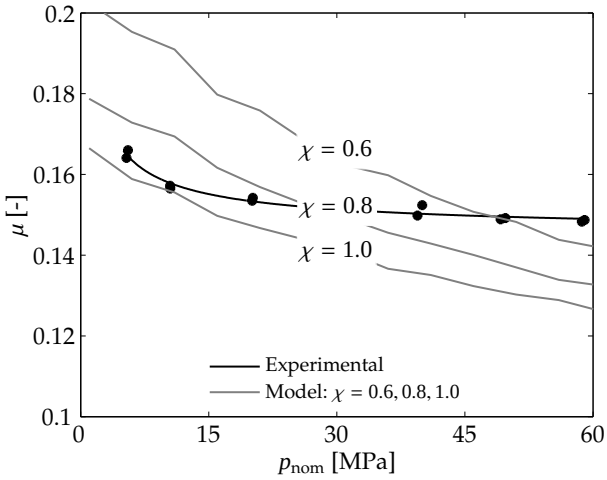

Figure 4.24 *Comparison between experimentally and numerically obtained friction coefficients.*

increasing pressure. The static and dynamic friction coefficient as a function of nominal contact pressure is shown in Figure 4.23 (right). The markers show the experimental values, the solid lines represent trend lines (based on a 2nd order power law). The static friction coefficient equals the maximum value as observed in Figure 4.23 (left). The dynamic friction coefficient equals the averaged value of the friction coefficient between a sliding angle of 20° till 100° in the RFT. Both the static and dynamic friction coefficient decreases with increasing nominal contact pressure. This behavior agrees with observations on coated steels by Emmens [15], on coated and uncoated steels by Schedin [60] and on different steel grades and aluminum alloys by Roll et al. [56] and Filzek et al. [16]. The decrease in friction coefficients can be explained by the ploughing model, as discussed in Section 2.5.

4.6.2 Determination of model parameters

The ploughing model discussed in Section 2.4 accounts for the formation of tool contact patches ploughing through a softer workpiece material. Friction forces are calculated by this model based on a 2D plane strain assumption. For this purpose, the shape factor χ was introduced to describe the 3D nature of contact patches in a 2D expression. The effect of χ on the calculated dynamic friction coefficients is visualized in Figure 4.29. Decreasing the shape factor χ increases the effective attack angle, resulting in higher friction coefficients.

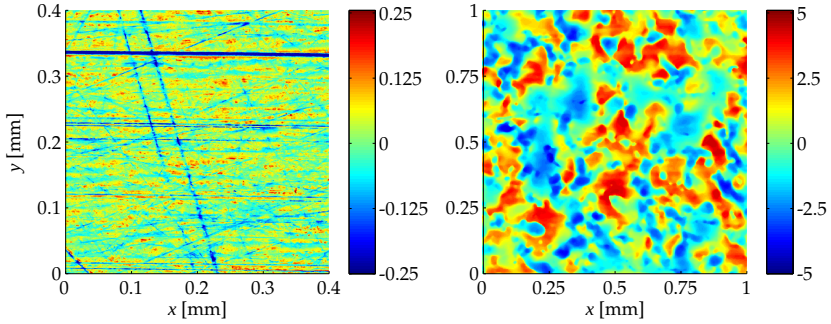

Figure 4.25 *Measured surface height textures (in µm).* ***Left:*** *Tool notch 1 ($S_q = 0.087\,\mu m$).* ***Right:*** *Workpiece surface 1 ($S_q = 1.86\,\mu m$).*

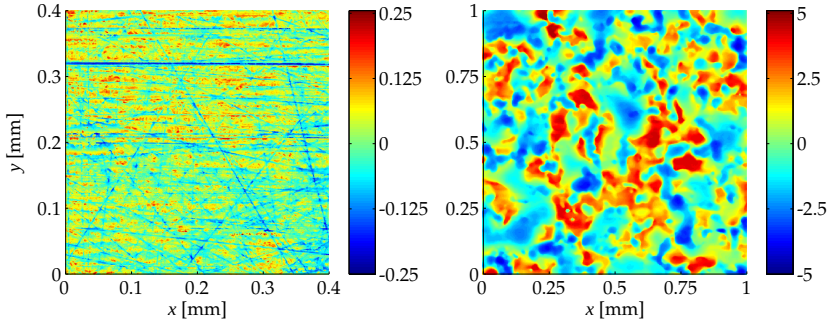

Figure 4.26 *Measured surface height textures (in µm).* ***Left:*** *Tool notch 2 ($S_q = 0.073\,\mu m$).* ***Right:*** *Workpiece surface 2 ($S_q = 1.87\,\mu m$).*

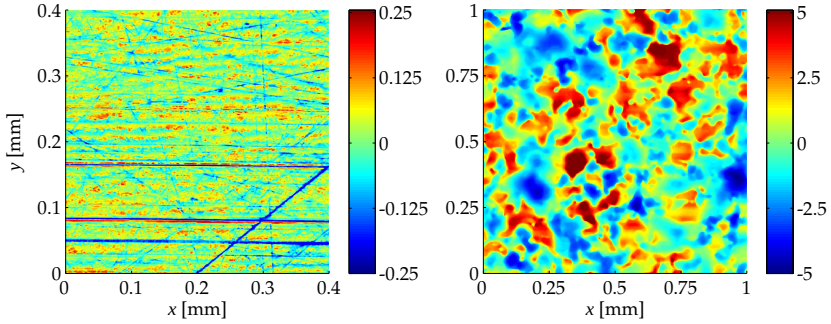

Figure 4.27 *Measured surface height textures (in µm).* ***Left:*** *Tool notch 3 ($S_q = 0.082\,\mu m$).* ***Right:*** *Workpiece surface 3 ($S_q = 1.93\,\mu m$).*

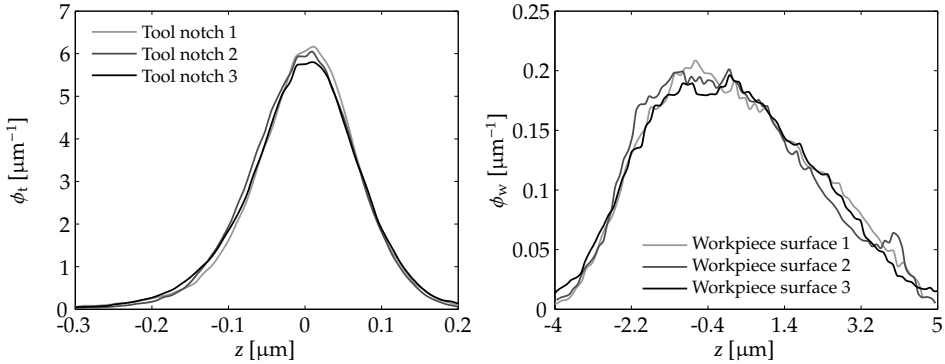

Figure 4.28 *Comparison surface height distributions, corresponding to the surfaces shown in Figures 4.25-4.27.* ***Left:*** *Tool.* ***Right:*** *Workpiece.*

Comparing analytical with experimental results shows that experimental results can be predicted best by using a value of $\chi = 0.8$ (which corresponds to the experimental value obtained by Hokkirigawa & Kato in [28]). Although the calibrated model overestimates the negative correlation between the friction coefficient and the nominal contact pressure, the calculated friction coefficients are within the expected range of experimentally obtained friction coefficients.

4.7 Robustness friction analysis

Model results discussed in this chapter depend on 3D rough surface measurements. In the first section of this chapter, it was stated that a representative surface area should be used to ensure a reliable outcome of the friction model. The representativeness of surface measurements was related to the difference in surface height distributions (by changing the resolution of the scan and the size of the measurement area). To verify this approach, additional friction analyses have been conducted. 3 surface scans of the tool surface (obtained from the different RFT notches) and 3 surface scans of the workpiece surface have been used for this purpose, see Figures 4.25-4.27 for a top view of the measured tool surfaces (left) and of the measured workpiece surfaces (right). Corresponding surface height distributions are shown in Figure 4.28. The influence of different tool/workpiece combinations on calculated friction coefficients is shown in Figure 4.29. The same trend in decreasing friction coefficients is calculated for all friction evaluations. Moreover, the differences in calculated friction curves is acceptable ($\sigma_\mu = 0.003$), although some larger

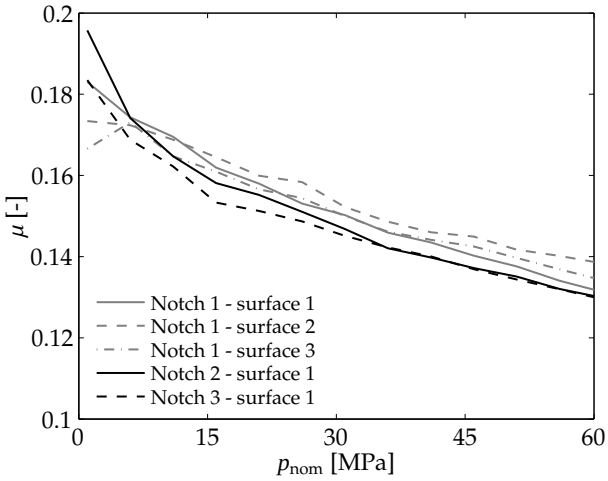

Figure 4.29 *Numerically obtained friction coefficients for different scanned workpiece and tool surfaces.*

variation is found for low nominal contact pressures. It is concluded that the size of the measurement area and the resolution of the surface scan, as proposed in Section 4.2, can be used to perform a representative friction analysis.

Closure

A procedure is proposed in this chapter to determine input parameters of the advanced friction model. A method to obtain a deterministic and stochastic description of 3D rough surfaces is discussed and an experimental procedure is proposed to determine the interfacial shear strength of boundary layers. Loading and sliding experiments have been conducted to investigate the development in real contact area and friction coefficients during sliding. Results have been used to quantify model parameters and to show the predictive capabilities of the advanced friction model.

Chapter 5

Application to forming processes

The developed mixed lubrication friction model is used in FE forming simulations to demonstrate its applicability to metal forming processes. Two deep-drawing applications have been used for this purpose, i.e. a top-hat section and a cross-die product. The influence of boundary and mixed lubrication friction on forming is outlined and a comparison between numerically and experimentally obtained punch force–displacement diagrams is made. First, the application of the mixed lubrication interface elements to FE forming simulations is discussed in Section 5.1. Next, results obtained for the top-hat section are discussed in Section 5.2. In the last section, Section 5.3, results obtained for the cross-die product are reviewed.

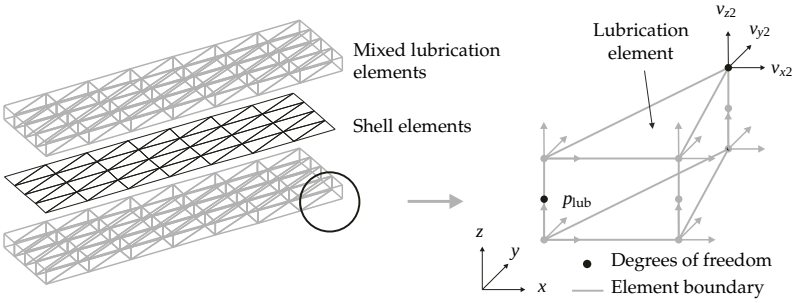

Figure 5.1 *Schematic view of shell and interface elements.*

5.1 Application of interface elements to forming simulations

The mixed lubrication interface elements have been used in two forming applications. To establish a proper description of friction during forming simulations, the following points have been accounted for:

Interface elements

Contact and friction between the tools and the blank are described by the interface elements. The forming behavior of the blank material itself is described by shell elements. Interface elements are attached to the upper and the lower side of the shell elements, describing the frictional behavior on both sides of the blank, see Figure 5.1.

Starvation of lubricant

Starvation of lubricant will occur if insufficient lubricant is present to fill the non-contacting surface pockets, see Section 3.3. Boundary lubrication will dominate in this situation since the lubricant does not carry any load. Starvation is evaluated for each integration point of the interface element in contact with the tooling, for each time step of the forming simulation.

Input mixed lubrication friction model

The hydrodynamic part of the friction model relies on physical parameters only. These parameters are described by the amount of lubricant used, the viscosity of the lubricant and the roughness texture of the workpiece material. The latter parameter is liable to changes due to asperity deformations, which

is determined by the boundary lubrication friction model. Input data for the boundary lubrication friction model is obtained by the experimental procedure as proposed in Chapter 4. The roughness of both the tools and the sheet material have been measured by confocal microscopy, and used accordingly.

Flow factors

Section 3.5 demonstrated the FE implementation of the averaged Reynolds equation by using flow factor expressions of Patir & Cheng [49] and Wilson & Marsault [87]. However, it is unknown whether these flow factors will yield an accurate representation of lubricant flow for the metal–lubricant combinations discussed in this chapter. Flow factor expressions should be determined for the actual metal–lubrication combination used. Since this topic is not part of this research, flow factors have been taken equal to $\mathbf{\Phi}_p \rightarrow \mathbf{I}$ and $\mathbf{\Phi}_s \rightarrow \mathbf{0}$, reducing the averaged Reynolds equation to the standard form of the Reynolds equation.

Squeeze flow

It has been observed that the squeeze term in the Reynolds equation leads to convergence problems of FE forming simulations, yielding erroneous punch forces. The reason for the convergence problems is yet unknown. Therefore, the squeezing term is omitted from the Reynolds equation. However, it is not to be expected that omitting these terms will influence the results too much. Squeezing mainly takes place during closing of the die and the blankholder, which becomes increasingly important for high-speed forming processes [72]. For the forming processes discussed in this chapter, some time was present between closing the forming tools and the start of the actual forming process. This means that squeeze flow is expected to be reduced to a negligible amount at the moment forming starts.

Thin film and thick film lubrication

As presented in Section 3.3, the fluid film thickness is calculated from the amount of deformation of contacting surface asperities. This means that contact between the blank and the dies is required, otherwise no information is available from the boundary lubrication friction model. To describe lubricant flow in the thin film or thick film lubrication regime, a different definition of the fluid film thickness is required. This topic has not been studied in this research.

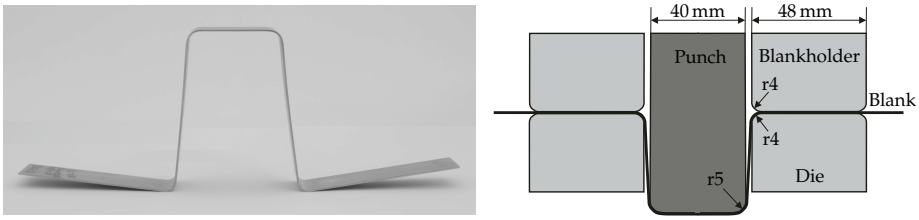

Figure 5.2 ***Left:*** *Picture top-hat section.* ***Right:*** *Schematic view of top-hat section.*

Table 5.1 *Process specifications top-hat section.*

Parameter	Specification
Blank material	DC06 EN10130:2006
Tool material	DIN 1.2379
Blank geometry	$300 \times 25 \times 0.8$ mm
Lubricant1	Quaker FERROCOAT® N6130 (η_{40° = 23 mPas)
Lubricant2	Fuchs Anticorit PLS100T (η_{40° = 90 mPas)
Lubrication amount	0.6 g/m^2 & 2.0 g/m^2
Blankholderforce (F_{bhf})	10 kN, 17.5 kN and 25 kN
Punch velocity (v_{punch})	20.0 mm/s and 50.0 mm/s
Drawing depth	75 mm

5.2 Top-hat section

First the top-hat section is considered, see Figure 5.2 (left). Process specifications of the top-hat section are presented in Section 5.2.1. A distinction is made between boundary lubrication friction and mixed lubrication friction in the two subsequent sections. Friction is dominated by boundary lubrication if starvation of lubricant occurs, which is discussed in Section 5.2.2. A pressure can be generated in the lubricant if sufficient lubricant is available, which is outlined in Section 5.2.3. A comparison with experimental results is made in both sections to demonstrate the predictive capabilities of the advanced friction model.

5.2.1 Process specifications

The top-hat section is formed by a strip drawn into a simple U-shaped profile and is used in practice to, among other things, establish the lubricating behavior of lubricants on (coated and uncoated) blanks under realistic forming conditions.

Table 5.2 *Vegter parameters for DC06.*

Material parameter	0°	45°	90°
R-value	1.85	2.06	2.51
Uniaxial factor (f_{un})	1.0	0.9947	0.9931
Plane-strain factor (f_{ps})	1.2427	1.2476	1.1456
Plane-strain ratio (α)	0.5	0.5	0.5
Pure shear factor (f_{sh})	0.5720	0.5421	0.5002
Equi-biaxial factor (f_{bi})	1.1530		
Equi-biaxial ratio (ρ_{bi})	0.7770		

Table 5.3 *Bergström-Van Liempt hardening parameters for DC06.*

Material parameter	Value	Unit
Initial static stress (σ_{f0})	101.47	MPa
Stress increment parameter ($\mathrm{d}\sigma_{\mathrm{m}}$)	251.83	MPa
Linear hardening parameter (β_{v})	0.5	
Remobilization parameter (ω)	9.951	
Hardening exponent (n)	0.75	
Initial strain (ε_0)	0.005	
Initial strain rate ($\dot{\varepsilon}_0$)	10^8	
Max. dynamic stress (σ_0^*)	600	MPa
Temperature (t)	300	K
Dynamic stress power (p)	2.2	
Activation energy (ΔG_0)	0.8	J
Boltzmann's constant (k)	8.617×10^{-5}	eV

During forming, the sheet experiences a normal stress/bulk strain history which is responsible for surface deformations affecting the frictional behavior.

The top-hat tooling consists of a punch, a die and a blankholder, see Figure 5.2 (right). The radii of the die shoulder and the punch shoulder are 4 mm and 5 mm, respectively. The punch has a width of 40 mm, the blankholder and die have a width of 48 mm. Strips of 300 × 25 mm with a thickness of 0.8 mm have been used. The punch stroke has been set to 75 mm. The process specifications are listed in Table 5.1. Experiments have been conducted under different loading and lubrication conditions, i.e. the blankholder force, the amount of lubricant applied to the blank surface and the type of lubricant have been varied.

For the FE simulations, the workpiece was meshed with 3750 triangular discrete Kirchhoff shell elements using 3 integration points in plane and 11 integration

points in thickness direction. Only a quarter of the product was modeled due to symmetry. The rigid tooling was described by analytical surfaces. The yield surface of the blank material was described by the Vegter model [80] using the Bergström–Van Liempt hardening relation [76]. Material parameters used to describe the yield curve are given in Table 5.2, parameters to describe the hardening relation are given in Table 5.3.

5.2.2 Boundary lubrication friction

From top-hat section simulations it was found that starvation of lubricant occurs if a lubrication amount of $0.6\,\mathrm{g/m^2}$ is used, meaning that only boundary lubrication friction takes place. The same frictional behavior is known from practice. To discuss friction in the boundary lubrication regime, experiments and simulations have therefore been performed using a lubrication amount of $0.6\,\mathrm{g/m^2}$.

Evolution of friction

Figure 5.3 (left) shows a contour plot of friction coefficients at 55 mm punch displacement. Results are shown for the lower side of the blank, representing the side of the blank in contact with the die. The gray area indicates that there is no contact, hence no friction coefficients are calculated for this region. Zooming-in on the contact zone shows a variation in friction coefficients from the flat die region towards the die shoulder, see Figure 5.3 (top right). The evolution of friction coefficients is mainly dominated by the variation in nominal contact pressures within this region, since strains within the blank are relatively low. The evolution of friction from the die region towards the outlet of the die shoulder can be described as follows (see Figure 5.3 (bottom right) for the areas A1-A3):

A1: The blankholder force is carried over a large area within the die region, resulting in low nominal contact pressures and subsequently higher friction coefficients compared to values found within the die shoulder ($\mu \approx 0.17$). This observation can be directly correlated to the calculated friction coefficients in Section 2.5.

A2: In general, the nominal contact pressure increases towards the die shoulder, decreases at the middle and increases again towards the outlet. This region is characterized by sliding under high nominal contact pressures and surface strains due to bending and unbending of the blank. The relatively high nominal contact pressures yield friction coefficients around $\mu \approx 0.11$.

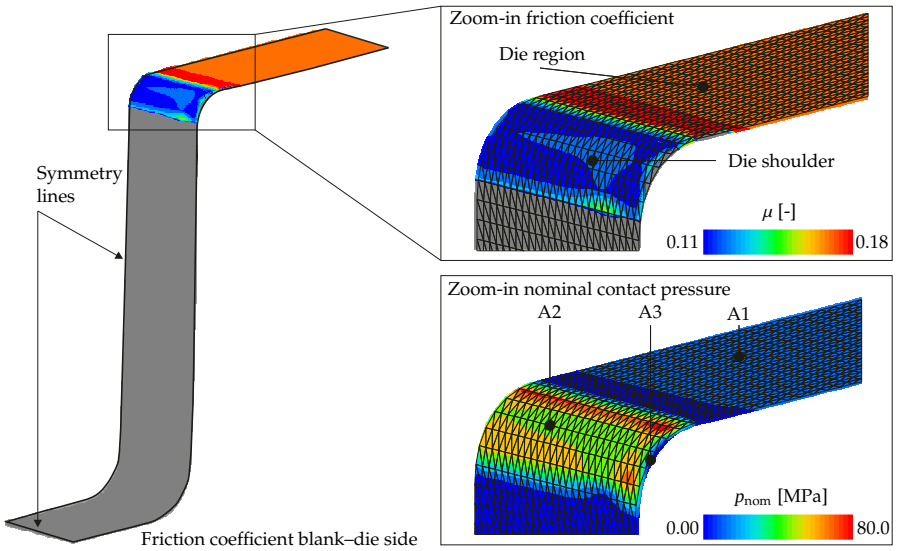

Figure 5.3 *Impression numerically obtained friction coefficients top-hat section at 55 mm punch displacement for 0.6 g/m² of lubricant (v_{punch} = 20 mm/s and F_{bhf} = 25 kN). **Left:** Distribution friction coefficients blank–die side. **Top right:** Zoom-in on friction coefficient. **Bottom right:** Zoom-in on nominal contact pressure.*

Somewhat higher friction coefficients are found at the middle of the die shoulder ($\mu \approx 0.12$) due to a decrease in nominal contact pressures.

A3: The reduction in nominal contact pressures near the edge of the blank is most likely caused by anticlastic bending. Consequently, a variation in friction coefficients is observed in this region.

Comparison with experiments

The experimentally and numerically obtained punch force–displacement diagrams are compared in Figure 5.4. Experiments have been conducted using a punch velocity of 20 mm/s, lubricated with Quaker N6130. A lubrication amount of 0.6 g/m² was applied to the sheet surfaces before executing the experiments.

Figure 5.4 (top) shows that the punch force evolves to a steady-state value for all experiments. The small variation in punch forces between triplicates demonstrates the good repeatability of the experiments. As can be seen, the trend of the experimental punch force–displacement diagrams can be predicted precisely by using the proposed mixed lubrication friction model. Only for

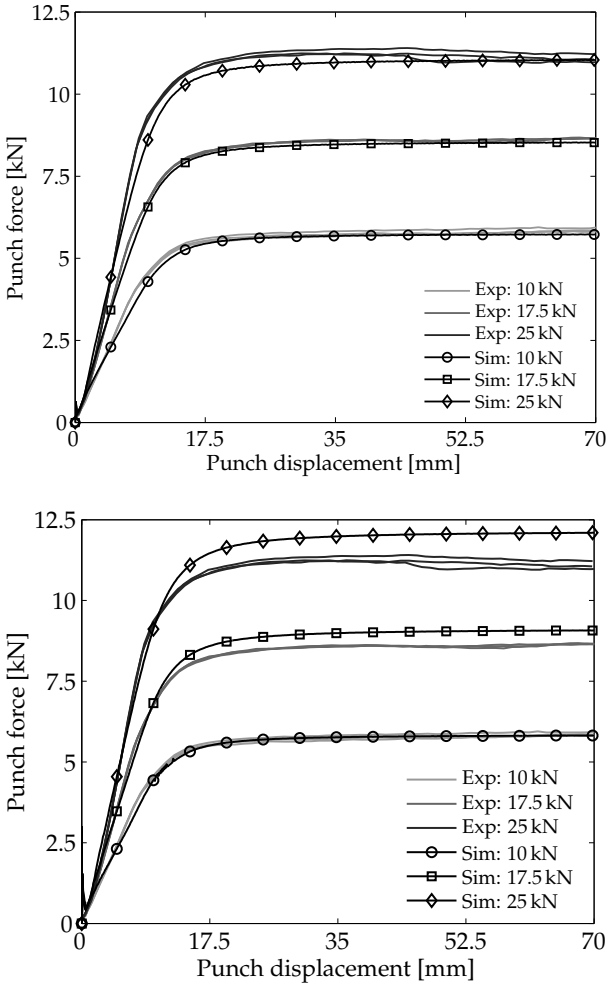

Figure 5.4 *Punch force–displacement diagrams for different blankholder forces, lubrication amount* = $0.6\,g/m^2$ *and* v_{punch} = 20 *mm/s.* ***Top:*** *Using the advanced friction model.* ***Bottom:*** *Using the Coulomb friction model.*

the 25 kN case a small underestimation in punch forces is found, which in all likelihood could be attributed to an underestimation of friction coefficients. The increase in computation time compared to using a Coulomb friction model was around 50 %. Since only boundary lubrication friction occurred, the computation time could be reduced significantly by using the boundary lubrication friction model directly (see Section 2.5). This excludes the use of mixed lubrication interface elements. In this case, the simulation time increases by less than 3 %

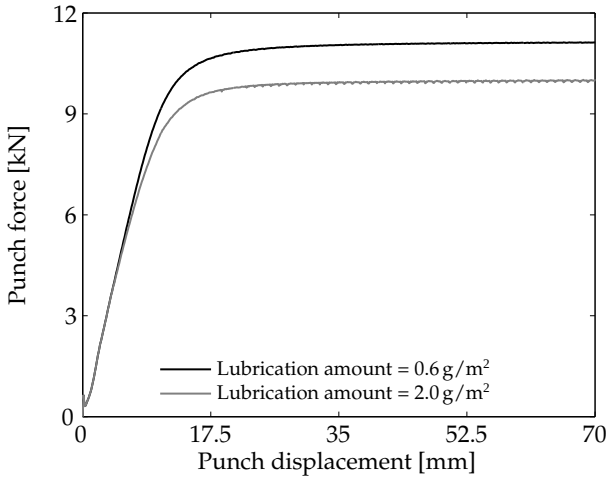

Figure 5.5 *Simulated punch force–displacement curves for the top-hat section using different lubrication amounts (v_{punch} = 50 mm/s and F_{bhf} = 25 kN).*

compared to using a Coulomb friction model.

Figure 5.4 (bottom) shows a comparison between the experimental results and FE results using the classical Coulomb friction law. The value of the (constant) friction coefficient is generally unknown in advance and is often adapted based on a trial-and-error approach to mimic experimentally obtained punch forces. The same holds for the results shown in Figure 5.4 (bottom), where the Coulomb friction coefficient is obtained by minimizing the error between model and experimental punch forces. Experimentally obtained punch forces with a blankholder force of 10 kN have been used for this purpose, resulting in a friction coefficient of $\mu = 0.155$. It is observed that a good approximation can be made by using this value. However, when the blankholder force is increased, the FE results and experimental results start to deviate. In other words, to describe the punch force–displacement diagram, the friction coefficient has to be refitted for each used blankholder force. However, a good agreement for all three blankholder forces is obtained using the advanced friction model.

5.2.3 Mixed lubrication friction

Figure 5.5 shows simulated punch force–displacement diagrams for two different lubrication amounts. Practical values of 0.6 g/m^2 and 2.0 g/m^2 have been used for the simulations. For the 2.0 g/m^2 case, the interface elements predicted that no starvation of lubricant occurs. This means that a pressure build-up can be

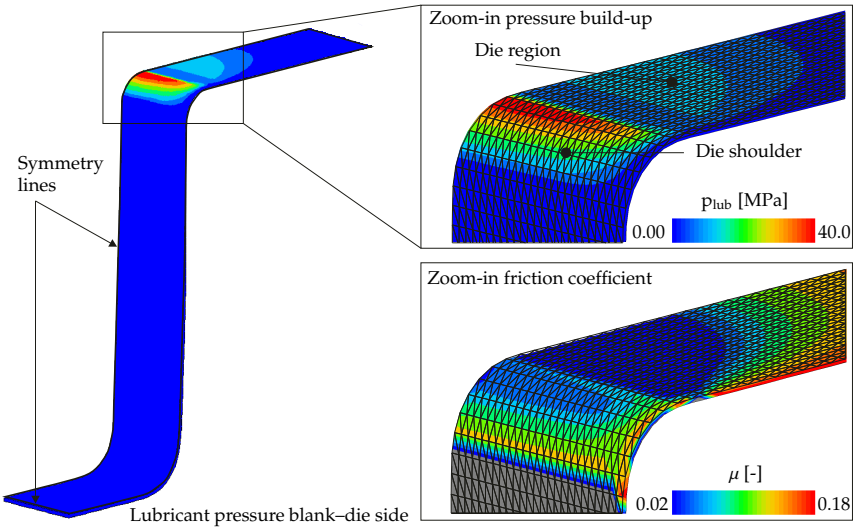

Figure 5.6 *Impression numerically obtained lubricant pressure distribution top-hat section at 55 mm punch displacement using 2.0 g/m^2 of lubricant (v_{punch} = 50 mm/s and F_{bhf} = 25 kN). **Left:** Distribution lubricant pressure blank–die side. **Top right:** Zoom-in on lubricant pressure distribution. **Bottom right:** Zoom-in on friction coefficient.*

generated in the fluid, contributing to the load-carrying capacity of the lubricant. Simulations and experiments have therefore been performed using a lubrication amount of 2.0 g/m^2.

Evolution of friction

Figure 5.6 shows a contour plot of the lubricant pressure distribution at 55 mm punch displacement. Results are shown for the lower side of the blank, describing the side of the blank in contact with the die. As can be seen, a low pressure is generated in the lubricant in the flat die region (see Figure 5.6 (top right)). The strip slides over the die surface, where the deformed surface asperities generate a converging wedge due to a variation in nominal contact pressures in this region. Lubricant pressures up to 40 MPa are found at the die shoulder, meaning that a large part of the nominal contact pressure is carried by the lubricant. The lubricant pressure is symmetric along the symmetry axis and reduces to zero towards the free edges of the strip, demonstrating a correct handling of the boundary conditions applied in the FE simulation.

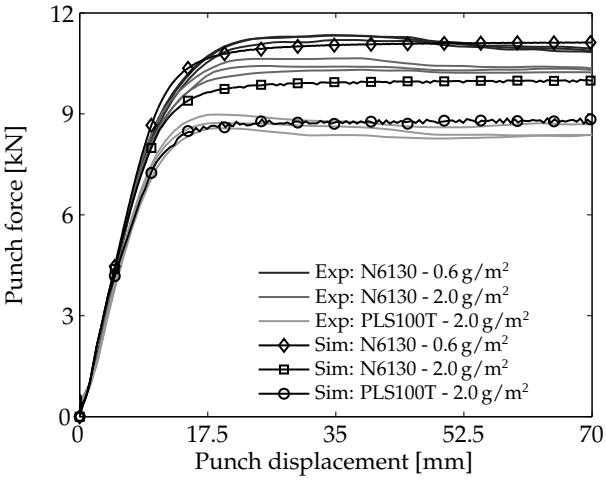

Figure 5.7 *Punch force–displacement diagrams for different lubrication amounts and lubricant types (v_{punch} = 50 mm/s and F_{bhf} = 25 kN).*

The influence of the lubricant pressure on the friction coefficient is clearly visible in Figure 5.6 (bottom right). If the lubricant pressure is low, the friction coefficient is dominated by boundary lubrication friction. Relatively high friction coefficients are observed towards the free edges of the strip and towards the regions where the shell elements lose contact with the tooling, indicated by the gray areas. If friction coefficients lower than 0.18 are found, mixed lubrication takes place. If the friction coefficient drops to values around 0.02, as is the case in Figure 5.6 (bottom right), the transition towards the thin film lubrication regime is reached.

The friction coefficient is directly related to the load-carrying capacity of the lubricant, see Section 3.5. The load-carrying capacity depends on, among other things, the sliding velocity, the amount of lubricant and the viscosity of the lubricant. Therefore, the friction coefficient, and hence the predicted punch force, depends on these operational parameters.

Comparison with experiments

To validate the friction model, a comparison is made between experimentally and numerically obtained punch force–displacement curves. Figure 5.7 shows the results for two lubricant amounts and two different lubrication types. It is noted that for the DC06-PLS100T material-lubricant combination the input parameters as presented in Chapter 4 have been used.

The punch force converges to a steady-state value for all experiments. The low variation in punch forces between triplicates demonstrates the good repeatability of the experiments. Increasing the lubrication amount from $0.6\,g/m^2$ to $2.0\,g/m^2$, decreases the experimentally obtained punch force to form the top-hat section. The same observation can be made from the simulation results, although the load-carrying capacity of the lubricant is slightly overestimated for N6130, indicated by an underestimation of the required punch force. The high viscosity lubricant PLS100T lowers the punch forces further, demonstrating an increased load-carrying capacity of the lubricant. Also, for the PLS100T lubricant an accurate prediction of the experimental punch force–displacement diagram is made by the simulations. The influence of velocity on the punch force–displacement diagram is not investigated in this research. However, it can be expected that increasing the velocity will also result in a reduction of the required punch forces.

Different (constant) friction coefficients will be required to describe the experimental results by a Coulomb friction model. The decrease in friction coefficients is accounted for by the proposed mixed lubrication friction model, which predicts lower friction coefficients for a higher lubrication amount, or a higher viscosity of the lubricant. This result clearly demonstrates the good predictive capabilities of the mixed lubrication friction model. A similar increase in computation time was found as for the boundary lubrication friction simulations, approximately 50 % compared to using a Coulomb friction model.

5.3 Cross-die product

Next, the deep-drawing process of the cross-die product is considered. First, the process specifications are discussed in Section 5.3.1. As for the top-hat section, a distinction is made between boundary lubrication friction and mixed lubrication friction. Friction in the boundary lubrication regime is discussed in Section 5.3.2. The influence of mixed lubrication on friction is outlined in Section 5.3.3. A comparison between numerically and experimentally obtained punch force–displacement diagrams is made in both sections to illustrate the performance of the mixed lubrication friction model for a complex metal part.

5.3.1 Process specifications

The cross-die product is a product designed by Renault [42], see Figure 5.8. The cross-die product mimics process conditions of automotive parts, introducing

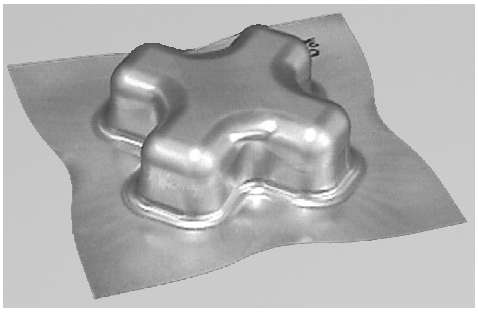

Figure 5.8 *Picture cross-die product.*

complex stress–strain paths in the material and changing contact conditions during forming.

The cross-die tooling consists of a cross-shaped punch, blankholder and die, see Figure 5.9 (left). The dimensions of the blank are 260×260 mm having a thickness of 0.8 mm. The punch stroke has been set to 60 mm. Process settings of the cross-die experiment are listed in Table 5.4. Lubrication amounts of $0.6\,\mathrm{g/m^2}$ and $1.2\,\mathrm{g/m^2}$ have been used for the experiments.

For the FE simulations a quarter of the cross-die process was modeled because of symmetry. The tooling was assumed rigid. The blank was meshed with 20.000 triangular discrete Kirchhoff shell elements using 3 integration points in plane and 11 integration points in thickness direction. Material parameters are given in Table 5.2 and Table 5.3.

Table 5.4 *Process specifications cross-die product.*

Parameter	Specification
Blank material	DC06 EN10130:2006
Tool material	DIN 1.2379
Blank geometry	$260 \times 260 \times 0.8$ mm
Lubricant	Quaker FERROCOAT® N6130 ($\eta_{40^\circ} = 23$ mPas)
Lubrication amount	$0.6\,\mathrm{g/m^2}$ & $1.2\,\mathrm{g/m^2}$
Blankholderforce	120 kN, 150 kN and 170 kN
Drawing velocity	25 mm/s
Drawing depth	60 mm

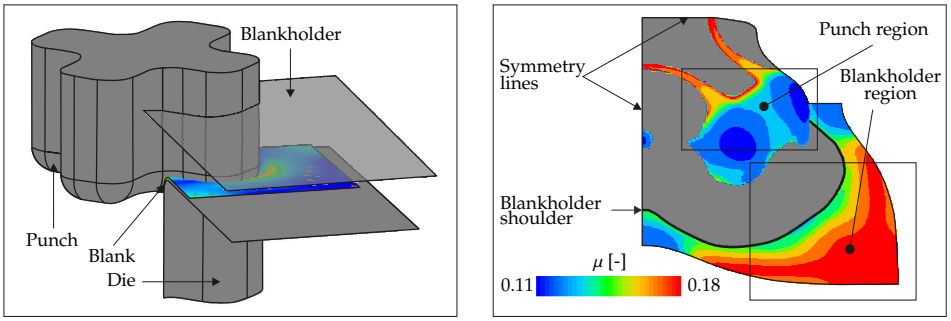

Figure 5.9 ***Left:*** *Schematic view cross-die product.* ***Right:*** *Distribution of friction coefficients at the upper side of the sheet (punch displacement = 60 mm, lubricant amount = 0.6 g/m^2, v_{punch} = 25 mm/s and F_{bhf} = 150 kN).*

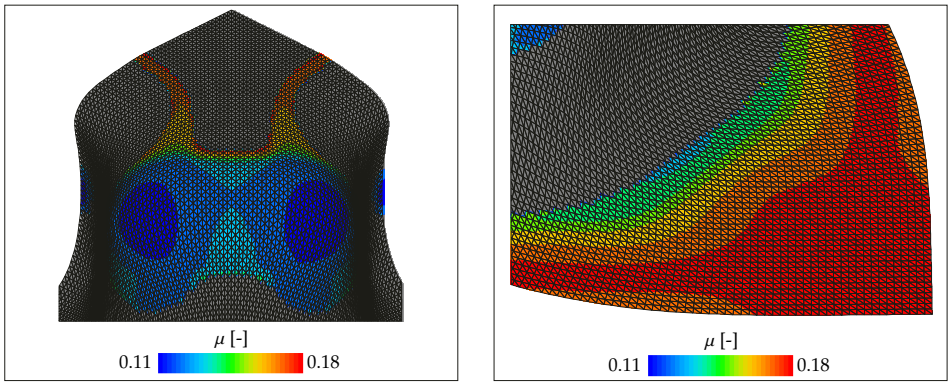

Figure 5.10 *Impression numerically obtained friction coefficients cross-die product at 60 mm punch displacement using 0.6 g/m^2 of lubricant (v_{punch} = 25 mm/s and F_{bhf} = 150 kN).* ***Left:*** *Zoom-in punch region.* ***Right:*** *Zoom-in blankholder region.*

5.3.2 Boundary lubrication friction

To discuss the evolution of friction in the boundary lubrication regime, experiments and simulations have been conducted using a lubrication amount of 0.6 g/m^2.

Evolution of friction

Figure 5.9 (right) shows the distribution of friction coefficients at 60 mm punch displacement. Results are shown for the side of the blank in contact with

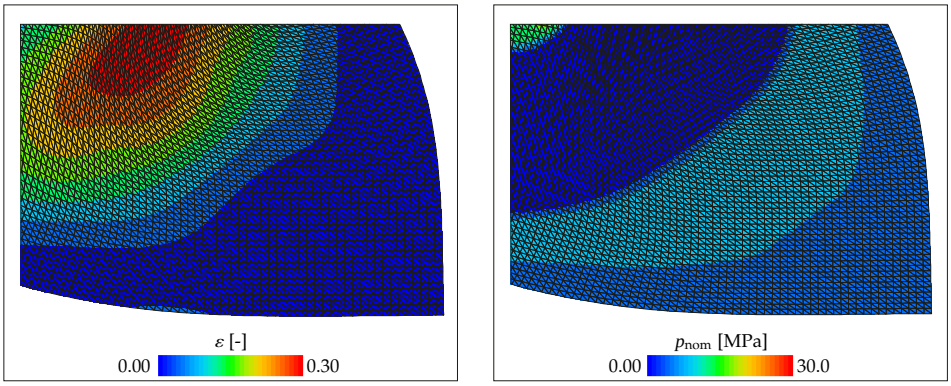

Figure 5.11 *Zoom-in on local process conditions in the blankholder region (punch displacement = 60 mm, lubricant amount = 0.6 g/m², v_{punch} = 25 mm/s and F_{blhf} = 150 kN). **Left:** Distribution in thickness strains. **Right:** Distribution in nominal contact pressures p_{nom}.*

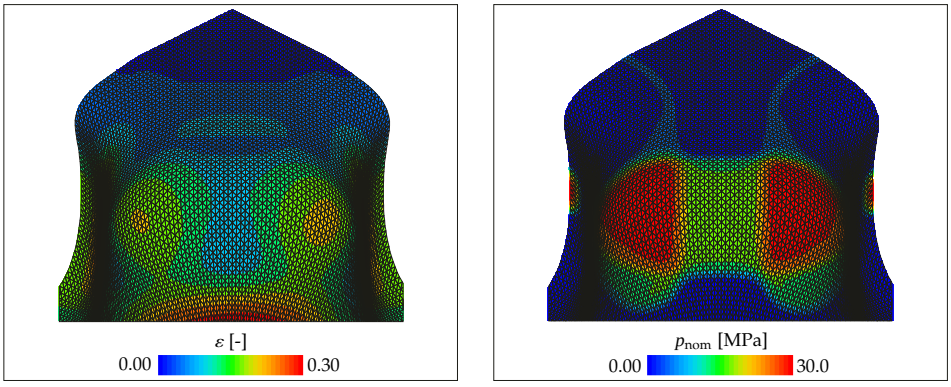

Figure 5.12 *Zoom-in on local process conditions in the punch region (punch displacement = 60 mm, lubricant amount = 0.6 g/m², v_{punch} = 25 mm/s and F_{blhf} = 150 kN). **Left:** Distribution in thickness strains. **Right:** Distribution in nominal contact pressures p_{nom}.*

the punch. Friction conditions are influenced by the strains within the sheet material and nominal contact pressures between the tooling and the blank. The distribution of strains and nominal contact pressures are shown in Figure 5.11 for the punch region and in Figure 5.12 for the blankholder region. In the blankholder region, relatively low strains and pressures are found. This results in a near constant distribution of friction coefficients around $\mu \approx 0.18$, see Figure 5.10 (right). The strain within the blank increases significantly towards

the blankholder shoulder, yielding a decrease in friction coefficients in this region towards $\mu \approx 0.14$. A significant variation in strains and nominal contact pressures can be observed in the punch region, see Figure 5.12. The highest strains and nominal contact pressures are found at the punch corners, where friction coefficients decrease towards $\mu \approx 0.11$. Away from the punch corners, lower strains and nominal contact pressures are observed, consequently leading to higher friction coefficients.

Comparison with experiments

Figure 5.13 shows numerically and experimentally obtained punch force–displacement diagrams for different blankholder forces. It is observed that the trend in the development of punch forces is in good agreement with the experimental results (see Figure 5.13 (top)). Starvation of lubricant was predicted by the interface elements, meaning that friction is dominated by boundary lubrication friction. Punch forces are slightly overestimated for punch displacements between 10 mm and 60 mm. The overestimation can be caused by the boundary lubrication friction model, but also by the material model used during the forming simulation. That is, in the cross-die sample the material is much more deformed than in the top-hat section, reducing the relative influence of friction on punch forces. Although an overestimation in punch forces is predicted for all blankholder forces, overall trends are predicted correctly. The increase in simulation time compared to using a Coulomb friction model was approximately 50 %. By using the boundary lubrication friction model directly (without using the mixed lubrication interface elements), the simulation time increases by less than 2 % compared to using a Coulomb friction model.

Figure 5.13 (bottom) shows a comparison between numerical and experimental punch forces when using the Coulomb friction model. A constant friction coefficient of $\mu = 0.16$ was used. This value has been obtained from fitting the numerical punch force results to the experimental punch force results when a blankholder force of 120 kN was used. The overall trend is predicted correctly, and corresponds to the trend found when using the mixed lubrication friction model. However, as for the top-hat section, increasing the blankholder force increases the gap between experimental and numerical punch forces.

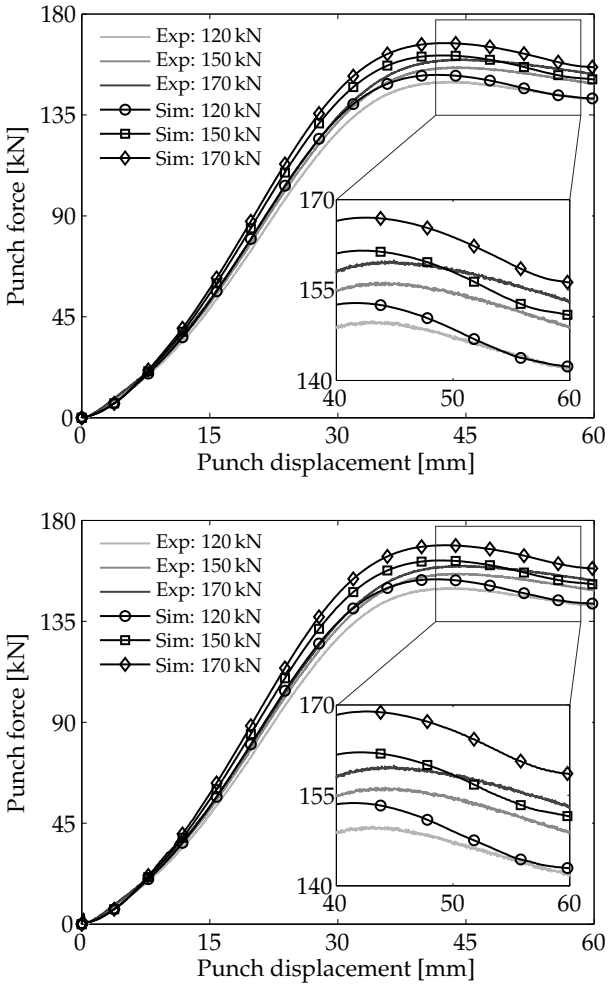

Figure 5.13 *Punch force–displacement diagrams different blankholder forces, lubrication amount* $= 0.6\,g/m^2$ *and* $v_{punch} = 25\,mm/s$. ***Top:*** *Using the advanced friction model.* ***Bottom:*** *Using the Coulomb friction model.*

5.3.3 Mixed lubrication friction

Cross-die experiments have also been conducted using a lubrication amount of $1.2\,g/m^2$. Numerically and experimentally obtained punch-force displacement diagrams are compared to discuss the prediction of friction in the mixed lubrication regime.

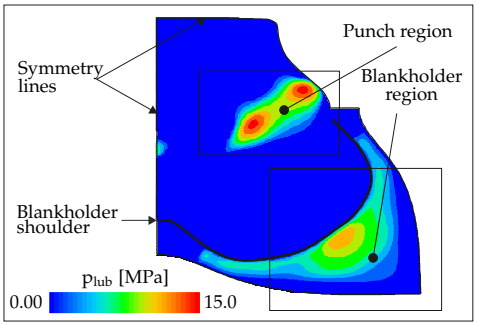

Figure 5.14 *Lubricant pressure distribution at the lower side of the sheet (punch displacement = 60 mm, lubricant amount = 2.0 g/m², v_{punch} = 25 mm/s and F_{bhf} = 150 kN).*

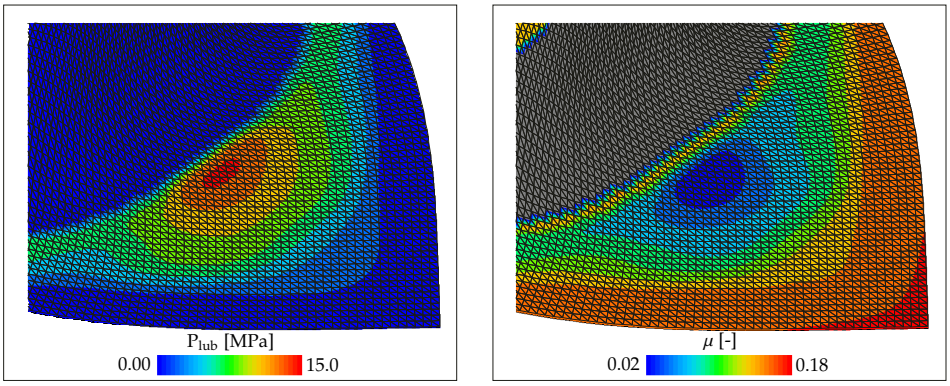

Figure 5.15 *FE results blankholder region at the lower side of the sheet (punch displacement = 60 mm, lubricant amount = 2.0 g/m², v_{punch} = 25 mm/s and F_{bhf} = 150 kN).* ***Left:*** *Lubricant pressure distribution.* ***Right:*** *Friction coefficients.*

Evolution of friction

Figure 5.14 shows the distribution of lubricant pressures at 60 mm punch displacement. Results are shown for the punch side of the sheet. As for the top-hat section, asperity flattening takes place in contact regions supporting the pressure build-up in the lubricant. For the punch region, high nominal contact pressures are present between the punch corners and the sheet, accumulating severe asperity flattening in this region. Sheet material slides over the punch corners introducing a lubricant pressure build-up in this region. Contact in the blankholder region is characterized by lower nominal contact pressures, which increases towards the blankholder shoulder. The increase in nominal

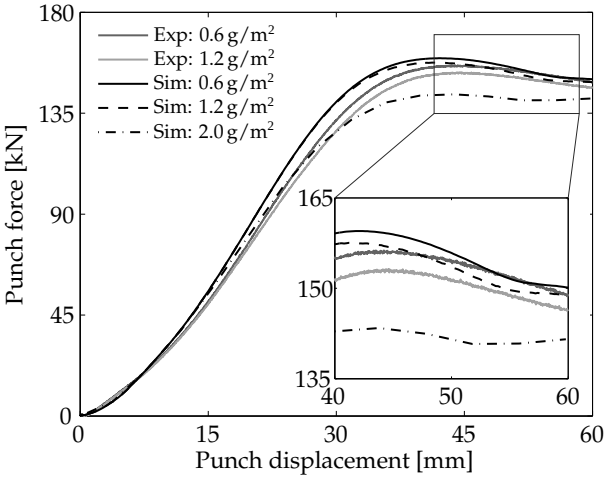

Figure 5.16 *Punch force–displacement diagrams different lubrication amounts (v_{punch} = 25 mm/s and F_{blhf} = 150 kN).*

contact pressure introduces a converging wedge, formed by the deformed surface asperities. This converging wedge supports hydrodynamic effects within the lubricant, increasing the load-carrying capacity of the lubricant. The lubricant pressure distribution underneath the blankholder region is shown in Figure 5.15 (left). The effect of the lubricant pressure on the friction coefficient is shown in Figure 5.15 (right). As expected, a decrease in friction coefficients is found for an increasing load-carrying capacity of the lubricant. Values are found around 0.02, reflecting the transition from mixed lubrication towards thin film lubrication in this region. The friction coefficient is dominated by boundary lubrication friction near the free edges of the sheet and towards the area where the blank loses contact with the tooling, i.e. the gray area in Figure 5.15 (right).

Comparison with experiments

Figure 5.16 shows experimental punch force–displacement diagrams for two different lubrication amounts, i.e. 0.6 g/m^2 and 1.2 g/m^2. Increasing the lubrication amount decreases the punch force, indicating that part of the contact load is carried by the lubricant.

The numerical results for three different lubrication amounts, i.e. 0.6 g/m^2, 1.2 g/m^2 and 2.0 g/m^2, are shown in Figure 5.16 as well. The trends of the experimental punch force–displacement diagrams are in good agreement with the experimental results. Starvation of lubricant was predicted for the 0.6 g/m^2

case. For the $1.2\,g/m^2$ case, partial starvation was predicted by the interface elements. That is, in high pressure regions, where severe asperity flattening takes place, enough lubricant is present to initiate lubricant flow. The influence of partial starvation on the punch force–displacement diagram is shown in Figure 5.16. The lubricant pressure lowers the friction coefficient, causing a decrease in obtained punch forces. Comparing FE results with experimental results shows a similar trend in decreasing punch forces for increasing lubrication amounts, demonstrating the good predictive capabilities of the mixed lubrication friction model. A situation for which no starvation of lubricant will occur is established by using a lubrication amount of $2.0\,g/m^2$. A further decrease in punch forces is predicted due to the increased load-carrying capacity of the lubricant. A comparison with experiments could unfortunately not be made, since experimental results for the $2.0\,g/m^2$ case were not available. An increase of approximately 55 % in computation time was observed compared to using a Coulomb friction model.

Closure

Two deep-drawing applications have been used to present the predictive capabilities of the mixed lubrication friction model. From numerical simulations, a distribution in friction coefficients is obtained that changes in time and depends on external process settings like the blankholder force, the amount of lubricant and the type of lubricant. Numerically obtained punch force–displacement diagrams are in good agreement with experimental results. The friction model is especially useful for friction dominated processes, like thin sheet forming processes or forming processes where low deformation energies are involved. The increase in simulation time compared to using a Coulomb friction model was approximately 50 % for all simulations.

Contrary to the Coulomb based friction model, the proposed friction model does not require any adaptions to the original input data when process settings are changed. An accurate prediction of friction during forming can be made by using the mixed lubrication friction model, rather than fitting the FE data to experiments using a constant friction coefficient.

Chapter 6

Conclusions and recommendations

In the introduction to this thesis it was stated that an accurate prediction of forming processes can only be made if, among other things, friction between the sheet material and the tools is modeled correctly. The objective of this research was therefore to develop a physically based friction model that is computationally attractive for use in metal forming simulations. To achieve this goal, a multi-scale friction model has been developed, describing friction in both the boundary lubrication regime and the mixed lubrication regime. Conclusions are drawn and recommendations for future research topics are given in this chapter.

6.1 Conclusions

The developed boundary lubrication friction model has been described in Chapter 2. As an input, the model requires 3D tool/workpiece surfaces, a relation to describe the boundary layer shear strength and specific model parameters. Both the change in surface topography and the evolution of friction is taken care of by the boundary lubrication friction model. The following conclusions are drawn from Chapter 2:

- Increasing the nominal contact pressure or increasing the bulk strain both result in larger real contact areas.
- Larger real contact areas result in decreasing effective attack angles and a decreasing number of active contact patches, yielding lower friction coefficients. Credible friction coefficients are obtained.
- The direction dependency of friction due to anisotropic surface textures can be accounted for.
- An efficient coupling with FE forming simulations can be made by generating friction matrices for a predefined range of nominal contact pressures and strains.

The boundary lubrication friction model has been extended in Chapter 3 to account for mixed lubrication friction. The required lubricant film thickness is based on the amount of lubricant present in non-contacting surface pockets, obtained from the boundary lubrication friction model. A mixed lubrication interface element has been developed and implemented in an FE software code. 1D and 2D fluid flow test cases have been used to demonstrate the performance of the interface elements. The following is concluded:

- The hydrodynamic part of the mixed lubrication friction model depends on physical parameters only, i.e. the amount of lubricant applied to the surface, the viscosity of the lubricant and the roughness texture of the workpiece surface.
- The 2D (averaged) Reynolds equation is solved correctly by using the mixed lubrication interface elements.
- Increasing the contact length, increasing the sliding velocity or increasing the nominal contact pressure, increases the load-carrying capacity of the lubricant and lowers the friction coefficient.
- Surface roughness can have a significant influence on the load-carrying capacity of the lubricant, which increases for decreasing surface separations.
- Stribeck curves can be generated, demonstrating a change in transition points if process conditions are changed (like the size of the contact zone,

the nominal contact pressure or the strain in the material).
- On the whole, a credible distribution in friction coefficients is obtained by using the mixed lubrication friction model.

The experimental procedure to determine the input parameters of the mixed lubrication friction model is explained in Chapter 4. The experimental procedure should be executed for each metal–lubricant combination of interest. One metal–lubricant combination is discussed in this thesis, from which the following conclusions are drawn:

- **Boundary layer shear strength:** The shear strength increases with increasing nominal contact pressures. The lubrication amount does not influence friction significantly, though the trend in shear strength is affected slightly. A power law relation can be used to describe the boundary layer shear strength empirically.
- **Real contact area:** Normal loading has only little effect on asperity deformation, while simultaneous sliding increases the real contact area significantly. A factor of 3 over the complete range of nominal contact pressures was found. No significant raise of non-contacting asperities was observed. Experimental results are used to calibrate the asperity flattening models incorporated in the friction model. The real contact area, for both normal loading and normal loading + sliding cases, is predicted accurately by the calibrated model. A further increase in real contact area is caused by combined normal loading and straining of the underlying bulk material (shown by FE simulations). The straining model is not able to predict the development in real contact area accurately, however, the asperity density can be used as a fitting parameter to mimic experimental results.
- **Evolution of friction:** Both the static and the dynamic friction coefficient decreases with increasing nominal contact pressure. Experimental results are used to obtain the model parameter of the ploughing model. The negative correlation between the friction coefficient and the nominal contact pressure is predicted by the advanced friction model, although more than was found in the experiments. Calculated friction coefficients are within the expected range of experimentally obtained friction coefficients.

Two deep-drawing applications have been discussed in Chapter 5. Based on FE results using the mixed lubrication interface elements, the following is concluded:

- During forming, local friction coefficients depend on location and time, and rely on external process settings like the blankholder force, punch velocity and lubrication amount.
- An excellent prediction of the punch force is made for a simple-shaped metal product using the advanced friction model.

- Increasing the blankholder force, increasing the lubrication amount or increasing the lubricant viscosity decreases the average friction coefficient.
- For complex-shaped products the same frictional trends are found as for simple-shaped products. Increasing the blankholder force or increasing the amount of lubricant both decreases the average friction coefficient. However, the description of the material behavior itself becomes increasingly important, reducing the relative influence of friction.
- The increase in computation time, compared to a Coulomb friction model, was approximately 50 % for both applications.
- If starvation of lubricant occurs, meaning that only boundary lubrication is present, the boundary lubrication friction model as presented in Chapter 2 can be used directly. This excludes the use of mixed lubrication interface elements. In this case, the simulation time increases by less than 3 % compared to using a Coulomb friction model.

Numerical results obtained by the mixed lubrication friction model have been compared with results obtained by using the Coulomb friction model. A fitted constant friction coefficient has been used for the Coulomb model. This value only holds for a specific forming process, and depends on the process settings used, like the blankholder force or the amount of lubricant. In order to make an accurate prediction of punch forces, the Coulomb friction coefficient must be adapted for each specific process setting. Contrary to the Coulomb friction model, the advanced friction model does not require any adaptions to the original input data when process settings are changed. Input data is obtained by the calibration procedure presented in Chapter 4 and used as such in the FE forming simulations. This clearly demonstrates the increased predictive capabilities of the FE simulation when using the mixed lubrication friction model.

6.2 Recommendations

The multi-scale friction model is a modular framework in which existing, adapted and newly developed micro-mechanical friction models have been implemented. The choice of the implemented models was a trade-off between accuracy and computational efficiency. This section reviews the accuracy of the implemented models and presents recommendations for future research.

Validation of the multi-scale friction model

A comparison between numerically and experimentally obtained punch forces has been made for two deep-drawing applications in this thesis. Although FE results are in good agreement with the experimental results, a more thorough validation step is required to evaluate the increased predictive capabilities of FE software codes. For this purpose, the draw-in of the sheet material, the thickness distribution, the strain distribution and the amount of spring-back after forming could be compared with FE results. To validate the predicted lubricant pressure distribution during forming, pressure and shear sensors could be included into the tooling of the forming process. Also the fluid film thickness, left on the blank after forming [40], could be used for further validation of the friction model.

Biaxial straining

In Section 4.5, it was concluded that another, more advanced, model is required to describe the influence of bulk straining on the amount of asperity deformation. With respect to 3D FE forming simulations, a straining model should be developed that incorporates the effects of combined normal loading and biaxial straining. Besides asperity flattening, asperity roughening can occur due to grain rotations and the emergence of slip bands [65]. Although this mechanism has not been investigated in this research, it can have a significant influence on the development in real contact area [57]. A physical model to describe the combined influence of stretching, compression and roughening on the real contact area is desired. Although no theoretical solution is known, a parametric model could be built to obtain the development in real contact area for a changing set of parameters (geometry asperities, material properties, pressure exerted on the contact and strain in the material). Idealized geometries should be used for evaluation purposes. An upper-bound method or an FE method could be used to solve the parametric model, from which results can be used to derive simplified empirical relations. Additional research is required to develop such a model.

History dependency of deformed surface asperities

As discussed in Section 2.5, friction matrices are constructed for a range of nominal contact pressures and strains. These matrices are used in FE simulations to obtain friction coefficients for each integration point of the interface element in contact. The friction matrix, however, does not account for strain path dependency. To include strain path dependency, the boundary lubrication friction model must be rewritten in incremental form [6, 8]. One way to describe friction in FE simulations is to implement the incremental model directly into FE software, which excludes the use of matrices. This will lead to a more physically sound description of friction (compared to the current approach), although the simulation time will increase significantly. A more efficient approach is to generate additional matrices including history parameters, and use these matrices in an FE simulation.

Change in hardness during forming

The relation $H = B\sigma_y$ has been used to calculate the hardness of surface asperities (Section 2.3). The constant B is obtained from hardness tests and holds for approximately ideal-plastic material behavior under a typical 3D stress state in the material, i.e. the stress state present during hardness testing. The value of the factor B will change if a different stress state is present in the material. A proper model to describe the change in hardness during forming is not available yet, but is desirable to improve the accuracy of the advanced friction model. A parametric model could be built and solved for a set of parameters (indenter geometry, material properties, strain state). Results can be used to derive an empirical relation which can be used in the advanced friction model.

Boundary layer shear strength

A power-law relation is obtained from shear strength experiments to describe the boundary layer shear strength as a function of nominal contact pressure (Section 4.3). Shear strength experiments are, however, time consuming, and experimental settings like pressure, temperature and velocity are bounded by the apparatus used. In addition, the yield strength of the softer material determines the feasible pressure range of the experiments. This means that for soft metals (or metals with soft coatings) the shear strength could only be measured for low nominal contact pressures. The application of novel modeling techniques, e.g. molecular dynamics models [18], should be investigated to overcome the drawbacks of sliding experiments.

Roughness effects on fluid flow

The mixed lubrication interface elements account for flow factors to describe the influence of surface roughness on fluid flow. Flow factors have, however, not been accounted for in the application chapter of this thesis, since the accuracy of the predicted pressure distribution is not known when using flow factors from the literature. In fact, flow factors should be determined for each specific metal–lubricant combination. To obtain accurate flow factor expressions, either numerical flow simulations on 3D measured surface textures or lubricant flow experiments have to be conducted [58, 59].

Coated steels

A valuable extension of the model would be to enable the prediction of friction for coated workpiece materials. The flattening models have to be adapted to account for the combined hardness of the coating and the substrate. A proper degradation model should be implemented since boundary layers degrade more easily (known from practice, for example, for zinc-coated steels). If boundary layers degrade, dry contact occurs and galling or material pick-up could occur more easily during forming [61]. The friction framework should be extended to account for the influence of these mechanisms when coatings are considered.

Nominal contact pressure from FEM

A final recommendation is made regarding the calculation of the nominal contact pressure in FE simulations, describing an important input parameter for friction modeling. The nominal contact pressure is obtained by the *penalty method* in this research, which excels in computational efficiency compared to other methods and is commonly used for its numerical stability [26]. However, as for all FE contact algorithms, concessions with respect to the accuracy of the predicted nominal contact pressure have to be made for computational purposes. To further improve the accuracy of the frictional behavior during forming, not only are further developments in friction modeling required, but also in describing the nominal contact pressure during forming simulations.

Appendix A

Flow factor expressions

This appendix presents the flow factor expressions proposed by Patir & Cheng [50] and Wilson & Marsault [87] for 1D fluid flow. A longitudinal or transversal lay in the direction of sliding is assumed (excluding the coupling terms $\phi_{p,xy}$ and $\phi_{s,xy}$).

Patir & Cheng

For thin film geometries, i.e. $h/S_q > 3$, the following expressions to describe the flow factors $\phi_{p,x}$ and $\phi_{s,x}$ are used:

$$\begin{aligned} \phi_{p,x} &= 1 - Ce^{-rH_t} && \text{for} \quad \gamma \leq 1 \\ \phi_{p,x} &= 1 + CH_t^{-r} && \text{for} \quad \gamma > 1 \end{aligned} \tag{A.1}$$

and:

$$\begin{aligned} \phi_{s,x} &= A_1 H_t^{\alpha_1} \exp\left(-\alpha_2 H_t + \alpha_3 H_t^2\right) && \text{for} \quad H_t \leq 5 \\ \phi_{s,x} &= A_2 \exp\left(-0.25 H_t\right) && \text{for} \quad H_t > 5 \end{aligned} \tag{A.2}$$

with:

$$H_t = h/S_q \tag{A.3}$$

Expressions for the variables C, r, A_1, A_2, α_1, α_2 and α_3 as a function of the Peklenik surface pattern γ can be found in Table A.1 [50].

Table A.1 *Coefficients of Equations A.1 and A.2.*

γ	A_1	A_2	α_1	α_2	α_3	C	r
1/9	2.046	1.856	1.12	0.78	0.03	1.48	0.42
1/6	1.962	1.754	1.08	0.77	0.03	1.38	0.42
1/3	1.858	1.561	1.01	0.76	0.03	1.18	0.42
1	1.899	1.126	0.98	0.92	0.05	0.90	0.56
3	1.560	0.556	0.85	1.13	0.08	0.225	1.5
6	1.290	0.388	0.62	1.09	0.08	0.520	1.5
9	1.011	0.295	0.54	1.07	0.08	0.870	1.5

Wilson & Marsault

To describe fluid flow under mixed-lubrication conditions, i.e. $h/S_\mathrm{q} < 3$, the following expressions for the flow factors $\phi_{\mathrm{p},x}$ and $\phi_{\mathrm{s},x}$ are used:

$$\phi_{\mathrm{p},x} = \frac{1}{H_\mathrm{t}^3}\left(a_1\left(H_\mathrm{t} - H_\mathrm{tc}\right)^2 + a_2\left(H_\mathrm{t} - H_\mathrm{tc}\right)^3\right) \tag{A.4}$$

with:

$$H_\mathrm{tc} = 3\left(1 - \left(\frac{0.47476}{\gamma + 1}\right)^{-0.25007}\right) \tag{A.5}$$

and:

$$\begin{aligned} a_1 &= 0.051375\ln^3(9\gamma) - 0.0071901\ln^4(9\gamma) \\ a_2 &= 1.0019 - 0.17927\ln(\gamma) + 0.047583\ln^2(\gamma) - 0.016417\ln^3(\gamma) \end{aligned} \tag{A.6}$$

and:

$$\phi_{\mathrm{s},x} = b_0 + b_1 H_\mathrm{t} + b_2 H_\mathrm{t}^2 + b_3 H_\mathrm{t}^3 + b_4 H_\mathrm{t}^4 + b_5 H_\mathrm{t}^5 \tag{A.7}$$

with:

$$\begin{aligned} b_0 &= 0.12667\gamma^{-0.6508} \\ b_1 &= \exp\left(-0.38768 - 0.44160\ln(\gamma) - 0.12679\ln^2(\gamma) + 0.042414\ln^3(\gamma)\right) \\ b_2 &= -\exp\left(-1.1748 - 0.39916\ln(\gamma) - 0.11041\ln^2(\gamma) + 0.031775\ln^3(\gamma)\right) \end{aligned}$$

$$
\begin{aligned}
b_3 &= \exp\left(-2.8843 - 0.36712\ln(\gamma) - 0.10676\ln^2(\gamma) + 0.028039\ln^3(\gamma)\right) \\
b_4 &= -0.004706 + 0.0014493\ln(\gamma) + 0.00033124\ln^2(\gamma) - 0.00017147\ln^3(\gamma) \\
b_5 &= 0.00014734 - 4.255\times 1^{-5}\ln(\gamma) - 1.057\times 1^{-5}\ln^2(\gamma) + 5.0292\times 1^{-6}\ln^3(\gamma)
\end{aligned}
\tag{A.8}
$$

Bibliography

[1] A. Almqvist, D. Lukkassen, A. Meidell, and P. Wall. New concepts of homogenization applied in rough surface hydrodynamic lubrication. *International Journal of Engineering Science*, 45:139–154, 2007.

[2] Taylan Altan and Erman Takkaya, editors. *Sheet metal forming fundamentals*. ASM International, 2012.

[3] Y. Bergström. A dislocation model for the stress-strain behaviour of polycrystalline α-Fe with special emphasis on the variation of the densities of mobile and immobile dislocations. *Materials Science and Engineering*, 5:193–200, 1970.

[4] R. Boman and J. P. Ponthot. Finite element simulation of lubricated contact in rolling using the arbitrary Lagrangian-Eulerian formulation. *Computer Methods in Applied Mechanics and Engineering*, 193:4323–4353, 2004.

[5] J. F. Booker and K. H. Huebner. Application of finite element methods to lubrication: An engineering approach. *Journal of Lubrication Technology*, 94:313–323, 1972.

[6] R. Bosman. History dependent friction model for sheet metal forming. Master's thesis, University of Twente, 2013.

[7] B. J. Briscoe and D. C. B. Evans. The shear properties of Langmuir-Blodgett layers. *Proceedings of the Royal Society of London. Series A, Mathematical and Physical Sciences*, 380:389–407, 1982.

[8] M. F. C. Bruinja. Extending an advanced friction model for sheet metal forming. Master's thesis, University of Twente, 2012.

[9] J. M. Challen and P. L. B. Oxley. An explanation of the different regimes of friction and wear using asperity deformation models. *Wear*, 53:229–243, 1979.

[10] J. M. Challen and P. L. B. Oxley. Slip-line fields for explaining the mechanics of polishing and related processes. *International Journal of Mechanical Siences*, 26:403–418, 1984.

[11] J. S. Courtney-Pratt and E. Eisner. The effect of a tangential force on the contact of metallic bodies. *Proceedings of the Royal Society of London. Series A, Mathematical and Physical Sciences*, 238:529–550, 1957.

[12] C. de Boor. On calculating with B-splines. *Journal of Approximation Theory*, 6:50–62, 1972.

[13] M.B. de Rooij. *Tribological aspects of unlubricated deepdrawing processes*. PhD thesis, University of Twente, 1998.

[14] P. M. Dixit and S. Dixit. *Modeling of metal forming and machining processes, by finite element and soft computing methods*. Springer-Verlag London Limited, 2008.

[15] W. C. Emmens. *Tribology of flat contacts and its application in deep drawing*. PhD thesis, University of Twente, 1997.

[16] F. Filzek, M. Ludweg, and P. Groche. Improved FEM simulation of sheet metal forming with friction modelling using laboratory tests. *15th International Deep Drawing Research Group Conference, IDDRG2011*, 2011.

[17] J. Filzek and P. Groche. Assessment of the tribological function of lubricants for sheet metal forming. *ASTM Special Technical Publication*, 1404:97–108, 2001.

[18] J. Gao, W. D. Luedtke, and U. Landman. Nano-elastohydrodynamics: Structure, dynamics and flow in nonuniform lubricated junctions. *Science*, 270:605–608, 1995.

[19] D. Godfrey. *Boundary lubrication*. 1968.

[20] J. A. Greenwood. A note on Nayak's third paper. *Wear*, 262:225–227, 2007.

[21] J. A. Greenwood and J. B. P. Williamson. Contact of nominally flat surfaces. *Proceedings of the Royal Society of London. Series A, Mathematical and Physical sciences*, 295:300–319, 1966.

[22] Aberdeen Group. The impact of strategic simulation on product profitability. 2011.

[23] R. Grueebler and P. Hora. Temperature dependent friction modeling for sheet metal forming. *International Journal of Material Forming*, 2:251–254, 2009.

[24] B. J. Hamrock, S. R. Schmid, and B. O. Jacobson. *Fundamentals of Fluid Film Lubrication*. Marcel Dekker, 2004.

[25] W. B. Hardy and I. Doubleday. Boundary lubrication - The paraffin series. *Proceedings of the Royal Society of London. Series A, Mathematical and Physical Sciences*, 100:550–574, 1922.

[26] G. T. Havinga. Contact methods for finite element modeling. Master's thesis, University of Twente, 2011.

[27] R. Hill. *The mathematical theory of plasiticy*. Oxford University Press, 1950.

[28] K. Hokkirigawa and K. Kato. An experimental and theoretical investigation of ploughing, cutting and wedge formation during abrasive wear. *Tribology International*, 21:51–57, 1988.

[29] M. K. Hu. Visual pattern recognition by moment invariants. *IRE Transactions on Information Theory*, pages 179–187, 1962.

[30] Y. K. Hu and W. K. Liu. An ALE hydrodynamic lubrication finite element method with application to strip rolling. *International Journal for Numerical Methods in Engineering*, 36:885–880, 1993.

[31] J. Huétink, J. van der Lugt, and J. R. Miedema. A mixed Eulerian-Lagrangian contact element to describe boundary and interface behaviour in forming processes. *Proceedings of the International Conference on Numerical Methods in Engineering: Theory*

and Applications, NUMETA, 1:131–151, 1987.

[32] D. K. Karupannasamy. *Friction modeling on multiple scales for deep drawing processes*. PhD thesis, University of Twente, 2013.

[33] D. K. Karupannasamy, J. Hol, M. B. de Rooij, V. T. Meinders, and D. J. Schipper. Modelling mixed lubrication for deep drawing processes. *Wear*, 294-295:296–304, 2012.

[34] T. Kayaba and K. Kato. Experimental analysis of junction growth with a junction model. *Wear*, 51:105–116, 1978.

[35] D. A. Korzekwa, P. R. Dawson, and W. R. D. Wilson. Surface asperity deformation during sheet forming. *International Journal of Mechanical Sciences*, 34(7):521–539, 1992.

[36] J. S. Lim. *Two-dimensional signal and image processing*. Prentice Hall, 1990.

[37] S-. W. Lo, T. C. Yang, and Z. M. Shih. Effects of surface roughening on asperity flattening. *Tribology Letters*, 35:67–75, 2009.

[38] S. W. Lo. A study on flow phenomena in mixed lubrication regime by porous medium model. *Journal of Tribology*, 116:640–647, 1994.

[39] S. W. Lo and S. D. Tsai. Real-time observation of the evolution of contact area under boundary lubrication in sliding contact. *Journal of Tribology*, 124:229–238, 2002.

[40] M. Ludwig, S. Volk, and P. Groche. Surface evolution and lubricant distribution in deep drawing. *Key Engineering Materials*, 554-557:811–824, 2013.

[41] X. Ma, M. de Rooij, and D. J. Schipper. A load dependent friction model for fully plastic contact conditions. *Wear*, 269:790–796, 2012.

[42] G. Maeder. *Advanced Methods in Material Forming*, chapter Material Forming and Dimensioning Problems: Expectations from the Car Industry, pages 19–33. Springer Berlin Heidelberg, 2007.

[43] F. Martinet and P. Chabrand. Application of ALE finite elements method to a lubricated friction model in sheet metal forming. *International Journal of Solids and Structures*, 37:4005–4031, 2000.

[44] J. S. McFarlane and D. Tabor. Relation between friction and adhesion. *Proceedings of the Royal Society of London, Series A*, 251:244–253, 1950.

[45] T. Meinders, I. A. Burchitz, M. H. A. Bonte, and R. A. Lingbeek. Numerical product design: Springback prediction, compensation and optimization. *International Journal of Machine Tools & Manufacture*, 48:499–514, 2008.

[46] P. R. Nayak. Random process model of rough surfaces in plastic contact. *Wear*, 26:305–333, 1973.

[47] A. Ovcharenko, G. Halperin, and I. Etsion. In situ and real-time optical investigation of junction growth in spherical elastic-plastic contact. *Wear*, 264:1043–1050, 2008.

[48] R. Parker and D. Hatch. The static coefficient of friction and the area of contact. *Proceedings of the Physical Society, Section B*, 63:185–197, 1950.

[49] N. Patir and H. S. Cheng. An average flow model for determining effects of three-dimensional roughness on partial hydrodynamic lubrication. *Journal of Lubrication*

Technology, 100:12–17, 1978.

[50] N. Patir and H. S. Cheng. Application of average flow model to lubrication between rough sliding surfaces. *Journal of Lubrication Technology*, 101:220–229, 1979.

[51] J. Peklenik. New developments in surface characterization and measurements by means of random process analysis. *Proceedings of the Institution of Mechanical Engineers*, 182:108–126, 1967.

[52] C. Y. Poon and B. Bhushan. Comparison of surface roughness measurements by stylus profiler, AFM and non-contact optical profiler. *Wear*, 190:76–88, 1995.

[53] J. Pullen and J. B. P. Williamson. On the plastic contact of rough surfaces. *Proceedings of the Royal Society of London. Series A, Mathematical and Physical Sciences*, 327:159–173, 1972.

[54] Lord Rayleigh. On the lubricating and other properties of thin oily films. *Philosophical Magazine*, 35:157–162, 1918.

[55] O. Reynolds. On the theory of lubrication and its application to Mr. Beauchamp Tower's experiments, including an experimental determination of the viscosity of olive oil. *Philosophical Transactions of the Royal Society*, 177:157–234, 1886.

[56] K. Roll, K. Wiegand, and P.Hora. Benchmark 2 - influence on drawbeads on the springback behaviour - part a: Physical tryout report. *Proceedings of Numisheet 2008 - 7th International Conference on Numerical Simulation of 3D Sheet Metal Forming Processes - Part B*, pages 45–52, 2008.

[57] P. K. Saha and W. R. D. Wilson. Influence of plastic strain on friction in sheet metal forming. *Wear*, 172:167–173, 1994.

[58] F. Sahlin, R. Larsson, A. Almqvist, P. M. Lugt, and P. Marklund. A mixed lubrication model incorporating measured surface topography. part 1: Theory of flow factors. *Proceedings of the Institution of Mechanical Engineers, Part J: Journal of Engineering Tribology*, 224:335–351, 2010.

[59] F. Sahlin, R. Larsson, P. Marklund, A. Almqvist, and P. M. Lugt. A mixed lubrication model incorporating measured surface topography. part 2: roughness treatment, model validation, and simulation. *Proceedings of the Institution of Mechanical Engineers, Part J: Journal of Engineering Tribology*, 224(J4):353–365, 2010.

[60] E. Schedin. *Micro-mechanisms of sheet-tool contact in sheet metal forming*. PhD thesis, Royal Institute of Technology, Sweden, 1991.

[61] J. A. Schey. *Tribology in Metalworking - Friction, Lubrication and Wear*. ASM, 1983.

[62] D. J. Schipper. *Transitions in the lubrication of concentrated contacts*. PhD thesis, University of Twente, 1988.

[63] D. J. Schipper and A. W. J. de Gee. Lubrication models and the IRG transition diagram. *Lubrication Science*, 8(1):27–35, 1995.

[64] S. Sheu and W. R. D. Wilson. Mixed lubrication of strip rolling. *Tribology Transactions*, 37(3):483–493, 1994.

[65] H. C. Shih and W. R. D. Wilson. Effects of contact pressure and strain on friction in sheet-metal forming. *Tribology Transactions*, 42:144–151, 1999.

[66] R. J. J. M. Sniekers. *Friction in deep drawing*. PhD thesis, Technical University Eindhoven, 1996.

[67] F. O. Sonmez and A. Demir. Analytical relations between hardness and strain for cold formed parts. *Journal of Materials Processing Technology*, 186:163–173, 2007.

[68] R. Stribeck. Die wesentlichen Eigenschaften der Gleit- und Rollenlager. *VDI-Zeitschrift*, 46:1341–1348, 1432–1438 and 1463–1470, 1902.

[69] M. P. F. Sutcliffe. Surface asperity deformation in metal forming processes. *International Journal of Mechanical Sciences*, 30:847–868, 1988.

[70] D. Tabor. Junction growth in metallic friction: The role of combined stresses and surface contamination. *Proceedings of the Royal Society of London*, 251:378–393, 1959.

[71] R. ter Haar. *Friction in Sheet Metal Forming; the influence of (local) contact conditions and deformation*. PhD thesis, University of Twente, 1996.

[72] R. ter Haar and E. H. Atzema. The impact of lubricant buffering on the operating window of deep drawing processes. *Proceedings of the 21st Biennial Congress of the International DeepDrawing Research Group*, 2000.

[73] X. Tian and B. Bhushan. A numerical three-dimensional model for the contact of rough surfaces by variational principle. *Journal of Tribology*, 118:33–42, 1996.

[74] R. S. Timsit and C. V. Pelow. Shear strength and tribological properties of stearic acid films (part 1) on glass and aluminium-coated glass. *Journal of Tribology*, 114:150–158, 1992.

[75] E.M. Toose. Private communication. 2010.

[76] A. H. van den Boogaard and J. Huétink. Simulation of aluminium sheet forming at elevated temperatures. *Computer Methods in Applied Mechanics and Engineering*, 195:6691–6709, 2006.

[77] J. van der Lugt. *A finite element method for the simulation of thermo-mechanical contact problems in forming processes*. PhD thesis, University of Twente, 1988.

[78] P. van Liempt. Workhardening and substructural geometry of metals. *Journal of Materials Processing Technology*, 45:459–464, 1994.

[79] H. Vegter. *On the plastic behaviour of steel during sheet forming*. PhD thesis, University of Twente, 1991.

[80] H. Vegter and A. H. van den Boogaard. A plane stress yield function for anisotropic sheet material by interpolation of biaxial stress states. *International Journal of Plasticity*, 22:557–580, 2006.

[81] J. D. Westeneng. *Modelling of contact and friction in deep drawing processes*. PhD thesis, University of Twente, 2001.

[82] J. H. Wiebenga, A. H. van den Boogaard, and G. Klaseboer. Sequential robust optimization of a V-bending process using numerical simulations. *Journal of Structural and Multidisciplinary Optimization*, 46:137–153, 2012.

[83] W. R. D. Wilson. Friction and lubrication in bulk metal-forming processes. *Journal of Applied Metal Working*, 1:1–7, 1979.

[84] W. R. D. Wilson. Friction models for metal forming in the boundary lubrication regime. *American Society of Mechanical Engineers*, 10:13–23, 1988.

[85] W. R. D. Wilson. Mixed lubrication in metal forming. *Advanced Technology Plasticity*, 4:1667–1675, 1990.

[86] W. R. D. Wilson and D. F. Chang. Low speed mixed lubrication of bulk metal forming processes. *Journal of Tribology*, 118:83–89, 1996.

[87] W. R. D. Wilson and N. Marsault. Partial hydrodynamic lubrication with large fractional contact areas. *Journal of Tribology*, 120:16–20, 1998.

[88] W. R. D. Wilson and S. Sheu. Real area of contact and boundary friction in metal forming. *International Journal of Mechanical Science*, 30:475–489, 1988.

[89] W. R. D. Wilson and J. J. Wang. Hydrodynamic lubrication in simple stretch forming processes. *Journal of Tribology, Transactions of the ASME*, 106:70–77, 1984.

[90] D. M. Maietta Y. Zhao and L. Chang. An asperity microcontact model incorporating the transition from elastic deformation to fully plastic flow. *Journal of Tribology*, 122:86–93, 2000.

[91] T. S. Yang and S. W. Lo. A finite element analysis of full film lubricated metal forming processes. *Tribology International*, 37:591–598, 2004.

[92] Y. Zhao and L. Chang. A model of asperity interactions in elastic-plastic contact of rough surfaces. *Journal of Tribology*, 123:857–864, 2001.

Key results

Key results related to this research project, i.e. publications and research activities, are presented here.

Journal publications

1. J. Hol, V.T. Meinders, M.B. de Rooij and A.H. van den Boogaard. Multi-scale friction modeling for sheet metal forming: Boundary lubrication friction. *In preparation*. (Chapter 2 of this thesis)

2. J. Hol, V.T. Meinders, H.J.M. Geijselaers and A.H. van den Boogaard. Multi-scale friction modeling for sheet metal forming: Mixed lubrication friction. *In preparation*. (Chapter 3 of this thesis)

3. D.K. Karupannasamy, J. Hol, M.B. de Rooij and D.J. Schipper. A friction model for deep drawing processes under loading/reloading conditions. *In preparation*.

4. J. Hol, D.K. Karupannasamy, R. Boterman, M.B. de Rooij and V.T. Meinders. Calibration and validation of an advanced friction model for mild steel under forming conditions. *Submitted*, 2013. (Chapter 4 of this thesis)

5. D.K. Karupannasamy, J. Hol, M.B. de Rooij, T. Meinders and D.J. Schipper. Modeling mixed lubrication for deep drawing processes, *Wear*, 294-295:296-304, 2012.

6. J. Hol, M.V. Cid Alfaro, M.B. de Rooij and V.T. Meinders. Advanced friction modeling for sheet metal forming. *Wear*, 286-287:66-78, 2012.

7. J. Hol, M.V. Cid Alfaro, V.T. Meinders and J. Huétink. Advanced friction modeling in sheet metal forming. *Key engineering materials*. 473:715-722, 2011.

8. R. Bosman, J. Hol and D.J. Schipper. Running-in of metallic surfaces in the boundary lubrication regime. *Wear*, 271:1135-1146, 2011.

Conference Proceedings

1. V.T. Meinders, J. Hol and A.H. van den Boogaard. Boundary and mixed lubrication friction modeling under forming process conditions. *Accepted by the 9th International Conference and Workshop on Numerical Simulation of 3D Sheet Metal Forming Processes (Numisheet 2014)*, 2014, Melbourne, Australia.

2. J. Hol, V.T. Meinders and A.H. van den Boogaard. Experimental and numerical friction characterization of DC06 high formable steel. *International Deep Drawing Research Group (IDDRG 2013)*, 2013, Zurich, Switzerland.

3. J. Hol, D.K. Karupannasamy and V.T. Meinders. Friction modeling for manufacturing processes: Application to sheet metal forming. *ASME 2012 International Manufacturing Science and Engineering Conference (MSEC 2012)*, 2012, Indiana, USA.

4. J. Hol, M.V. Cid Alfaro, V.T. Meinders and J. Huétink. A multi-scale friction model for sheet metal forming simulations. *8th International Conference and Workshop on Numerical Simulation of 3D Sheet Metal Forming Processes (Numisheet 2011)*, 2011, Seoul, Korea. In: K. Chang, H. Nam Han, H. Huh, F. Barlat and M. Lee (Eds.). *AIP Conference Proceedings*, 1383:784-791, 2011.

5. J. Hol, V.T. Meinders and J. Huétink. A multi-scale friction model framework for full scale sheet forming simulations. *14th ESAFORM conference*, 2011, Belfast, UK. In: G. Menary (Ed.), *AIP Conference Proceedings*, 1353:207-212, 2011.

6. J. Hol, M.V. Cid Alfaro, M.B. de Rooij and V.T. Meinders. Multi-scale friction modeling for sheet metal forming. *4th International Conference on Tribology in Manufacturing Processes (ICTMP 2010)*, 2010, Nice, France. In: E. Felder and P. Montmitonnet (Eds.). *Tribology of Manufacturing Processes*, 573-582, 2010.

Invited speaker

Keynote presentation at the 8th forum for Tribologische Entwicklungen in der Umformtechnik (Triboforum) in Darmstadt, 2013, entitled: 'Calculating coefficients of friction as input for finite element simulations' by C. Dane (Tata Steel) and J. Hol.

Software package TRIMM

Within this research project, the stand-alone software package TRIMM has been developed. TRIMM can be used to characterize friction between user-defined metal–lubricant combinations under metal forming conditions. The boundary lubrication friction model and mixed lubrication friction model presented in this thesis form the foundation of the TRIMM software.

Spin-off company: 'Innprove Solutions'

During this research project the spin-off company Innprove Solutions was founded by J.H. Wiebenga and J. Hol. Innprove Solutions is an engineering company providing consultancy services and software solutions in the field of virtual design and tribological modeling. Cooperating partners are the University of Twente, Tata Steel and the Materials innovation institute (M2i).

Dankwoord

Zondag 3 november

Eindelijk, het proefschrift is af! Nou ja, bijna af. Er komt nog één hoofdstukje achteraan, het dankwoord. Het volledige traject heeft ongeveer vier en een half jaar geduurd, waarvan de afgelopen vier maanden ongetwijfeld het zwaarst zijn geweest. Dit komt niet zo zeer door het strakke schema om het proefschrift op tijd af te krijgen, maar meer door de warme zomerdagen die ik heb doorgebracht in een veel te warme studeerkamer. Maar goed, het resultaat mag er dan ook zijn, en inmiddels durf ik voorzichtig weer achterover te leunen met een spannende thriller in mijn handen. Helaas wel binnen, want grijze donkere wolken hebben het zomerse zonnetje inmiddels verdreven en heeft Nederland alweer met de eerste zware herfststormen te maken gehad.

Het onderzoek zoals beschreven in dit proefschrift is uitgevoerd aan de Universiteit Twente binnen de vakgroep Nonlinear Solid Mechanics, in samenwerking met de vakgroep Surface Technology and Tribology en de industriële partner Tata Steel. Het project is onderdeel geweest van het programma van het onderzoeksinstituut M2i onder het projectnummer MC1.07289. In dit dankwoord wil ik graag iedereen bedanken die op enige wijze een bijdrage heeft geleverd aan dit onderzoek.

Allereerst wil ik mijn promotor Ton van den Boogaard bedanken voor zijn begeleiding in dit onderzoek. Ton, jouw scherpe blik is van onschatbare waarde geweest om dit onderzoek te brengen waar het nu staat. Lichtelijk frustrerend was het als je binnen één minuut een antwoord had op een probleem waar ik de nodige uurtjes al aan had besteed. Bedankt voor de vrijheid die ik gekregen heb om zelf invulling te geven aan dit onderzoek, en, ondanks je overvolle agenda, voor de tijd die je voor mij vrijgemaakt hebt. Han Huétink, tot eind 2010 heb jij dit onderzoek onder je hoede gehad. Bedankt voor de sturing aan het begin van het onderzoek en de leuke (en natuurlijk leerzame) discussies die daarbij hoorden.

Timo Meinders was het eerste aanspreekpunt in mijn onderzoek en tevens copromotor van dit proefschrift. Timo, wanneer ik terugdenk aan de afgelopen vier en

een half jaar, dan denk ik aan de wekelijkse maandagochtendbesprekingen, de ‘één-minuutgesprekjes’, de Numisheet 2011 conferentie in Seoul, mountainbiken (al was het eenmalig), post-its, roze ballonnen en een gezonde dosis humor. Maar daarnaast natuurlijk ook aan de vele technisch-inhoudelijke discussies en brainstormsessies die dit proefschrift zijn uiteindelijke vorm heeft gegeven. Bedankt dat je deur altijd open stond, je uitgesproken mening die meer dan eens goed van pas kwam en je steun en vertrouwen in dit onderzoek!

Alle (ex-)collega’s van de vakgroepen Technische Mechanica en Productietechnologie, bedankt voor de leerzame maar vooral gezellige periode aan de Universiteit Twente. Jan Harmen Wiebenga, met jou heb ik ongetwijfeld de meeste tijd doorgebracht. Naast de conferenties, de cursussen en de vele liters koffie, hebben we ondertussen aardig wat uurtjes in ons bedrijf Innprove Solutions zitten. Bedankt voor de lol, de interesse en de vele keren dat je met je heldere blik naar dit manuscript gekeken hebt. Zelfs toen je volop in de stress zat om je eigen boekje af te ronden maakte je tijd vrij om delen van dit proefschrift door te lezen, top! Daan Waanders, jij kwam kantoor N130 halverwege dit jaar met je humor versterken. Bedankt voor de tijd die je vrijmaakte als ik van je creatieve geest gebruik wilde maken en voor de schuimkabouters die je wekelijks van het tankstation meebracht. Bert Geijselaers, bedankt voor je fundamentele inbreng in dit project en je hulp wanneer ik weer eens een wiskundige vastloper had. Jos Havinga, Mart Bruinja en Ruben Bosman, bedankt voor jullie bijdrage aan dit onderzoek door middel van jullie afstudeerwerk. Harm Wisselink en Nico van Vliet, bedankt voor jullie ondersteuning rondom de eindige-elementencode DIEKA. Ook Axel Lok wil ik bedanken voor het regelen van zo’n beetje alle ICT zaken en Laura Vargas voor haar assistentie in het gebruik van de confocaal microscoop. De secretaresses van de vakgroep, Debby, Belinda en aan het begin van mijn onderzoek ook Tanja, bedankt voor het regelen en organiseren van zo’n beetje alles, jullie zijn toppers!

De leescomissie van dit proefschrift, Ton van de Boogaard, Timo Meinders en Jan Harmen Wiebenga, bedankt voor jullie kritische blik op dit werk. Mijn vriendin kon op mijn gezicht aflezen wanneer ik weer een hoofdstuk met jullie had doorgesproken. Maar eerlijk is eerlijk, het proefschrift is er een stuk strakker en leesbaarder door geworden! Bo Cornelissen, bedankt dat ik jouw stylesheet mocht gebruiken voor dit proefschrift, ongemerkt scheelt dit zomaar een paar dagen beeldschermgetuur. Jan Harmen Wiebenga en Alex Hol, bedankt dat jullie mijn paranimfen zijn tijdens de verdediging van dit proefschrift. Mede dankzij jullie zie ik deze dag met vertrouwen tegemoet.

Vanaf het begin van dit onderzoek was Matthijn de Rooij het eerste aanspreekpunt op tribologisch vlak. Matthijn, in vier en een half jaar tijd heb

jij mij op een vakkundige manier kennis laten maken met de wondere wereld van de tribologie. Jouw enthousiasme in dit vakgebied werkt werkelijk waar aanstekelijk. Bedankt voor je deskundige bijdrage aan mijn onderzoek en de vele leuke en leerzame discussies die we hebben gevoerd. Dinesh Karupannasamy, thanks for sharing your expertise in the field of tribology and for the nice discussions we had on friction modeling. I wish you all the best in your future career.

Van Tata Steel waren Matthijs Toose, Romke Boterman, Chiel Dane, Henk Vegter, Toni Chezan en aan het begin ook Marcela Cid Alfaro direct betrokken bij dit project. Bedankt voor jullie deskundige inbreng in dit onderzoek. Een speciaal woord van dank gaat uit naar Romke, die halverwege dit onderzoek aan boord is gekomen. Mede dankzij jou is dit onderzoek in een stroomversnelling terecht gekomen. Speciale dank ook aan Matthijs, voor het coördineren van dit onderzoek binnen Tata Steel en voor het delen van zijn brede kennis op tribologisch vlak. Chiel, Henk en Toni, bedankt voor jullie actieve deelname in dit project en jullie industriële visie op dit onderzoek. Zeker naar het einde van dit project toe is deze van onschatbare waarde geweest. Marco Appelman en Albert Lourens, bedankt voor jullie hulp tijdens het uitvoeren van RFT en U-bend experimenten. Ten slotte wil ik de deelnemers van de Tata-UT groep bedanken voor de interessante gesprekken tijdens de driemaandelijkse bijeenkomsten. Het zijn de kleine opmerkingen tussendoor die een project een bepaalde richting op kunnen sturen.

Mede dankzij onderzoeksinstituut M2i was het mogelijk om vier en een half jaar aan dit onderzoek te werken. Bert van Haastrecht wil ik bedanken voor het coördineren van dit onderzoek vanuit M2i. Dames van M2i, bedankt voor het regelen van alle nodige zaken rondom mijn onderzoek en de gezelligheid tijdens de jaarlijkse M2i conferenties en sportdagen. Alice Sosef-van Leijen, ik zal je maandelijkse belletje missen wanneer ik weer eens mijn time-sheets niet had ingevuld. Bedankt dat je de moed niet opgaf en elke maand weer netjes mijn salaris uitkeerde. Monica Reulink, ik ken weinig mensen die zo positief in het leven staan als jij. Bedankt voor je interesse in zo'n beetje alles! Ook wil ik de partners van M2i bedanken, voor de getoonde interesse in dit onderzoek tijdens cluster 1 vergaderingen en conferenties.

De mogelijkheid die mij en Jan Harmen Wiebenga geboden is om tijdens mijn onderzoek het spin-off bedrijf Innprove Solutions op te starten wil ik niet ongenoemd laten. Ik wil M2i, Tata Steel en de Universiteit Twente, die dit met hun actieve en flexibele opstelling mogelijk hebben gemaakt, dan ook van harte bedanken. Voor een jonge start-up is deze ondersteuning zeer waardevol.

Als laatste wil ik mij richten tot mijn familie, schoonfamilie en vrienden. Bedankt voor de inspiratie, de steun, de schouderklopjes, de lol en natuurlijk de welgemeende interesse de afgelopen jaren. Meer dan eens hebben jullie, bewust of onbewust, een positieve bijdrage geleverd aan dit onderzoek! Pa en ma, bedankt voor jullie steun en vertrouwen in alles wat ik doe. Jullie zijn fantastische ouders en vervullen een belangrijke rol in mijn leven. Broer, eindelijk kunnen we Dr. Hol tegen elkaar zeggen! Bedankt voor de ontspannende momenten in Beuningen, dat intussen een tweede thuisbasis voor mij en Lilian is geworden. Lieve Lilian, de laatste zinnen van mijn proefschrift zijn voor jou. Vier en een half jaar geleden ben je naar Enschede gekomen om samen met mij de uitdaging van het promoveren aan te gaan. Bedankt voor je liefde, je zorg en je begrip voor de vele avonden en weekenden die in dit werk zijn gaan zitten. Vooral de laatste vier maanden zullen ook voor jou niet de leukste maanden zijn geweest. Maar het is ons gelukt, het proefschrift is af! Bedankt voor alles, ik hou van je.

Johan